Dissertation
submitted to the
Combined Faculties for the Natural Sciences and for Mathematics
of the Ruperto-Carola University of Heidelberg, Germany
for the degree of
Doctor of Natural Sciences

Put forward by
Diplom-Physiker: **Philip Guthardt Torres**
Born in: **Bremen**
Oral examination: **09.05.2012**

Modeling Shape and Rupture of Filament Networks

Referees: **Prof. Dr. Ulrich S. Schwarz**
Prof. Dr. Dieter W. Heermann

Zusammenfassung

Das Aktin-Zytoskelett ist ein Netzwerk aus Biopolymeren, welches für die räumliche Koordination und mechanische Festigkeit biologischer Zellen sorgt. Aufgrund der asymmetrischen mechanischen Antwort von Polymeren auf Spannung und Kompression, verhält es sich wie ein mechanisches Kabelnetzwerk. Darüber hinaus ist es in einem Zustand dauerhafter Kontraktion aufgrund der Aktivität von Myosinmotoren. Wir untersuchen hier theoretische Modelle auf zellulärer Skala, die beide Besonderheiten berücksichtigen. Im ersten Teil dieser Arbeit untersuchen wir Modelle von Zellen, die an diskreten Haftstellen auf ebenen Flächen adhärieren. Wir vergleichen die Form und die Kraftverteilung in kontrahierten Feder- und Kabelnetzwerken. Es zeigt sich, dass nur aktive Kabelnetze die experimentell beobachtete Zellform korrekt vorhersagen. Im zweiten Teil verwenden wir das aktive Kabelnetzwerk zur Interpretation experimenteller Daten. Wir verbinden dieses dazu mit kontraktilen Aktin-Bündeln und sehen, dass diese Kombination zu überraschend guten Vorhersagen für die Spannungsverteilung von adhärierten Zellen auf weichen elastischen Substraten führt. Da zelluläre Kräfte zur Zerstörung des Netzwerkes führen können, untersuchen wir im dritten Teil das Brechen von Verbindungen in mechanische Netzwerken. Dabei brechen Verbindungen stochastisch mit Raten, die exponentiell mit der anliegenden Kraft wachsen. Wir untersuchen die statistischen Eigenschaften von Netzwerken unter konstanter Verformung und zeitlich linear wachsender Verformung. Die Ergebnisse vergleichen wir mit denen aus traditioneller Bruchmechanik, welche durch Stabilitätsgrenzen dominiert sind.

Abstract

The actin cytoskeleton is a biopolymer network that provides spatial coordination and mechanical strength to biological cells. Due to the asymmetric mechanical response of polymers under tension versus compression, it behaves like a mechanical network of cables. In addition, it actively contracts through the continuous action of myosin molecular motors. Here we investigate theoretical models on the cellular scale which incorporate these special properties. In the first part of this work we model cells adherent to discrete adhesion sites on planar surfaces. We compare the shape and force distribution in contracted networks of Hookean springs and cables. We find that only active cable networks can correctly predict the experimentally observed cell shape. In the second part we apply the active cable network to experimental data. We combine this model with contractile actin bundles and find that this combination leads to surprisingly good predictions for the traction force pattern of adherent cells on soft elastic substrates. Because cellular forces can lead to failure of the network, in the third part we investigate bond rupture in mechanical networks. Here, bonds stochastically rupture with rates that grow exponentially with force. We study the statistical properties of networks under constant strain and strain which linearly increases in time. The results are compared to traditional fracture mechanics which are dominated by stability thresholds.

Contents

List of Figures

Glossary

3T3	Mouse fibroblasts from the NIH 3T3 cell line
ACN	Active cable network
ADF	Actin depolymerizing factor
AFM	Atomic force microscopy / Atomic force microscope
ATP	Adenosine triphosphate
B16	Mouse melanoma cell line
BC	Boundary condition
BFP	Biomembrane force probe
CD	Constant displacement
CDF	Cumulative distribution function
CGM	Conjugate gradient method
CoT	Connective tissue
CSK	Cytoskeleton
CT	Center tree
DSF	Dorsal stress fiber
ECM	Extracellular matrix
ET	Epithelial tissue
FA	Focal adhesion
FBC	Free boundary conditions
FBM	Fiber bundle model
FEM	Finite element method
H1	Hexagonal network topology
H2	Hexagonal network topology inclined by $\pi/2$
HSN	Hookean spring network
LD	Linear displacement
LOT	Laser optical tweezers
MD	Molecular dynamics
MDCK	Madin-Darby canine kidney
MP	Motor protein
PBC	Periodic boundary conditions
PCN	Passive cable network
PDF	Probability density function
RBC	Red blood cell
RFM	Random fuse model
RSM	Random spring model
S1	Square network topology
S2	Diamond network topology
SDM	Steepest descend method
SF	Stress fiber
T1	Triangular network topology
T2	Triangular network topology inclined by $\pi/2$
TEM	Tension-elasticity model
TFM	Traction force microscopy / Traction force microscope
TVA	Transverse arc
U2OS	Human osteosarcoma cell line
VSF	Ventral stress fiber
WLC	Worm-like-chain

1

Introduction

1.1 Biological and Biophysical Background

1.1.1 Actin and Actin-related Proteins

The *actin cytoskeleton* (CSK) is a crucial part of eukaryotic cells. It consists of the structural protein actin, 50% of which in the cytoplasm is available in the form of monomers, small globules with a diameter of $\sim 8\ nm$, also called G-actin [1]. G-actin polymerizes to form long protein chains, called actin filaments or F-actin, which can be up to 100 μm long. The other half of a cell's actin is available in this filamentous form, whose representatives have a persistence length on the order of their physiological length in the μm range [2, 3]. In living cells there is continuous turnover from G-actin to F-actin and vice versa [1, 4].

G-actin exhibits two structurally different ends, i.e. the actin monomer is polar, see Fig. 1.1(a). Three actin monomers can build a nucleus, to which more and more actin globules are added. This happens in such a way that always two different ends of G-actin bind. Hence, the actin filament is polar itself. It consists of two parallel polymer chains, which are twisted into a double helix, Fig. 1.1(b). Please note, these two strands do not form individually. One end of the actin filament, the plus end, significantly grows faster than the other one, the minus end. G-actin has adenosine triphosphate (ATP) bound in its center, see Fig. 1.1(a). ATP can be seen as the fuel of cellular processes. During actin polymerization ATP is hydrolyzed to adenosine diphosphate (ADP), so ADP is bound inside the monomers of F-actin [1].

There are many cellular processes for which the actin CSK acts as the key player. Among the most important examples are cell migration [5], cell division [4], and cell adhesion [6]. But since all these cannot be regulated by variants of the protein actin only, there are many actin related proteins which take part in regulation [1]. Myosin II, for example, is a motor protein, which can bind to two actin filaments and slide them relatively to each other, thereby applying stress to the actin CSK [7]. Further examples are given by ADF/cofilin which severs actin filaments [8], and capping proteins, which inhibit polymerization of the filament end they bind to. Formins are also very

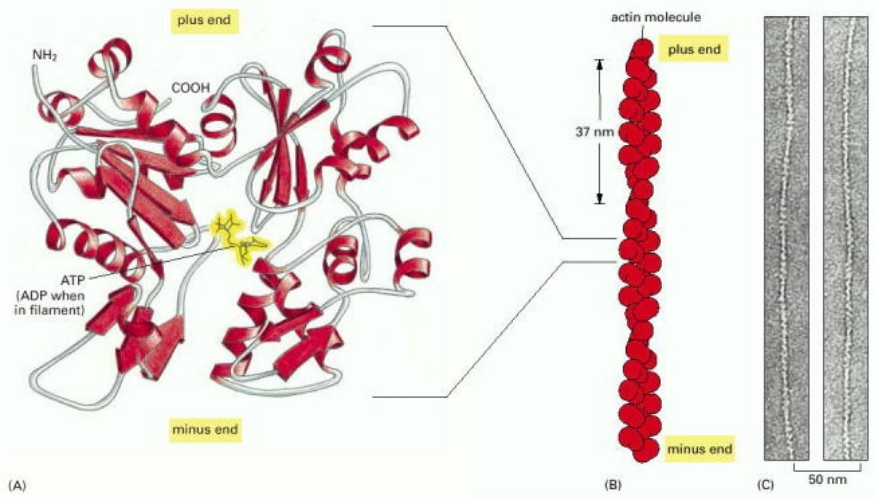

Figure 1.1: Actin Filaments. (a) A schematic view of a single actin molecule. ADP is bound in the center of the actin molecule. (b) Actin molecules have polymerized to an actin filament. After 37 nm the helix repeats. (c) Transmission electron microscopy image of an actin filament. Taken from [1].

important. Proteins from this family, like the protein complex ARP2/3, nucleate filaments [9]. ARP2/3 binds to an actin filament and nucleates a new one. Thus, ARP2/3 is crucial for the regulation of dendritic networks of actin filaments [10].

Motor proteins (MPs) also hydrolyze ATP to gain chemical energy, which they transform into mechanical work [1]. A myosin II molecule consists of a head and a tail domain, see Fig. 1.2. The head domain has two heads, each of which is composed of a heavy chain connected to the tail by two light chains. The tail of myosin II is a double helix of two twisted parallel strands. Although there has already been discovered a variety of myosin families, we restrict the discussion to myosin II motors. A special form of myosin II e.g. acts in muscles to mediate contraction of anti-parallel actin filaments in sarcomeres. Like most myosins, myosin II is non-processive, i.e. after binding to a filament, it falls off very soon. However, the two heads can be bound to an actin filament. It is assumed that ATP hydrolysis leads to the release of one head. Equivalent to making a step with our feet the head is moved to another place

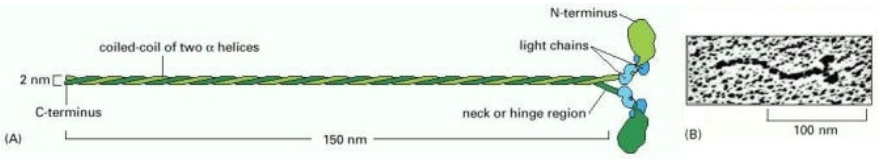

Figure 1.2: Myosin II motor protein. (a) Cartoon of a myosin II molecule. (b) Transmission electron microscopy image of a single myosin II molecule. Taken from [1].

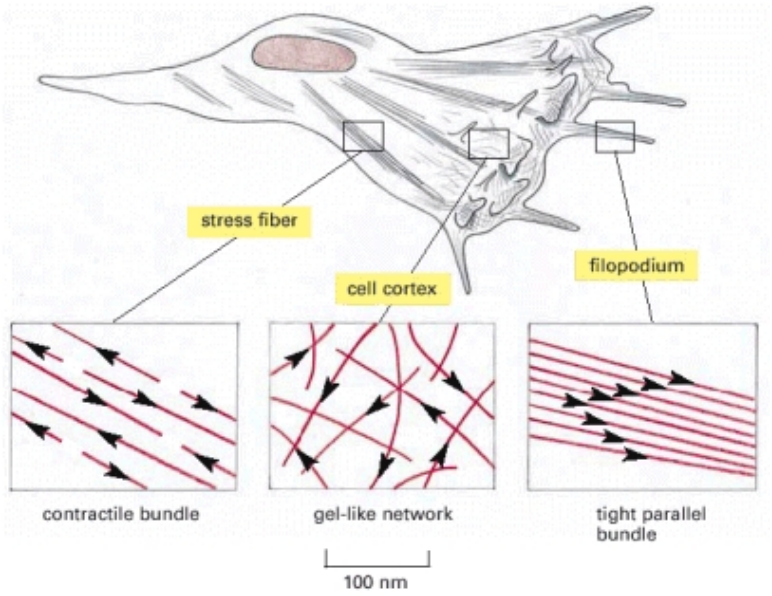

Figure 1.3: Different actin arrays of a tissue cell. Schematic of the different actin arrays. Left box: Loosely packed but highly contractile anti-parallel actin bundles in stress fibers which are connected by α-actinin and myosin II. Middle box: Gel-like actin network in the cell cortex linked together by filamin. Right box: Densely packed parallel actin bundles connected by fimbrin. Taken from [1].

to bind again to the filament. So the MP can walk along the filament and displace cargo, e.g. vesicles or other actin filaments, which are attached to the MP's tail, along the filament. To displace cargo over a long distance, several myosin II motors can bind together to motor complexes and work cooperatively. That way, myosin II can bundle actin filaments and set these bundles under permanent tension [1]. These bundles may be anchored e.g. to a substrate, so the motor feels a force against its walking direction. This decreases the motor's walking speed eventually down to zero. If stalled, the motor pulls with a constant value, the motor stall force [11].

In eukaryotic cells there are distinct structures actin filaments are organized into, see Fig. 1.3 [1]. Contractile bundles consist of anti-parallel actin filaments connected by α-actinin, which compared to G-actin and the head domain of myosin II is a quite large ($\approx$ 25 nm) protein, so the contractile bundle is very loosely packed. Hence myosin II motors can bind to two filaments and walk towards their plus ends. In the extreme case, filament bundles condense to highly contractile structures called stress fibers (SFs), which can have one end or both ends anchored to focal adhesion (FAs). FAs are connections between the actin CSK and extracellular space. SFs and FAs will be discussed below in more detail. Another actin linker protein, fimbrin, aligns actin filaments in a parallel fashion. Since fimbrin is much smaller than α-actinin, myosin II molecules cannot enter the parallel bundle which therefore is not under tension. An-

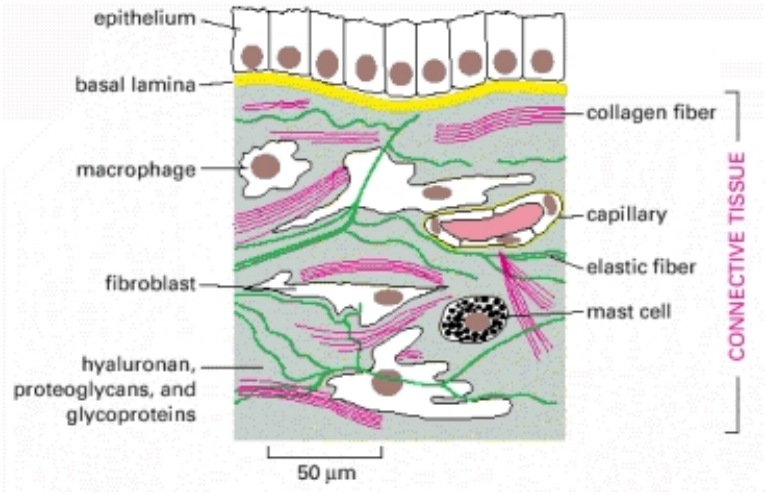

Figure 1.4: Epithelial tissue and connective tissue. Epithelial tissue built by cells connected via adhesion belts. The ECM of epithelia basically only consists of the basal lamina. The ECM of connective tissue contains variate macromolecules and only rarely distributed fibroblasts. Taken from [1].

other prominent structure formed by actin filaments, the two-dimensional network of the cell cortex, is interconnected via the protein filamin, such that the actin network can be contractile as well [1]. The filopdium shown in Fig. 1.3 is not the only protrusion of eukaryotic cells. Migrating cells exhibit a thin layer of polymerizing actin filaments at the cell wall. Two different components of this layer are distinguished. The lamellipodium is a dendritic network branched by ARP2/3 and destabilized by ADF/cofilin, while the lamella is much more stable and contractile [1].

Besides actin filaments there are other two very important kinds of filaments in the eukaryotic CSK. On the one hand, there are microtubules, which consist of 13 parallel polar polymer chains forming a hollow tube. The subunit of microtubules is a heterodimer called tubulin. Microtubules have a persistence length in the range of *mm*s and therefore are very rigid. Often microtubules are found organized by the centrosome, an organelle (=a special subunit of the cell), as a spindle with their minus ends in the center. microtubules mainly serve as tracks for cellular transport, when the MPs kinesin and dynein walk along them and carry cargo [1]. On the other hand, intermediate filaments are in contrast to actin filaments and microtubules not polar. Intermediate filaments consist of related proteins like vimentin, lamin, and keratin, in size are between actin filaments and microtubules, and are much more resistant to strain than actin filaments and microtubules. If a eukaryotic cell is under large external tension in an epithelial sheet, it is the intermediate CSK which maintains its integrity [1, 12, 13].

1.1.2 Adherent Tissue Cells

Multicellular organisms consist of different tissues, which their cells organize into. Major tissue types are connective, epithelial, muscle and nerve tissue. Connective tissue (CoT) is build by a filamentous network of different proteins called extracellular matrix (ECM), compare Fig. 1.4. The ECM proteins are macromolecules, as e.g. collagen, which provides the ECM's mechanical strength, and elastin, which guarantees

(a) 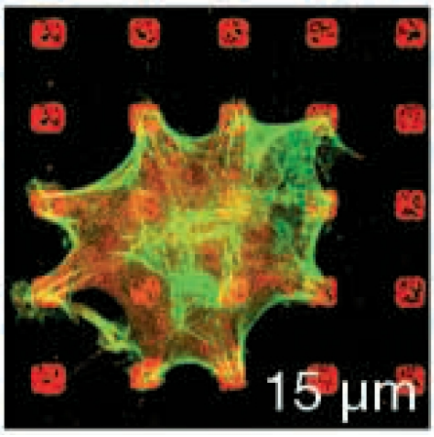

(b) 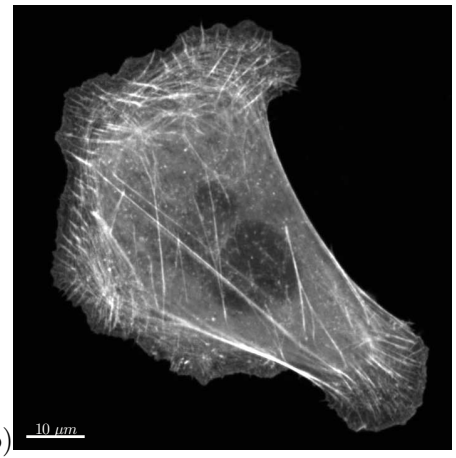

Figure 1.5: Actin-stained cell images. (a) Actin-stained image for a B16 cell on a micropatterned substrate. Actin is shown in green. Red dots consist of fibronectin and are spaced by 15 μm. Taken from [14]. (b) Actin-stained image of a human osteosarcoma cell. Courtesy of J. Stricker and M. L. Gardel.

the ECM's elasticity. They are secreted by special cells which are widespread into the tissue, the fibroblasts [1]. Due to the action of contractile bundles and stress fibers fibroblasts are highly contractile. In contrast to connective tissue, epithelial tissue (ET) is formed mainly by epithelial cells which directly adhere to each other via adhesion belts and to a thin underlying extracellular layer, the basal lamina, see Fig. 1.4. That is, ET is based on cell-cell adhesions whereas CoT is based on cell-matrix adhesions. In this thesis we mainly discuss CoT (abbreviated as tissue), fibroblasts, and cell-matrix adhesions, because these mechanically are very active [1].

It is assumed that tissue cells adherent to two-dimensional substrate surfaces act similar as in the ECM. Therefore, in cell experiments, this situation is studied extensively. If a tissue cell is placed on such a 2D surface, it usually spreads over a certain area, thereby becoming very flat. After spreading, contractile cell shapes can be observed. If the surface is coated with the appropriate protein, the cell adheres to the substrate. The Bastmeyer Lab (Karlsruhe Institute of Technology, Germany) is well-known for their work on micropatterned substrates [14, 15]. On these substrates cells can adhere to special protein dots, which are regularly distributed on the surface. In Fig. 1.5(a) we show a B16 mouse melanoma cell on a micropatterned substrate investigated by the Bastmeyer Lab [14]. Experimentalists from the Gardel Lab (University of Chicago, IL, USA) study cells on elastic substrates coated with a special protein [16, 17]. Fig. 1.5(b) gives the image of a human osteosarcoma (U2OS) cell on a polyacrylamide substrate. For the experimental protocol see [16]. Both cells, Fig. 1.5(a) and (b), are labeled (another term for this is stained) with the appropriate agent to highlight actin filaments. Therefore signal intensity can be assumed as proportional to actin filament

density. Both images show that actin filaments are present throughout the whole cell. In particular, the U2OS cell shows a dendritic actin network.

Note the elongated structures of high actin filament density. These are the stress fibers, contractile actin bundles held together by α-actinin and myosin II, which appear as periodic patterns in an alternating order [18]. Actin filaments in SFs are not always oriented in an anti-parallel fashion. Therefore, the mechanism of contraction and the question of SF contraction at all is not completely understood. There are three classes of SFs [19]: Dorsal stress fibers (DSFs) can grow from FAs near the cell boundary towards the nucleus with an inclination angle of $0° - 90°$ relative to the substrate. Two DSFs of opposing directions can become connected at their ends. Contraction of this structure moves it down to the cell bottom. The outcome, ventral stress fibers (VSFs), thus are straight and assumed to contract in a sarcomere-like fashion. Members of the third kind of SFs, transverse arcs (TVAs), usually are oriented parallel to the cell edge. During time, TVAs move towards the nucleus where they disassemble. TVAs are assembled as connections of short actin bundles or from pre-existing actin networks. Hence, it is possible that two DSFs first connect to the same TVA to subsequently form a VSF [18]. The formin mDia polymerizes the actin filaments in SFs. Hence, inhibition of mDia dramatically reduces the amount of SFs in cells.

There are several ways to manipulate the actin and myosin II in cells. For example, the drugs Y-27632 and blebbistatin both inhibit myosin II mediated contraction of actin bundles in cells. The first one, Y-27632, blocks phosphorylation of myosin light chains [20]. The second one, blebbistatin, binds to the ATPase part of myosin, thereby disturbing ATP consumption of myosin II [21].

1.1.3 Interactions between CSK and ECM

It has been shown that adherent cells actively explore the geometry and stiffness of their adhesive environment and respond to it [22]. Migrating fibroblasts, for example, prefer a certain rigidity of the underlying substrate. Hence, they exhibit a directed movement along stiffness gradients. This process is called durotaxis. Migrating fibroblasts play an important role in wound healing. They migrate to the site of injury to build up new epithelial tissue to close the wound [23]. These special fibroblasts, which are involved in wound healing, are called myofibroblasts which can differentiate from less developed fibroblasts [23]. This differentiation is effected by environmental stiffness, too [22]. Substrate geometry and stiffness can also kill the cell or influence its ability to grow or divide (the generic term is proliferation) [6, 22]. Inhibition experiments for both, actin and myosin II, have shown that active contractility is crucial for force sensing and response [22]. There is already much insight into these sensing capabilities of cells [24–26], but it is still unknown how a cell coordinates force generation, how these forces are distributed inside a cell and how a cell senses force over its full body.

Although it is a standard procedure in experiments to block force generation and propagation with chemical inhibitors or by RNA interference [27], it is very difficult to measure how force is distributed inside cells and between cells and their environment. Different experimental approaches have been developed to meet this challenge. Trac-

tion force microscopy (TFM) became very popular during the last decade [17, 28–32]. This technique allows to measure the forces cells transmit to the substrate via focal adhesions. To this end, tissue cells are placed on elastic substrates decorated with marker particles, e.g. fluorescent beads. If cells adhere and subsequently apply traction forces, the substrate is deformed and thus, the markers are displaced. To obtain the traction strain field the markers' positions have to be measured twice. First, with a contractile cell adherent to the substrate and second, after the cell was removed from the substrate. Cell removal can be achieved by adding the enzyme trypsin, a process called trypsinization [32]. The remaining step, traction force reconstruction [17], we will briefly discuss in the next chapter.

Recently TFM has been extended in such a way that also cell-cell forces can be estimated from cell-matrix forces [33, 34]. However, it is important to note that many forces balance inside the cell and are not transmitted to the substrate, so the forces existing inside cells might be much higher than appreciated from TFM [35]. Laser cutting allows to estimate forces from the mechanical relaxation after cutting load-carrying elements like microtubules in the mitotic spindle [36, 37] or stress fibers in the actin cytoskeleton [38–41]. Laser ablation can be used for subcellular analysis of cortical tension [42]. However, these experiments only probe local relaxation events of prominent cytoskeletal structures and therefore might miss the global effects of more distributed and less visible structures. Micromanipulation can be used to distort the mechanical balance of the cell globally [43–46], but the resulting changes in force distribution can only be estimated indirectly from its effects, e.g. growth of focal adhesions. To achieve a more systematic understanding, these experimental approaches have to be complemented by theoretical models.

1.1.4 Mechanical Stability of Cytoskeletal Networks

Recent evidence suggests that cytoskeletal networks often operate at the verge of mechanical stability. As an example for this, SFs have been shown to get elongated under stress and subsequently thin down. This is often accompanied by damages which can lead to SF failure. Failure can be averted by a repair mechanism which involves the protein zyxin [41]. Another example is given by epithelial cells under external mechanical load. At low strain, actin filaments are the main contributors to maintain the CSK's integrity. But if strain is increased, the actin filaments rupture and the intermediate filaments carry the load, because intermediate filaments can bear far more strain than actin filaments [12, 13, 47]. Molecular dynamics (MD) simulation of the intermediate filament network revealed that the α-helix turn contributes mainly to the intermediate CSK's integrity, even if the network is damaged [48]. On the scale of tissues there is the ECM, which cannot bear the same amount of strain as its strongest components elastin and collagen [49]. Using theoretical network models it was found that the weaker proteoglycans weaken the whole material and lead to failure of the ECM [50].

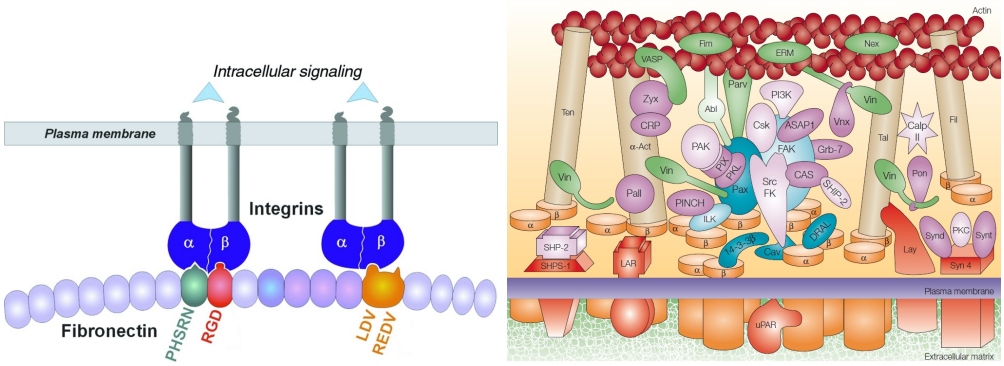

Figure 1.6: Focal adhesions. (a) Simplified view of the integrin-fibronectin binding. Figure was taken from [51]. (b) Cartoon of the complex network of proteins which builds up a focal adhesion. Taken from [52].

1.1.5 Focal Adhesions

FAs are based on weak interactions between transmembrane proteins, mainly integrins, which link the actin CSK to extracellular space, and corresponding binding partners in the ECM. In case of fibroblasts the ECM protein fibronectin acts as a ligand for the integrin receptors [1]. However, integrins can also bind to collagen or to several other proteins [53]. Fibronectin binds to a distinct binding pocket of the integrin molecule, see Fig. 1.6(a). This non-covalent connection is called a bio-molecular bond, which is built by weak hydrogen bonds or van-der-Waals interactions. As a consequence, noise, i.e. thermal fluctuation, is sufficient to open the bond. Thermal fluctuations are always present in living matter, since it is usually operated at the body temperature of $\sim 40°C$. To maintain the tissue's physical integrity bio-molecular bonds are able to close again, often a bond closes which recently opened. During cell migration, for example, rupture of focal complexes is indispensable for retraction of the cell body. Focal complexes are cell-matrix adhesions, which have not matured to FAs, yet. We can state: There is rupture and rebinding present for all times. Beyond integrin and fibronectin a variety of cellular proteins, such as vinculin, talin, paxillin, and α-actinin are involved in forming a FA [52], see Fig. 1.6(b). It is impossible to probe FAs by force and to assign changes in force or length to single bonds in this complex network. Indeed, FAs often do not break at the integrin-fibronectin bond, but somewhere inside this complex network [54]. This shows that among these weak connections, the integrin-fibronectin bond is one of the strongest.

1.1.6 Force Spectroscopy of Single Bio-Molecular Bonds

Single bio-molecular bonds have been under exhaustive investigation [55]. Bio-molecular bonds do not only appear in FAs, but also play an important role e.g. in rolling adhesion of leukocytes, i.e. white blood cells, at the blood vessel wall [56], and for titin,

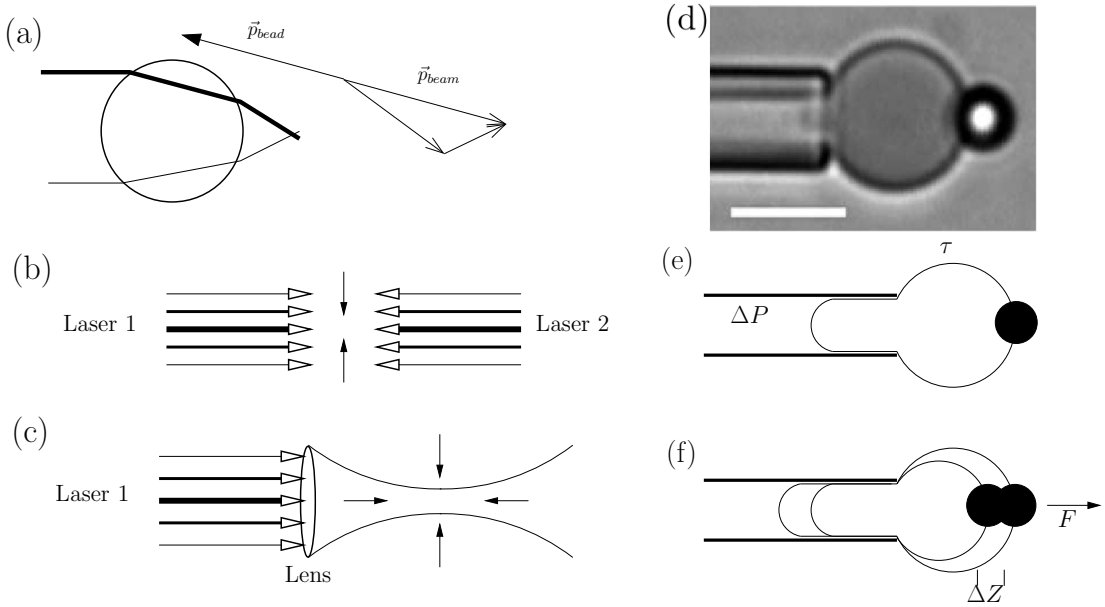

Figure 1.7: Laser optical tweezers and biomembrane force probe. (a)-(c) Laser optical tweezers (LOT). If a laser beam hits a small bead, the bead gets a momentum with a component in the direction of high intensity. This can be used to move the bead, either using two unfocused lasers (b), or a focused laser beam (c). (d)-(f) Biomembrane force probe (BFP). (d) A red blood cell subject to aspiration by the pipette on the left. Scale bar 5 μm. Taken from [55]. (e) Schematic view of the situation with the important physical properties here, namely the pressure Δp inside the micropipette and the surface tension of the RBC. (d) Suction deforms the RBC while displacing the bead and pulling on the bond.

the actin connector in sarcomeres [57]. Therefore, these have been subject to extensive research for the last 15 years and still are. Bonds usually are probed in pulling experiments. Measured forces often are on the scale of pN and lengths on the scale of nm [55, 58]. Hence, reliable measurements depend on the resolution power of the measuring equipment and thus, on the technical progress. Prominent techniques used today are atomic force microscopy (AFM) [59], laser optical tweezers (LOT) [60, 61], and biomembrane force probe (BFP) [62].

AFM is a widely used variant of scanning probe techniques [59]. A probe tip on an elastic lever arm, a cantilever, scans the surface of a sample in a very close distance ($< 100nm$). Interactions between sample and probe, as e.g. van-der-Waals forces, repulsive forces, adhesion forces, or electrostatic forces, lead to cantilever deflections. To measure these deflections a laser beam is reflected at the cantilever's backside. The signal of the reflected beam is detected by a photo diode [63]. For force spectroscopy the AFM is not moved laterally to the surface, as it is done for topography analysis. Instead, the probe tip is brought in contact with the sample. After a certain waiting time, a bond has formed. If the cantilever is now pulled away from the sample the

bond is stretched. That way, the force which is necessary to break the bond as well as the length the bond is elongated can be determined [55].

With LOTs, which can consists of either one laser or two lasers, small dielectric particles (dimensions < laser wave length) can be moved through the medium. Theoretically, a laser beam can be subdivided into infinitely many thin laser beams in parallel. The closer to the center of the beam the larger the intensity of such a small laser beam. If an unfocused laser beam hits a small bead, the bead gets a momentum towards the center and away from the laser source, Fig. 1.7(a). To fix the small bead either a focused laser can be used, which drags the bead towards the laser focus, see Fig. 1.7(b). Alternatively, two opposed lasers can be used to trap the bead in the center between them, compare Fig. 1.7(c) [55].

In BFP experiments two microbead surfaces are decorated with receptors and ligands, respectively. One bead is fixed while the other is glued to a red blood cell (RBC). Mature RBCs lack a nucleus and basically consist of the plasma membrane only. This three-dimensional network is built up mainly by the cytoskeletal protein spectrin [1]. The RBC is then aspirated by micropipette suction, i.e. a pressure is applied which pulls the RBC inwards the micropipette, see Fig. 1.7(d-f). From pressure and RBC deformation one can calculate the force on the bonds between the beads and the stretching length [55].

1.2 Theoretical Treatment

1.2.1 Static Network Models of Adherent Tissue Cells

The mechanical properties of cells, ECM and CoT are strongly determined by filamentous networks of proteins like the aforementioned actin, tubulin, lamin, spectrin or collagen. Therefore, mechanical networks are widely used theoretical models for cell and tissue mechanics [7, 64]. One of the best studied cases is the RBC, whose shape and mechanics have been studied with network approaches in very large detail [65–73]. Modern computer power permits to simulate each of the roughly 10^5 spectrin links separately and with molecular detail, for example using the appropriately parameterized force-extension curve of a semiflexible polymer [71]. In the limit of small extensions, these models usually reduce to Hookean networks.

For adherent cells, the main structural determinant is the actin cytoskeleton, whose mechanics differs in several important aspects from the one of the spectrin network of RBCs. In general, the molecular structure of the actin network is much less defined. Its most prominent feature in adhesion is strong contractility due to activity of myosin II motors. This observation implies that the mechanical links between the nodes of the network cannot be simple actin filaments, but have to be bundles of actin filaments cross-linked and tensed by myosin II motors. The simplest model for prestress in a mechanical network is the introduction of a finite resting length which is smaller than the typical extension of each link. Indeed, one- and two-dimensional spring networks with prestress are widely used for modeling cell migration [74–77].

Network models are conceptually very appealing due to their multi-scale nature: by changing the microscopic rules for the mechanics of the links, one can explore how the macroscopic behavior of the whole network changes. In particular, important biological effects like viscoelasticity of the links or coupling to diffusion fields can be incorporated [71–77]. Spring networks offer the additional advantage that homogenization techniques can be used to arrive at continuum models [78]. Recently, the interplay between force generation and the geometrical and adhesive properties of the environment have been addressed using the powerful framework of finite element method (FEM) models [79], which can be considered as the continuum limit of appropriate network models. Most FEM models use constitutive equations which correspond to Hookean networks.

Although conceptually very appealing, modeling cell mechanics with Hookean networks does not reflect the fact that the actin cytoskeleton does not provide much resistance to compression. This is especially true for two-dimensional networks for cell adhesion and migration, because in this case the network might contract laterally, while the cytosol flows into the third dimension. In this situation, the network links do not behave as springs, but rather as cables, which are characterized by an asymmetric force-extension relation. There are several microscopic reasons for this effective behavior: not only do thin actin bundles easily buckle under load, they also tend to telescope in due to filament sliding and even to depolymerize once tensile stress is released. Cable networks have been successfully used to model the prestress-dependent mechanical response of adherent cells to local mechanical perturbations [80]. The same model has also been used to describe how mechanical stress is propagated from the nuclear region through the cytoskeleton towards focal adhesions, where changes in load lead to changes in adhesion size [44].

One striking feature of strongly adhering cells is the fact that retracted contours often take the shape of circular arcs [14, 15, 81, 82], see the B16 cell shown in Fig. 1.5(a) for an example. Although for cable networks the resulting shapes are strongly invaginated, it has been shown that the circular invaginations observed for cells pinned at discrete sites of adhesions can only be explained if an additional contractile force is introduced for each mechanical link [15]. This additional force in an actively contracting cable network does not vanish at the resting length and represents the fact that contractility arises mainly from myosin II motors, which in steady state operate close to their non-vanishing stall force.

1.2.2 Dynamic Network Models of Fracture

In continuum mechanics a crack in a homogeneous material is modeled as a boundary condition for the strain field. The crack will grow and finally lead to failure of the material, if it is energetically favorable [83]. However, fracture is often the result of inhomogeneity in the material. A crack can nucleate from a weak spot and grow to lead to global material failure. Therefore inhomogeneity or disorder must be taken into account for fracture studies. This can be done very nicely by network models for material failure, which are widespread in engineering application, e.g. for bridges,

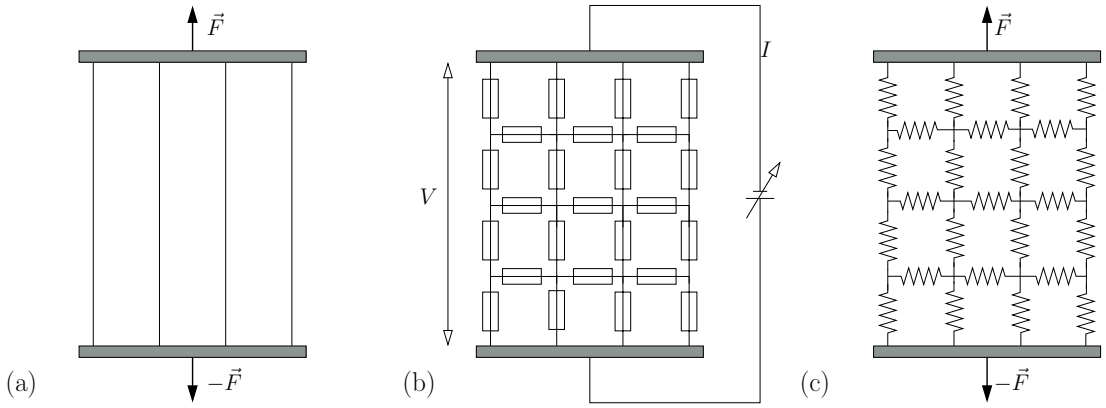

Figure 1.8: Sketch of the different models for fracture. (a) The fiber bundle model (FBM), a bundle of parallel fibers of (uniformly) distributed force thresholds. Increasing load $\vec{F}$ leads to fiber breakage. Force redistribution can be globally (over all remaining fibers) or locally (only neighboring fibers). (b) The random fuse model (RFM), a network of electric fuses with (uniformly) distributed current thresholds. Increasing voltage V leads to increasing current I and subsequently to serial burning of the fuses. (c) The random spring model (RSM), the vectorial counterpart of the RFM. A network of springs with (uniformly) distributed force threshold. Increasing displacement of the two attachments at the top and at the bottom leads to increasing forces in the springs and subsequently to serial breakage of the springs.

houses, or cars [84]. In computer simulations of such materials, the network bonds are allowed to rupture. Disorder can be introduced in two ways. On the one hand, a regular network topology can be disturbed by random dilution of a fraction of the bonds before starting the simulation. In this case all network bonds have the same force threshold. If the force in the bond exceeds the threshold the associated bond is irreversibly removed. On the other hand, one can determine force thresholds from a given distribution for bonds on a regular network, like e.g. in [48, 50].

There are extensive MD approaches to the mechanisms of fracture [85], also applied on biological materials using network models [48]. Buehler and co-workers emphasize the hierarchy of failure and the link between atomic and mesoscopic scales [86]. However, the most basic model studied in fracture mechanics is the one-dimensional fiber bundle model (FBM) [87]. A fiber bundle consists of a set of parallel fibers under mechanical load, see sketch in Fig. 1.8(a). These fibers have distributed force thresholds. If one fiber breaks, the force is redistributed among the remaining fibers. There can be equal load sharing, i.e. the load which was carried by the removed fiber is shared by all the remaining fibers. Alternatively, local load sharing can be studied: only the neighboring fibers carry the load of the broken one. The FBM has the advantage that it can be treated analytically.

2D or 3D materials of different elastic properties exhibit different failure properties. Two extreme cases can be easily distinguished. On the one hand, we have brittle failure

of e.g. concrete, which does not deform very much before it breaks. On the other hand, e.g. tissue or epithelia can be elastically deformed, and therefore show ductile failure.

Brittle failure is analyzed via an enhancement of the FBM, the random fuse model (RFM) [84], in which a hard material is modeled as a dense square shaped network of electric fuses, Fig. 1.8(b). The fuses have uniformly distributed current thresholds. In the RFM mechanical load is modeled as voltage which is increased step-wise between two parallel sides of the network. In the RFM equilibration is assumed to be faster than the burning of a fuse.

A less prominent model used in common fracture studies is much closer related to biological materials. The random spring model (RSM) [88], which is used to study ductile failure, can be interpreted as the vectorial counterpart of the scalar RFM. In the RSM the fuses are replaced by springs, the voltages by spatial displacements, the currents by mechanical forces, and the current thresholds by force thresholds, compare Fig. 1.8(c). Remarkably, the statistical properties of RFM and RSM are very similar [88].

Failure of bond networks can be interpreted as a first-order phase transition [89]. Take the RFM with distributed current threshold for example. If voltage is increased, small cracks form. These cracks grow until a spanning crack has formed and the network has failed. This is strongly reminiscent of forming droplets in the gas-liquid transition (condensation), which grow until the gas has condensed. In [89] the avalanche size distribution is calculated with a mean-field theory of an Ising-like model. An avalanche is a series of secondary rupture events which follow the rupture of a single (primary) bond. Before the fatal avalanche leads to material failure, avalanches can appear as precursors. Critical exponents are defined, similar to those in first-order phase transitions [89]. Nevertheless, it is still under debate, if the scaling laws found in network models of fracture can be related to a critical point [84].

1.2.3 Rupture of Bio-Molecular Bonds

In contrast to the fracture models discussed above, bio-molecular bonds are modeled with Kramers escape theory, which was already developed in the 1940s to model chemical interactions as a stochastic process [58, 90]. It describes particles initially bound to an energy minimum, which they can diffusely escape. If a force is applied, the escape path is directed because it simply follows the force. Hence, escape can be described by a one-dimensional reaction coordinate x. Fig. 1.9 shows such an energy landscape as a double well potential. In order to escape the minimum at $x_{m,1}$ the particle must get over the energy barrier $\epsilon_{b,1}$ at $x_{b,1}$. In the absence of force, this can only happen stochastically due to thermal fluctuations. If a force F is applied to the bond, the energy barrier at $x_{b,1}$ is lowered to $\epsilon'_{b,1} = \epsilon_{b,1} - Fx$ so the particle can overcome the barrier to reach $x_{m,2}$ on a faster time-scale. Now the bond is open, though it can close, rebind, again. This process is assumed to not depend on the pulling force, therefore the rebinding rate γ is constant. The form of the potential depicted in Fig. 1.9 implies that a particle will never return after getting over the second energy barrier at $x_{b,2}$. Similar to protein unfolding [91], there can exist several energy barriers corresponding

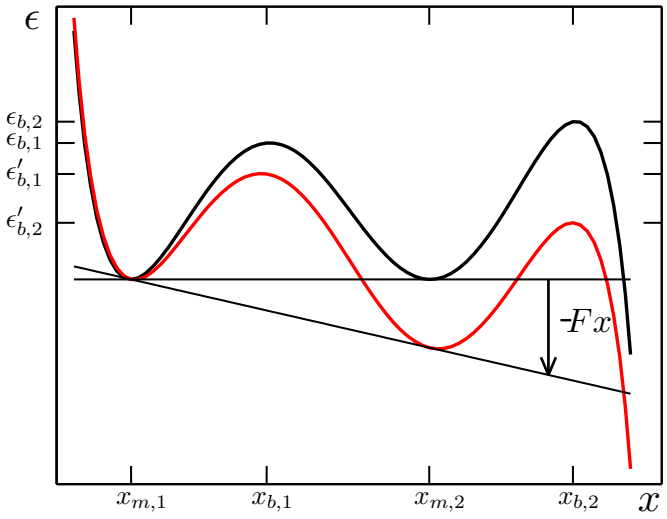

Figure 1.9: Double well potential as function of the reaction coordinate x. At $F = 0$ (top line) the particle at $x_{m,1}$ must cross the barrier $\epsilon_{b,1}$ at $x_{b,1}$. If force $F > 0$ is applied, the barrier is lowered down to $\epsilon'_{b,1} = \epsilon_{b,1} - Fx_{b,1}$. If the particle reached $x_{m,2}$, we have the same situation. But rebinding (transition from $x_{m,2}$ back to $x_{m,1}$), which is independent of force is possible.

to several groups of hydrogen bonds which rupture serially. The escape rate ρ according to Kramers theory is given by [92]:

$$\rho \sim e^{-\frac{\epsilon_{b,1}}{k_B T}}. \tag{1.1}$$

Application of a force F lowers the energy barrier down to $\epsilon_b - Fx_{b,1}$ as discussed above. With constant $\epsilon_{b,1}$ we have

$$\rho \sim e^{\frac{F}{F_0}}, \tag{1.2}$$

with $F_0 = k_B T / x_{b,1}$. Here, k_B and T denote Boltzmann constant and temperature, respectively. This equation was already used by Bell [93] and is therefore referred to as the Bell equation. Studies of the rupture of single bonds were performed by Evans and co-workers [92, 94]. More recently, Erdmann and Schwarz discussed the stochastic behavior of idealized adhesion clusters, which consist of many bonds in parallel [95]. But in FAs *in vivo* bonds are not all in parallel, they can be arranged into very complex networks as illustrated in Fig. 1.6(b).

The adhesion clusters discussed by Erdmann and Schwarz [95] and the FBM are very similarly composed. However, the physics behind bond behavior is fundamentally different. Bio-molecular bonds disintegrate during time due to thermal fluctuations. They rupture stochastically if a force is applied. Therefore the bond strength, the most frequent force the bond ruptures at, increases with pulling speed. All these biologically very relevant features cannot be included in threshold-based models of fracture. The assumption of force thresholds leads to a deterministic and not stochastic behavior of the system. However, there are recent studies, which already incorporate repair [96], similar to the rebinding mechanisms in the work by Erdmann and Schwarz.

1.3 Synopsis of the Thesis

The aim of this thesis was to study different network models for the actin CSK. On the one hand we were interested in a deep understanding of the equilibrium shapes of the networks, in regard of bond mechanics, topology, size, and geometry. On the other hand we wanted to compare the rupture dynamics of bio-molecular bond networks to the results of classical fracture studies. To this end we proceed as given here.

In **chapter 2**, we first introduce the different network models for adherent cells (spring models, cable networks, and actively contracting cable networks). Furthermore we show the network topologies which will be used. We stress the point, that the two seemingly different subjects of this thesis can be analyzed in the same framework. We also present the way we model stress fibers. Dorsal stress fibers and transverse arcs are integrated into the network while ventral stress fibers are assumed not to feel the other filaments which cross them. Then we introduce the rate-based rupture of the filaments according to the Bell equation. Two different loading protocols will be used: Constant displacement of the network sides and linearly increasing displacement. We discuss traction force reconstruction and how the deformation of a substrate can be calculated. Finally, we show the numerical algorithms used in this thesis. The algorithms which are used: conjugated gradient method to calculate the network equilibrium, GrowCut for image segmentation, MeshGrid for triangulation, and a tree-based algorithm for percolation.

In **chapter 3**, we systematically compare the different network models for adherent cells in regard to the predicted shapes and force distributions. Our main conclusion is that actively contracting cable networks share many interesting features with adherent cells. Due to their linear nature, actively contracting spring networks are equivalent to passive spring networks with a reduced resting length. Passive networks (both from springs and cables) have a well-defined reference state even in the absence of adhesion constraints and in general give similar results regarding shape and force distribution, which is determined mainly by global inputs like the spatial distribution of the adhesion points. In contrast, actively contracting cable networks do not have a well-defined reference state because without adhesion constraints, they contract onto a point. In this case, we find that shape and force distributions are determined mainly by the local distribution of adhesion sites. The internal force distribution is constant in the bulk and strongly localizes to the contour, where forces jump by orders of magnitude. This motivates a detailed study of two contour models, which allow us to derive analytical predictions which we then compare with the results from the computer simulations. We also discuss how actively contracting cable networks can be extended to model also non-linear or adaptive linker mechanics, and comment on the relation of our network models to tissue mechanics. Large part of **chapter 3** has been published before in [97].

Chapter 4 reports the application of the active cable model to experimental TFM data. We study 3 different cell types. Namely Madin-Darby canine kidney (MDCK) cells, mouse 3T3 fibroblasts, and human osteosarcoma (U2OS) cells. MDCK cells do not show stress fibers, therefore they are sufficiently described by the motor force density

of the network bonds only. In contrast, U2OS cells and 3T3 fibroblasts contain SFs. Therefore these must be modeled with different motor tensions. Finally, we show that myosin II inhibition leads to a decrease in motor tension in SFs.

In **chapter 5** we extended the static network models to dynamic models of bonds which stochastically break. The unstrained network can then be understood in the framework of percolation theory. For networks under prestrain we analyze the statistical properties of fracture. The second part of this chapter is dedicated to linearly increasing strain. We find that the statistical properties of dynamic networks differ from the threshold based fracture networks used for hard macroscopic materials.

2

Models & Algorithms

Tissue cells adhering to a planar substrate via discrete adhesion points usually become very flat and therefore effectively two-dimensional. Only the nucleus, which rises in the middle, makes them fully three-dimensional, see sketches in Fig. 2.1(a,b). However, here we focus on lateral contraction and contour effects and thus the nucleus is expected to play a minor role. In the following we therefore restrict ourselves to two dimensions and model the cytoskeletal network as a two-dimensional mesh of mechanical links joined at N discrete nodes. Nodes are labeled with single indices, i and j. Microscopically links and nodes may represent filament bundles and local accumulations of cross-linkers, respectively, but in a more general sense, these mechanical elements are simple representatives of an unknown network architecture which we model in a statistical sense. The network is subject to internal forces originating from molecular motor activity, $\vec{F}_{active}$, and the mechanical resistance of filaments to strain, $\vec{F}_{mech}$, compare Fig. 2.1(c).

2.1 Bond Mechanics

We introduce three fundamentally different kinds of mechanical models for the network bonds (in this thesis the terms link and bond are equivalent). The simplest case is a *Hookean spring network* (HSN) composed of links with resting length L_0, which represent linear springs with spring constant EA/L_0, where E is the Young modulus of the link and A its cross-section. The restoring force acting on a node i due to elastic strain in the link ij then reads:

$$\vec{F}_{ij,mech} = EAu_{ij}\vec{e}_{ij}, \tag{2.1}$$

where $\vec{e}_{ij} = (\vec{R}_j - \vec{R}_i)/L_{ij}$ is the dimensionless unit vector along the link ij. Here, $\vec{R}_i$ and $\vec{R}_j$ specify the node positions, $L_{ij} = |\vec{R}_i - \vec{R}_j|$ is the length of the link and $u_{ij} = (L_{ij} - L_0)/L_0$ is the strain in the link. The force-extension curve of a single link in a HSN is shown in Fig. 2.1(d) as a dashed line with short dashes.

The mechanical properties of the cytoskeleton are attributed mainly to the actin part. Actin is a semi-flexible filament prone to buckling under compression and thus

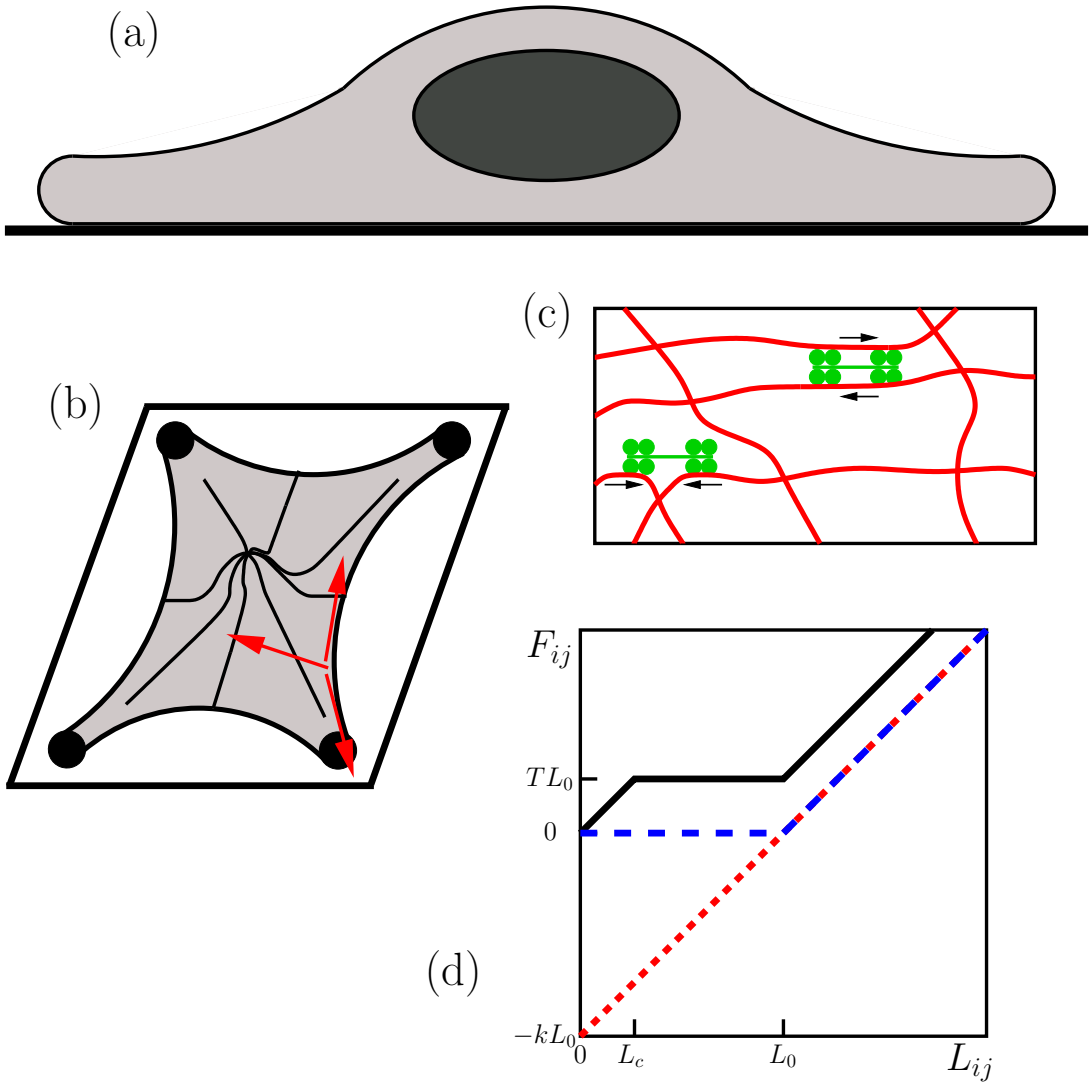

Figure 2.1: Sketch of the system. (a) Side-view of an adherent tissue cell. (b) Top-view. The cell is assumed to be adherent at four discrete dots. Its contour shows inward directed shapes resulting from a force balance between inward directed forces and forces in the boundary. (c) The actin cytoskeleton is tensed by myosin II minifilaments, which actively contract the network with forces $\vec{F}_{active}$. If the network links are strained, restoring forces $\vec{F}_{mech}$ appear. (d) Force-extension curve $F_{ij}(L_{ij})$ of a link ij in a simple Hookean network, a passive cable network, and an active cable network (in order of increasing dash lengths). (k = spring constant, T = motor stall force per length, L_0 = initial link length, L_c = critical length)

behaves like a cable, which can be stretched but not compressed. The Hookean assumption of a symmetric elastic response is therefore not valid. The mechanical properties of actin networks on a coarse-grained scale are more accurately described by assuming a finite resistance of filaments to tensile strain, $u_{ij} > 0$, but no resistance to compressive strain, $u_{ij} < 0$. The mechanical restoring forces originating from a link connecting two nodes i and j in the *passive cable network* (PCN) are therefore given by:

$$\vec{F}_{ij,mech} = \begin{cases} EAu_{ij}\vec{e}_{ij}, & L_0 < L_{ij} \\ 0, & L_{ij} \leq L_0 \end{cases} \tag{2.2}$$

We show the force-extension relation of the PCN links in Fig. 2.1(d) as a dashed line with long dashes.

Let us assume that myosin II motor proteins are homogeneously distributed in the network. Because they are arranged in a parallel fashion, their individual forces add up. We therefore assume that a link contracts with a force TL_0 proportional to its length, where T is force per length. We also assume that this force does not change as the filament bundle contracts, because the number of active motors does not decrease. For a link ij we therefore have:

$$\vec{F}_{ij,active} \;=\; TL_0\vec{e}_{ij} \;, \tag{2.3}$$

where $T > 0$ is the tensile force per initial length applied by the motors. The finite force at zero length is unphysical and we avoid it by introducing an additional rule such that force is diminished if two neighboring nodes come closer to each other than some small distance $L_c \ll L_0$:

$$\vec{F}_{ij,active} \;=\; TL_0\frac{L_{ij}}{L_c}\vec{e}_{ij}, \qquad L_{ij} < L_c. \tag{2.4}$$

Combining PCN and active contraction, we obtain what we call the *active cable network* (ACN), compare the solid line in Fig. 2.1(d):

$$\vec{F}_{ij} = \begin{cases} \left(TL_0 + EAu_{ij}\right)\vec{e}_{ij}, & L_{ij} < L_0 \\ TL_0\vec{e}_{ij}, & L_c \leq L_{ij} \leq L_0 \\ TL_0\frac{L_{ij}}{L_c}\vec{e}_{ij}, & L_{ij} < L_c \end{cases} \tag{2.5}$$

Neither the detailed choice of L_c nor the assumption of a linear force reduction below L_c are crucial for our results.

Active contraction can also be combined with the HSN. However, this simply shifts the straight dashed line in Fig. 2.1(d), i.e. reduces the HSNs resting length L_0 to

$$L_0' = L_0\left(1 - \frac{TL_0}{EA}\right). \tag{2.6}$$

Please note, Eq. (2.6) is only valid for $TL_0 \leq EA$. In this case it is analogous to the common HSN with resting length L_0'. Therefore we may set $L_c = 0$. In the following this network type is not explicitly discussed anymore.

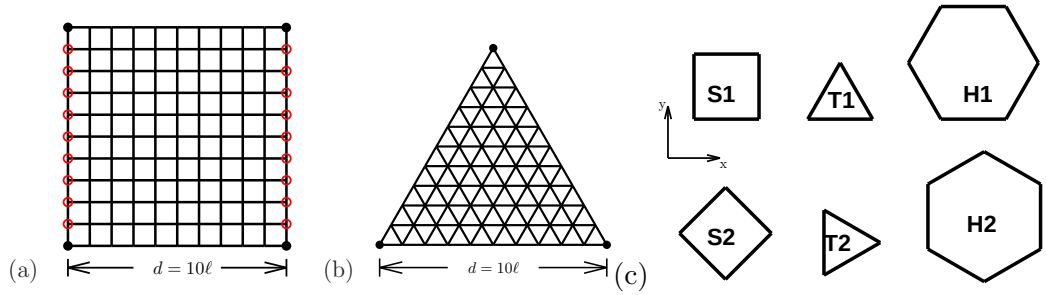

Figure 2.2: Tension-free reference states and topologies under consideration. (a) Square network with link length $\ell = 1$ and side length $d = 10\ell$. (b) Triangular network with the same ℓ and d. (c) Unit cells of the topologies under consideration. Link length is $\ell = 1$, irrespective of topology.

To reduce the number of parameters, we scale all lengths with respect to L_0, e.g. $\ell = L/L_0$. All forces are scaled as $f = F/EA$. We define the ratio of active to elastic forces as

$$\tau = \frac{TL_0}{EA} \ . \tag{2.7}$$

For an ACN we therefore may rewrite the forces acting on a node in the non-dimensionalized form as:

$$\vec{f}_{ij} = \begin{cases} (u_{ij} + \tau)\vec{e}_{ij}, & 1 < \ell_{ij} \\ \tau\vec{e}_{ij}, & \ell_c \leq \ell_{ij} \leq 1 \\ \tau\frac{\ell_{ij}}{\ell_c}\vec{e}_{ij}, & \ell_{ij} < \ell_c \end{cases} \tag{2.8}$$

In the computer simulations we use $\ell_c = 10^{-3}$.

2.2 Stress Fiber Modeling

In chapter 4 we extend the network model of the cytoskeleton by inserting inhomogeneity into the network. Hereby, we distinguish four different kinds of network bonds. Normal bonds which represent simple filament bundles, have a motor force density of τ. These do not interact with ventral stress fibers, which we model as single long bonds ranging from one fixed node (FA) to another. VSFs are subject to a tension density $\tau_v \approx \tau$. In contrast, dorsal stress fibers and transverse arcs are modeled as sets of serially arranged network links in the network. These serial structures are obtained with fixed points in DistMesh, see below. We will later justify the assumption $\tau_d \approx \tau_t \gg \tau \approx \tau_v$.

2.3 Network Geometry and Topology

The two main issues of this thesis, cell shape analysis and rupture dynamics of networks, both are treated in the framework of network mechanics of different topologies. We

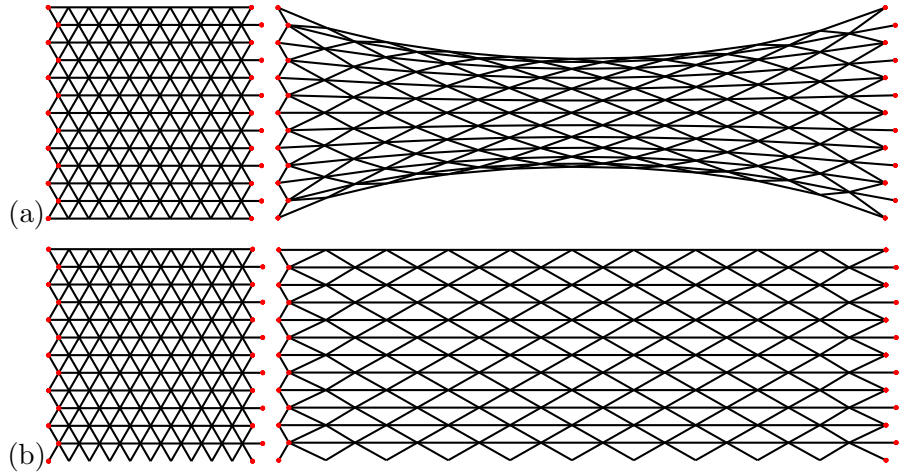

Figure 2.3: Triangular network T1 - relaxed vs. prestrained. (a) Free boundary conditions (FBC). In equilibrium normal stress to upper and lower boundary is zero. (b) Periodic boundary conditions (PBC). The nodes at bottom and those on top are assumed to be identical. Parameters: Left: strain 0%, right: strain 200%, $L_x = 10$, $L_y = 6\sqrt{3}$, $i = 0.5$, $\ell = 1$.

consider the same regular and irregular topologies for both of them, see e.g. the tension-free reference state of a network in square topology, see Fig. 2.2(a). If cell shape is studied, only the filled dots are kept fixed. If we study rupture, we fix (or displace) the empty nodes as well. We also analyze other simple topologies than the square topology S1, see Fig. 2.2(c) for their unit cells. For shape analysis as well as rupture analysis, mainly the network of square external shape is considered. For network topologies which are not $\pi/2$-periodic (H1,H2,T1,T2) the network height is chosen approximately by its width. Adherent square cells with topologies T2 and H2 are equivalent to those with T1 and H1, respectively, which follow by $\pi/2-$rotation. T2 and H2 are therefore not explicitly discussed in the cell shape related chapter 3 of the thesis. However, for rupturing networks it is a priori not clear whether these topologies give the same results. Therefore, in the rupture related chapter 5 of the thesis we take into account all 6 topologies.

We also analyze an irregular network topology, the Voronoi construction. To construct a 2D Voronoi network we randomly choose n points $\vec{p}_i$, $1 \leq i \leq n$, from any given square $S \in \mathbb{R}^2$ in the xy-plane. The square S can uniquely be fragmented into areas A_i, with $\vec{p}_i \in A_i$ and

$$A_i = \{\vec{x} \in S : |\vec{x} - \vec{p}_i| < |\vec{x} - \vec{p}_j| \quad \forall j \neq i\}. \tag{2.9}$$

The boundary lines of all these areas give the Voronoi construction, which will later be referred to as VO. Since the nodes at the corners of the square not necessarily are among the VO nodes, they must artificially be added. To be able to study contour effects in Voronoi networks, we also draw a square frame around the network.

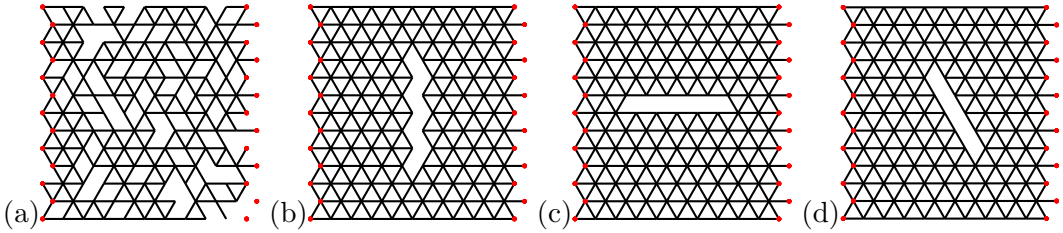

Figure 2.4: Possible predamages to the network. (a) Equally distributed bond removal. (b) Cut parallel to the applied strain. (c) Cut perpendicular to the applied strain. (d) Intermediate cut between (b) and (c). Parameters: $p = 0.4$. T1 network under FBC.

Most of the rupture results presented in chapter 5 are obtained using the T1 network, which has an integer bottom line length L_x. For the simulations we take $L_x = 20 \cdot i$ and $L_y = 12\sqrt{3} \cdot i$ with $i \in \{0.25, 0.5, 1, 2, ..., 11, 12\}$. This gives total bond numbers ranging from $N_{tb} \approx 100$ to $N_{tb} \approx 200000$ for the analyzed networks.

Intuitively, there are two different situations for the free network boundaries on top and at the bottom. If one considers free boundary conditions (FBC), the nodes with initially largest and lowest y-coordinate are allowed to move freely. Without bond rupture these boundaries invaginate but in general do not show a round contour, see Fig. 2.3(a). For periodic boundary conditions (PBC) in y-direction (a cylinder of infinite radius), Fig. 2.3(b), we treat each node at the bottom of the network as if it was identical with the one in the top line which initially has the same x-coordinate.

In order to investigate how the bond network deals with damages, we cut some of the bonds before starting the simulations. Four different kinds of this so-called predamage are studied, see Fig. 2.4. We quantify predamage by the parameter $p \in [0, 1]$. Equally distributed removal of $p \cdot N_{tb}$ bonds from a network with N_{tb} is called the "rand" case, see Fig. 2.4(a). The other damages under consideration are central cuts parallel ("par", see Fig. 2.4(b)), perpendicular ("per", see Fig. 2.4(c)), and under 60°-inclination to the applied strain ("diag", see Fig. 2.4(d)). The cut length is given by $p \cdot d_{\max}$, where $d_{\max}$ denotes the minimal cut length which would lead to loss of percolation. In the case of the T1 network for par we have $d_{\max} = L_x$ and for per $d_{\max} = L_y$.

2.4 Bond Rupture and Rebinding

In chapter 5 we assume that bio-molecular bonds (in particular actin filaments) rupture under force according to a rate τ which is given by the Bell equation Eq. (1.2)

$$\rho_{ij} = \rho_0 e^{F_{ij}/F_0}, \tag{2.10}$$

where F_{ij} denotes the force which acts in the bond between node i and node j, ρ_0 is the rupture rate for vanishing force, and F_0 is the force unit. To reduce the number of parameters, times are scaled by τ_0^{-1} from Eq. (2.10).

The rebinding of a broken bond between two nodes i and j must be time dependent, space dependent, and stochastic. The first is, we introduce a time t_{mem} after which the network has forgotten the bond between i and j, i.e. the network has a finite memory. This accounts e.g. for stress fiber retraction after cutting [40]. Secondly, if the distance between node i and node j, ℓ_{ij} is larger than a maximum rebinding distance ℓ_{max}, rebinding is prohibited. Randomness is introduced via a rate

$$\gamma_{ij} = \gamma = const. \tag{2.11}$$

This gives two additional conditions to stochastic rebinding events. If they all are fulfilled, a new bond is introduced, which connects nodes i and j again. This new bond has the same resting length as the old bond between i and j, ℓ and spring constant EA/ℓ, with EA equal to the other network bonds.

2.5 Algorithms for Clamped Node Displacement

2.5.1 Constant Displacement

In chapter 5 we simulate situations, in which the filled and empty nodes from the networks in Figs. 2.2(a) or 2.3(a,b) left are constantly displaced. In that case we use the so-called *next reaction method* of the Gillespie algorithm [98, 99]. Let us briefly describe it here. Given n possible reactions of a system and their respective rates a_i, $i \in \{1, ..., n\}$, first the sum $a = \sum_{i=1}^{n} a_i$ is calculated. Then the rates are normalized, $a_i^* = a_i/a \ \forall i$, and two random numbers $\xi, \zeta \in [0, 1]$ are drawn from a uniform distribution. The reaction which occurs is reaction j if

$$\sum_{i=1}^{j-1} a_i^* < \zeta \leq \sum_{i=1}^{j} a_i^*. \tag{2.12}$$

The time this reaction occurs is given by

$$t = -\frac{\ln(\xi)}{a}. \tag{2.13}$$

The Gillespie algorithm has two big advantages compared to time discretization. First, it is exact in time. Second, if there is no reaction for a long time, no computation is necessary. Nevertheless, in our simulations we cannot avoid a discretized time running in parallel to the Gillespie simulation in order to get statistics.

We apply the Gillespie algorithm to study the behavior of a prestrained network of molecular bonds. In this context, "prestrain" means that we take the networks shown in Fig. 2.3 on the left, apply a strain $e = 2\delta x/L_x$ by pulling each clamped side a length δx apart and compute the equilibrium. Now we set the system time to zero and keep the clamped nodes fixed during the simulation. In Fig. 2.3 the clamped nodes are shown as dots. Following the Gillespie algorithm, we have reaction rates

$$a_i = \begin{cases} e^{F_i}, & \text{for rupture of closed bonds } i \\ \gamma, & \text{for rebinding of open bonds } i. \end{cases} \tag{2.14}$$

We stop the calculation as soon as the percolation of one clamped side to the other has been lost, at the first passage time in the language of [95].

For constant displacement we apply the following procedure:

1. Apply strain e, equilibration, set system time to zero
2. For each (open or closed) bond i:
   - if i is closed: $a_i := e^{F_i}$ (F_i: force in bond i),
   - if i is open: $a_i := \gamma$ (if additional constraints forbid rebinding set $a_i := 0$).
3. - Set $a := \sum_i a_i$, $a_i := a_i/a$.
   - Draw two random numbers $\xi, \zeta \in [0, 1]$.
   - Add $-\ln(\xi)/a$ to system time.
   - Find j with $\sum_{i<j} a_i < \zeta \leq \sum_{i \leq j} a_i$.
   - Remove or close bond j.
4. Check for percolation, if true: equilibration and return to 2.
5. Exit program.

2.5.2 Linear Displacement

As an extension of the constant displacement we also study node displacement which linearly increases in time. Because this approach shares several similarities with the RFM, we discuss the RFM simulation protocol first. For the RFM equilibrium is achieved by solving the Kirchhoff equations for each node, i.e. the set of linear equations

$$A\vec{x} = \vec{b}. \tag{2.15}$$

Here the stiffness matrix A contains all the conductivities of the network bonds (the fuses) and $\vec{b}$ is the vector of the nodal currents. A typical RFM simulation is given by the following protocol:

1. Increase global load. Equilibration.
2. Check for links with current I_i larger than threshold T_i, if none return to 1.
3. Remove link with largest I_i/T_i.
4. Check for network percolation, if true: equilibration, return to 2.
5. Exit program.

Obviously, the bottleneck of a simulation according to this protocol is the equilibration step which for large systems causes enormous computational costs. There are very fast algorithms developed to face especially this problem [100, 101].

In our simulations, we also step-wise pull the network apart a unit displacement $dx = 1$. After this we equilibrate. We assume that displacement and equilibration happen instantaneously. We assume, that after the displacement, bond forces do not change for a time dt. That way, we model a bond network displaced with speed $v = dx/dt$. Please note, dx is not identical to the above mentioned δx. However, their relation is given by $\delta x = m \cdot dx$, where m denotes the number of steps taken up to the time under consideration. The force F_{ij} which acts in the bond connecting nodes i and j is assumed to be constant during the time dt. That is, the probability that the bond stays closed over time, $q_{ij}(t)$, follows from Eq. (2.10) in dimensionless form and is given by

$$\dot{q}_{ij} = -e^{F_{ij}} q_{ij}. \tag{2.16}$$

The solution of Eq. (2.16) is $q_{ij} = \exp(-\exp(F_{ij})t)$. Hence the probability of rupture of bond ij simply is

$$p_{ij,\text{rupture}} = 1 - q_{ij} = 1 - e^{-e^{F_{ij}} \cdot t}. \tag{2.17}$$

Analogous, the probability of a broken bond to close again (rebinding) is given by

$$p_{ij,\text{rebind}} = 1 - e^{-\gamma t}. \tag{2.18}$$

Motivated by the RSM we apply the following procedure:

1. Unit displacement, which takes a time dt. Equilibration
2. For each closed bond:
   - draw a random number $\xi \in [0, 1]$,
   - if $\xi < 1 - e^{-e^F dt}$ (F: force in the bond), remove bond.
3. If $\gamma > 0$: Equilibration.
4. For each broken bond:
   - draw a random number $\xi \in [0, 1]$,
   - if $\xi < 1 - e^{-\gamma dt}$ (additional temporary and spatial constraints) close bond.
5. Check for percolation, if true return to 1.
6. Exit Program.

2.6 Numerical Algorithms

2.6.1 Mechanical Equilibrium with Conjugated Gradients

For almost every numerical result presented in this thesis, it is necessary to calculate the mechanical equilibrium of bond networks. This has to be done once for cell shape analysis and several times for rupture studies. Therefore, we need a fast and stable equilibration algorithm.

Let us assume a network of N nodes, which are labeled with indices $1, .., N$. In order to keep the notation proper, we make use of an adjacency matrix $g = (g_{ij}) \in \mathbb{R}^{N\times N}$, which is 1 if nodes i and j are connected and 0 otherwise. Since g is sparse, in real computer simulations it is replaced by a link list. However, since g allows a closed and clear presentation, we use it here.

For nodes within the network the total force exerted on a node i is the sum of all forces applied on the node via bonds to connecting nodes. With g we can write

$$\vec{F}_i = \sum_{j=1}^{N} g_{ij}\vec{F}_{ij}. \tag{2.19}$$

In mechanical equilibrium the force on each non-adherent (non-clamped) node has to vanish: $\vec{F}_i = 0$ for all non-adherent (non-clamped) nodes i. The existence of adhesion / clamped sites is modeled by fixing the positions of the respective nodes. Thus the adhesion site geometry / displacement protocol will enter through the boundary conditions. In the following we will use dimensionless quantities.

Mechanical equilibrium requires the forces on each non-adherent (non-clamped) node to vanish

$$\sum_{j=1}^{N} g_{ij}\vec{f}_{ij} = 0 \qquad \forall \text{ non-adherent / non-clamped nodes } i. \tag{2.20}$$

For a two-dimensional network of N nodes the system of equations (2.20) consists of $2N$ coupled non-linear equations.

If the left hand side of system (2.20) consisted of arbitrary functions of the $\vec{r}_i$, the method of choice to solve it would be the Newton-Raphson method [102]. However, since the left hand side of system (2.20) is a force which has a potential, it is also a $2N$-dimensional gradient vector. Therefore we solve the minimization problem for the potential with the *conjugated gradient method* (CGM) [103]. Without loss of generality we use the example of a HSN for demonstration purpose. So we can avoid piece-wise defined functions in this section.

Given the potential of the whole network:

$$W\colon \mathbb{R}^{2N} \to \mathbb{R}, \vec{r} \to W(\vec{r}) = \frac{1}{2}\sum_{i=1}^{N}\sum_{j=1}^{N} u_{ij}^2 g_{ij}, \tag{2.21}$$

Here, $\vec{r} = (\vec{r}_1^T, \vec{r}_2^T, ..., \vec{r}_N^T)^T$ contains all the node positions in one vector. The potential W depends on u_{ij} which is a function of $\ell_{ij} = |\vec{r}_i - \vec{r}_j|$. That is, via u_{ij} the potential depends on $\vec{r}$. We can now calculate the gradient of W with respect to $\vec{r}$, $\vec{f} = -\vec{\nabla}_{\vec{r}} W(\vec{r})$:

$$\vec{f}\colon \mathbb{R}^{2N} \to \mathbb{R}^{2N}, \vec{r} \to \vec{f}(\vec{r}). \tag{2.22}$$

Here $\vec{f} = (\vec{f}_1^T, \vec{f}_2^T, ..., \vec{f}_N^T)^T$ contains all the node forces in one vector. The force acting on node i then reads

$$\begin{aligned} \vec{f}_i &= \left(-\left(\nabla_{\vec{r}} W(\vec{r})\right)_{2i-1}, -\left(\nabla_{\vec{r}} W(\vec{r})\right)_{2i}\right) \\ &= -\sum_{j=1}^{N} u_{ij} \frac{\vec{\ell}_{ij}}{\ell_{ij}} g_{ij}. \end{aligned} \tag{2.23}$$

The CGM starts with an arbitrary position $\vec{r}_0$ out of equilibrium, e.g. all free nodes at their positions from the tension-free reference state. The corresponding force is denoted $\vec{h}_0$. The position is updated by calculating the line minimum along the direction $\vec{h}_l$ which itself updates according to

$$\vec{h}_{l+1} = \vec{f}(\vec{r}_{l+1}) + \frac{\vec{f}(\vec{r}_{l+1}) \cdot \vec{f}(\vec{r}_{l+1})}{\vec{f}(\vec{r}_l) \cdot \vec{f}(\vec{r}_l)} \vec{h}_l. \tag{2.24}$$

The directions given by Eq. (2.24) satisfy $\vec{h}_l \cdot \vec{h}_m = 0$ for $l \neq m$ [104]. This makes the CGM superior to the steepest descend method (SDM), e.g. used in [15]. In the SDM the moving directions are the gradients of the potential W themselves, i.e. $\vec{h}_l = \vec{f}(\vec{r}_l)$, which does not necessarily satisfy $\vec{h}_l \cdot \vec{h}_m = 0$ for $l \neq m$. We stop iterating as soon as the force on every node (except the periphery nodes) is smaller by at least two orders of magnitude than the smallest bond force.

2.6.2 Image Segmentation with Otsu's Method and GrowCut

Since in chapter 4 we simulate real adherent tissue cells, we have to segment the cell body from the black and white actin-stained images. For these image segmentation purposes we use the commercial software MatLab. MatLab handles an image as a rectangular pixel matrix M. The matrix entries M_{ij} give the signal intensity at pixel (i, j). MatLab's image processing toolbox provides an implementation of Otsu's method [105], which calculates an intensity threshold for black and white images. We set matrix entries with an intensity higher than the threshold to 1 (inside the cell) and those with lower intensity to 0 (outside of the cell). We find that this result is not sufficient, because cell boundaries become very angular. However, this matrix can be taken as starting point into the algorithm *GrowCut* [106]. For this purpose, we only use 60% of the matrix entries. The rest is randomly deleted and treated as unknown.

GrowCut can be easily understood figuratively as spreading bacteria. The seed pixels outside and inside the cell correspond to bacteria of species A and B, respectively. Now these bacteria spread on the image. Bacteria of different species fight against each

other to increase their occupied area. The winner of one fight, which overtakes the losers pixel, depends on strength and distance of the two competitors. That way, in the end, the image is segmented by a front line, i.e. the cell boundary. To enhance smoothness of the front line, one can introduce further rules. For example a bacterium which is surrounded by too many enemies will die and its pixel will be taken by the enemies. As we show later, this procedure gives very nice segmented cells.

2.6.3 Triangulation with DistMesh

In order to endow the segmented cells with an actin CSK we generated a network inside them using the mesh-generator *DistMesh* [107]. The authors provide a MatLab implementation of DistMesh, which is directly used by us. It is well known that the triangular network is the best choice to fill arbitrary geometries with a mesh. Hence we will not use square or hexagonal network topologies in chapter 4.

DistMesh makes use of a signed distance function $d_{DM}(x, y)$, which in our case can be obtained via MatLab's *bwdist* function. bwdist calculates the euclidean norm (in units of pixels) from the closest pixel with entry 1. Clever combination of bwdist applications to the cell image obtained with GrowCut gives $d_{DM}(x, y)$ as the distance to the cell boundary. Signed means that $d_{DM}(x, y)$ is negative inside the cell and positive outside. DistMesh starts with regularly distributed nodes in the desired cell. These nodes are linked via a Delaunay triangulation, which can be seen as complementary to the Voronoi construction introduced above [108]. This network is assumed to experience external forces from the boundary, which it must not cross, and from the internal links, which are assumed as springs of a given (not necessarily) uniform length. In equilibrium, the links have uniform length. It is possible to define fixed points, which are not varied by DistMesh. This is very helpful in regard of stress fiber introduction.

2.6.4 Traction Force Reconstruction with FTTC

Note, the term 'traction force reconstruction' might be misleading. Here, it is not the traction force which is reconstructed, but traction force per area, i.e. traction stress $\vec{\sigma}_N$.

As mentioned in the introduction, the measured quantity of TFM is the marker displacement, i.e. substrate strain $\vec{u}_S$. There are several methods to calculate the traction stress field $\vec{\sigma}_N$ from $\vec{u}_S$ [17, 28–30]. In this thesis we use the Fourier-transform traction cytometry (FTTC) algorithm, which is implemented in MatLab code as part of the program *TF_reconstruction* by Benedikt Sabass [17].

The two-dimensional strain $\vec{u}_S$ of the substrate surface is caused by the traction stress $\vec{\sigma}_N$ applied by the adherent cell. According to [17, 29, 109] their relation is given by the convolution integral

$$u_{S,i}(\vec{x}) = \int \sum_j G_{ij}(\vec{x} - \vec{x}')\sigma_{N,i}(\vec{x}')d\vec{x}', \tag{2.25}$$

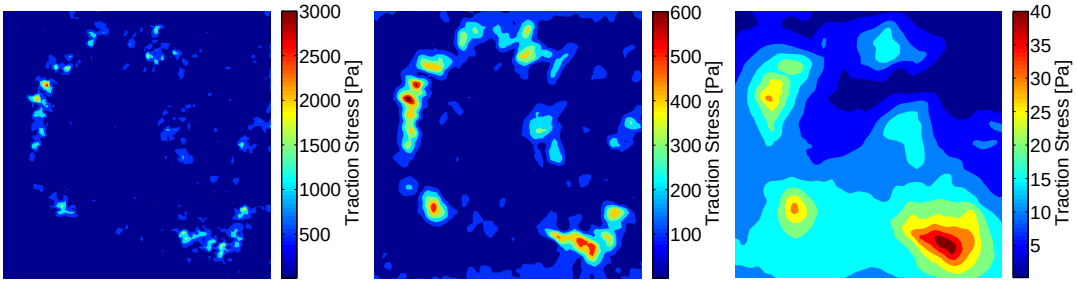

Figure 2.5: Reconstruction of traction stress. Magnitude of the reconstructed traction stress field for the cell shown in Fig. 1.5(a). Three different regularization parameters have been used for reconstruction with FTTC. From left to right: $\lambda_r = 2.4 \times 10^{-7}$, $\lambda_r = 2.4 \times 10^{-5}$ (optimal), and $\lambda_r = 2.4 \times 10^{-3}$. Data courtesy of J. Stricker and M. L. Gardel.

with the Green function [17]

$$G_{ij}(\vec{x}) = \frac{1+\nu_S}{\pi E_S}\left((1-\nu_S)\frac{\delta_{ij}}{|\vec{x}|} + \nu_S \frac{x_i x_j}{|\vec{x}|^3}\right). \tag{2.26}$$

Here, δ_{ij} denotes the Kronecker symbol: $\delta_{ij} = 1$ if $i = j$ and $\delta_{ij} = 0$ otherwise. E_S and ν_S are the substrate's Young modulus and Poisson ratio, respectively. Eq. (2.25) has to be inverted to obtain $\vec{\sigma}_N$. It is convenient to use a Fourier transformation, because in Fourier space the convolution integral becomes a simple product. After spacial discretization and Fourier transformation Eq. (2.25) can be written as [17]

$$\tilde{u}_{S,i,k} = \left\{\sum_j \tilde{G}_{ij}\tilde{\sigma}_{N,j}\right\}_k, \text{ inversion gives: } \tilde{\sigma}_{S,i,k} = \left\{\sum_j \tilde{G}^{-1}_{ij}\tilde{u}_{S,j}\right\}_k. \tag{2.27}$$

The Green function transforms to [17]

$$\tilde{G}_{ij,k} = \frac{2(1+\nu_S)}{E_S}\left(\frac{\delta_{ij}}{k} - \frac{\nu_S k_i k_j}{k^3}\right). \tag{2.28}$$

Because there is very much noise in biological cells, the application of a regularization scheme is required. Thereby, the traction stress field is smoothed. For the detailed calculus please see [17]. The regularized form of Eq. (2.27) is

$$\tilde{\sigma}_{N,ik} = \left\{\sum_{l,j}\left[\sum_m \tilde{G}_{ml}\tilde{G}_{mi} + \lambda_r^2 \tilde{H}_{il}\right]^{-1}\tilde{G}_{ji}\right\}_k. \tag{2.29}$$

For zeroth order regularization H_{ij} is chosen to be the identity matrix. If the regularization parameter λ_r is increased, the stress field becomes smoother but information on smaller length scales is lost. On the other hand does a regularization parameter, which is too small, lead to very noisy traction stresses, see Fig. 2.5 for an example. Therefore, an optimal choice of λ_r is needed. For FTTC the optimal λ_r is calculated by an L-criterion [17].

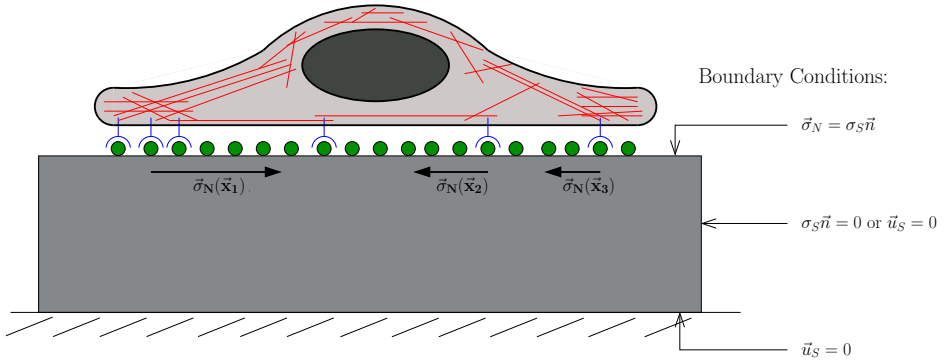

Figure 2.6: Reconstruction of substrate strain. A tissue cell (light gray) adheres to the surface of a substrate (dark gray). Strongly simplified, the actin cytoskeleton (red) connects to the fibronectin coating (green) via integrins (blue). Thereby, traction stress $\vec{\sigma}_N$ is transmitted to the substrate, which leads to substrate strain $\vec{u}_S$. The given boundary conditions are sufficient to calculate $\vec{u}_S$.

2.6.5 Reconstruction of Displacement Fields with celldeform

Numerical calculation of the equilibrium states of the triangular networks obtained via GrowCut and DistMesh is noise-free. This results in localized traction forces at the fixed network nodes. This makes it very difficult to compare the smoothed experimentally obtained traction stress with the simulation result. We therefore put the cart before the horse: we start with perfect traction stress $\vec{\sigma}_N$ and calculate the displacement field of the substrate $\vec{u}_S$. Then we make use of FTTC like after a TFM experiment, in order to calculate the reconstructed traction stress $\vec{\sigma}'_N$.

The stress tensor $\sigma_{S,ij}$, $i,j \in \{x,y,z\}$, contains the stresses on a unit cube oriented with its surfaces orthogonal to the axis of an euclidean coordinate system [109]. Hence, the unit vectors $\hat{e}_i$, $i = x,y,z$ of that coordinate system are (anti-) parallel to the surface normal vectors of the cube. $\sigma_{S,xy}$, for example, is the stress in y-direction applied to the cube surface with surface normal vector $\hat{e}_x$. The stress $\vec{\sigma}_N$ on any surface of the material, which has normal $\vec{n}$, is related to $\sigma_S = (\sigma_{S,ij})$ via [110]

$$\vec{\sigma}_N = \sigma_S \vec{n}. \tag{2.30}$$

The substrate strain tensor $u_{S,ij}$ in linear order is given by:

$$u_{S,ij} = \frac{1}{2}\left(\frac{\partial u_{S,i}}{\partial x_j} + \frac{\partial u_{S,j}}{\partial x_i}\right). \tag{2.31}$$

Strain and stress tensor obey the constitutive relation [110]

$$\sigma_{S,ij} = C_{S,ijkl} u_{S,kl}. \tag{2.32}$$

Note, in this section we use the Einstein sum convention. We assume the substrate to be homogeneous, isotropic, and linearly elastic. Then there are only two independent material's constants, namely the Lamé constants λ_S and μ_S:

$$C_{S,ijkl} = \lambda_S \delta_{ij}\delta_{kl} + 2\mu_S \delta_{ik}\delta_{jl}. \tag{2.33}$$

The Lamé constants are related to the substrate's Poisson ratio ν_S and Young modulus E_S:

$$\lambda_S = \frac{\nu_S E_S}{(1+\nu_S)(1-2\nu_S)},\ \mu_S = \frac{E_S}{2(1+\nu_S)}. \tag{2.34}$$

Inserting Eq. (2.33) into Eq. (2.32) we obtain

$$\sigma_{S,ij} = \lambda u_{S,kk}\delta_{ij} + 2\mu_S u_{S,ij}. \tag{2.35}$$

In equilibrium $\sum_j \partial_{x_j}\sigma_{S,ij}$ has to vanish. Together with Eq. (2.35) this gives the Navier equation [110]

$$(\lambda_S + \mu_S)\nabla\nabla\cdot\vec{u}_S + \mu_S\nabla^2\vec{u}_S = 0, \tag{2.36}$$

which has to be solved with the given stress field σ_N at the top surface and zero strain at the bottom of the substrate, see Fig. 2.6. The lateral surface can either be assumed as stress-free or clamped (i.e. with vanishing strain). In the limit of a large substrate both assumptions give similar results.

The boundary value problem for $\vec{u}_S$ is solved with the FEM algorithm *celldeform*, which is implemented in C++. celldeform needs the traction stress field on the substrate surface as input. It must be on a regular grid. Therefore we interpolate the traction force field first and then divide it by pixel area. celldeform was kindly provided by Jérôme Soiné.

The polyacrylamide substrate, which was used in the experiments, has $\nu_S = 0.5$, i.e. is incompressible. The Young modulus E_S varies from 2.8 to 90 kPa.

2.6.6 Percolation Check with a Tree-based Algorithm

To check for percolation of a network we use the fast tree-based algorithm developed by Newman and Ziff [111, 112]. In this algorithm we investigate the network clusters. A network cluster is a set of nodes of that network which are connected. Since the separation of network nodes into clusters is well-defined, each of these clusters contains a dedicated node which is called root. If and only if two nodes i and j of the network have the same root, they belong to the same cluster and hence the network percolates from node i to node j.

The algorithm only needs a label i for each of the N nodes of the network, $i \in \{1, ..., N\}$, and the so-called pointer array p_i. For roots p_i is negative. For all other nodes p_i gives the label of another node from the cluster, according to a tree structure. For every node it must be possible to recursively find the root of its cluster following the pointers p_i.

Initially, every pointer is set to $p_i = -N - 1$, i.e. every node is its own root. We define the empty state by $p_i = -N-1$. Then for every node i it is checked if a (possible)

nearest neighbor j is connected to i and if $p_j \neq -N-1$. In that case the recursive root-finding routine is applied. If the roots differ, the pointer of the root i_1 with the lower pointer p_1 is increased by the pointer p_2 of the other root i_2. After that, the pointer p_2 is replaced by i_1. Hence, i_2 is no longer root, but now has root i_1. This is done for every node i.

The actual percolation check then simply reduces to taking the nodes of the two clamped sides and applying the root finding routine. If there are root nodes which appear on the one clamped side and on the other clamped side, the network did not fail yet, if not then it already did. A disadvantage of this algorithm is that it is only applicable to regular topologies. Thus, it cannot be applied to Voronoi networks. For Voronoi networks we find the clusters by checking the nodes one by one. This method is very time consumptive.

2.7 Parameterization

Due to its dynamic and multiscale organization and the known limitations of microscopy, a detailed model of the actin cytoskeleton is currently out of bounds. In the face of these uncertainties, our models are not meant to represent the details of the organization of the actin cytoskeleton. Nevertheless, for practical purposes it is helpful to parameterize our model using some benchmark values for the actin cytoskeleton.

The elastic modulus of an actin filament, which has cross-section area $A_{fil} = 18.8$ nm^2, was experimentally found to be $E_{fil} = 2.8$ GPa [113], while typical values for stress fibers are $A_{fib} = 31416$ nm^2 and $E_{fib} = 1.45$ MPa [114]. Hence, the Young modulus of stress fibers is three orders of magnitude smaller than the one of single actin filaments. This suggests that cross-linkers like α-actinin and myosin II are the main contributors to elasticity and not the actin filaments themselves. However, the values for the one-dimensional modulus, $E_{fil}A_{fil} = 52.64$ nN and $E_{fib}A_{fib} = 45.6$ nN, are effectively very similar, so the one-dimensional modulus is expected to be of the order of 50 nN.

The mesh size of the cytoskeleton is expected to be typically around $L_0 = 100$ nm. This is an intermediate value introduced in [80] based on experimental observations of the actin cytoskeleton in adherent endothelial [115] and fibroblast cells [116]. For the active force, we estimate that around 1.000 myosin II motors are active in one effective link. With a stall force of 2 pN per motor head [11], we have $T = 2 \cdot 10^{-2}$ nN/nm for the motor force per length. Using Eq. (2.7) and $EA = 50$ nN, we estimate $\tau = 0.04$ for the active tension in the network.

3

Contractile Network Models for Adherent Tissue Cells

Now, we study the different network models for adherent cell contraction, HSN, PCN, and ACN, in regard of cell shape and contour forces. To this end we mainly use the square network topology S1. We demonstrate how the cell contour invaginates and that it exhibits circularity only for ACNs. In order to increase the comprehension of this arc morphology we relate the ACN to two analytical theories. First the tension-elasticity model, which has already been used to study adherent cells. Second, an elastic catenary theory, which is actually used for a chain in the gravitational field. Several extensions of this approach are discussed also: strain stiffening, link adaptation, homogenization, and three dimensional networks.

3.1 Equilibrium Shapes

In Fig. 3.1, the results for HSN and PCN are the same for the square shape, Fig. 3.1(a,c), because these two kinds of networks behave identical as long as all links are tensed. However, the results are somehow different for the triangle shape, Fig. 3.1(b,d). In this case, the PCN gives a significantly flatter contour due to the missing response to compression in the thin arms leading to the adhesion points. The most prominent examples for compressed links in Fig. 3.1(b,d) are indicated by arrows.

In order to understand our numerical results in more detail, we first note that the HSN with triangular network topology has a well-defined continuum limit, in which it corresponds to a two-dimensional sheet with isotropic linear elasticity [64, 65]. The two corresponding elastic constants are a Young modulus of $2k/\sqrt{3}$ and a Poisson ratio of $1/3$, where $k = EA/L_0$ is the spring constant of the links. The HSN with simple cubic topology does not have such a rigorous limit, but in our context it works in a similar way as the triangular lattice. Therefore similar results as obtained here for the HSN are also obtained with continuum elasticity theory applied to two-dimensional cell shapes [79]. Without any adhesion constraint, the HSN contracts isotropically to a finite size, i.e. the network is uniformly scaled and has a new side length $d' = 10\ell_0$.

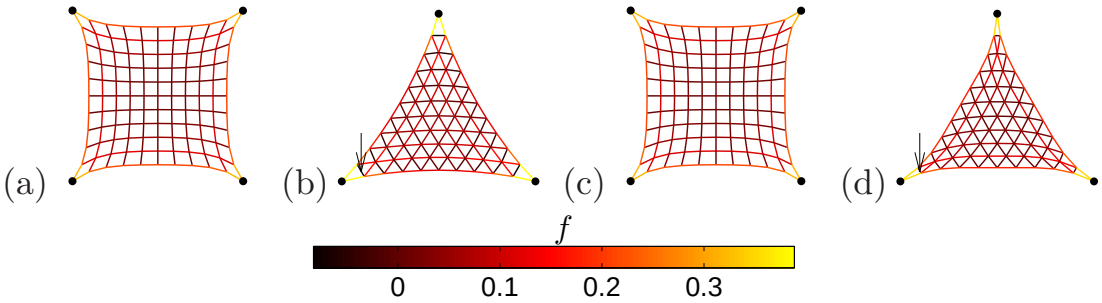

Figure 3.1: Tensed Hookean (HSN) and passive cable networks (PCN) with $\tau_H = 0.2$. The colorbar gives the dimensionless force f. (a) Contraction of a HSN in the square reference state. (b) Equilibrium shape of a HSN in triangular reference state. (c) PCN in square geometry. (d) PCN in triangular geometry. Note the difference between (b) and (d).

This shape we call the unconstrained reference shape and it is key to understand the results for HSN. The same shape as shown in Fig. 3.1(a) results if the network contracts away from its initial state under adhesion constraints or if the network starts from its unconstrained reference state and its corners are dragged to the desired adhesion points. This explains the main feature of the force distribution shown by the color coding in Fig. 3.1(a), namely the strong localization of stresses and strains to the regions around the adhesion points. With the amount of tension used here, the network can attain its unconstrained reference state away from the adhesion points and therefore its contour is essentially flat in the middle parts.

In Fig. 3.3(a) we directly compare the calculated network shapes for the square geometry to the unconstrained reference shape. In addition, we demonstrate the role of the link length ℓ. For the small value of tension, $\tau_H = 0.2$, the contracting network can reach the unconstrained reference shape over a large region where it is essentially flat. The smaller ℓ, the faster this contour is reached due to an increased force density along the contour. For the large value of tension, $\tau_H = 0.6$, the unconstrained reference shape is not reached by the contracted network and it stays non-flat along its whole contour even for rather small values of ℓ.

Figs. 3.2(a)-(d) show the equilibrium shapes of an active cable network (ACN) with reference state from Fig. 2.2(a) and increasing tension τ. As tension increases, the shape becomes more and more invaginated, until it collapses onto the zero-area network in Fig. 3.2(d). This network basically consists of a centrally contracted region which is connected to the adhesion points by long arms. We therefore call this network the center tree (CT). Note that this network still retains aspects of the two-dimensional network, because an effectively one-dimensional structure would collapse onto the so-called Steiner tree [117] of minimal length, which for a square is not four-fold symmetric.

In contrast to the passive networks, where tension ceases as the unconstrained reference state is reached, for the ACN no such unconstrained reference shape exists and without adhesion constraints the shape would collapse onto a single point. This

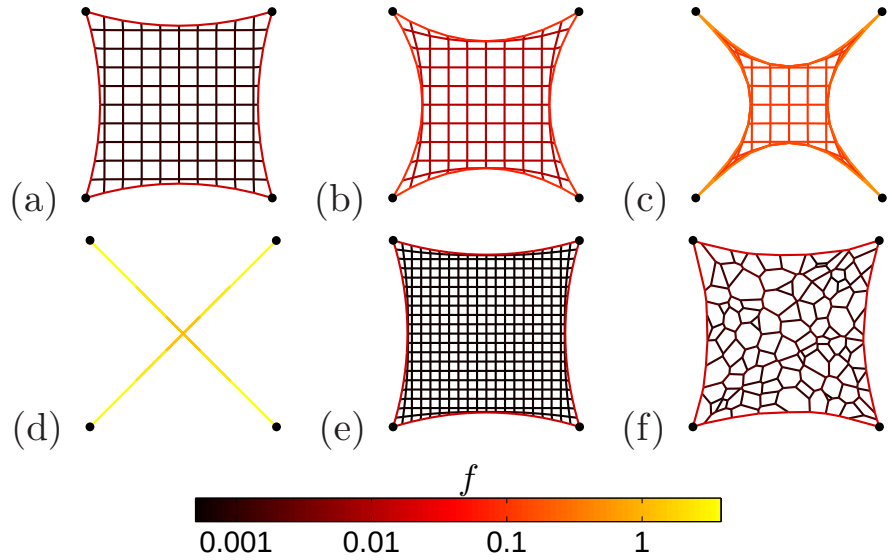

Figure 3.2: Contraction of an ACN with square shape. (a) and (b) Contraction of the network leads to arc formation. (c) With increasing tension tubes form near the adhesion points. Note the bundling of filaments at the edge. (d) For $\tau \to \infty$ the network collapses onto the center tree. (e) The same situation as in (a) but with $\ell = 0.5$. The contour is equal to that in (a), even forces are the same. (f) Square Voronoi network with 212 nodes and 316 links. Note the strong stress localization in the periphery. Tension values are (from (a) to (f)): $\tau = 10^{-3},\ 10^{-2},\ 10^{-1},\ 1,\ 10^{-3},\ 10^{-3}$.

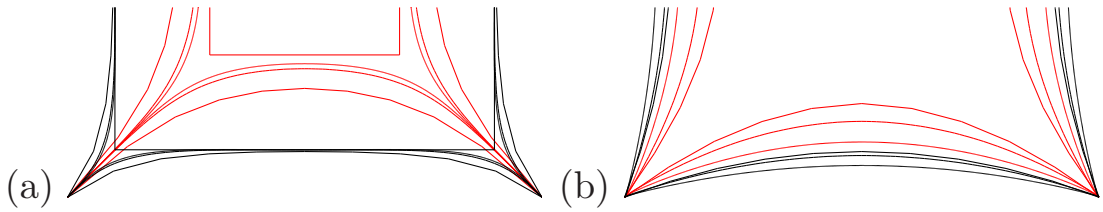

Figure 3.3: Boundary line of the different models in square geometry. (a) ACN with $\tau = 10^{-3}$ (lower set) and $\tau = 10^{-2}$ (upper set). The three lines represent the initial link lengths $\ell = 1,\ 0.1,\ 0.02$ (from top to bottom). (b) HSN/PCN with network tension $\tau_H = 0.2$ (lower set) and $\tau_H = 0.6$ (upper set). The straight line shows the unconstrained reference shape, while the three curved lines represent different initial link lengths, namely $\ell = 1,\ 0.1,\ 0.02$ (from bottom to top within one set).

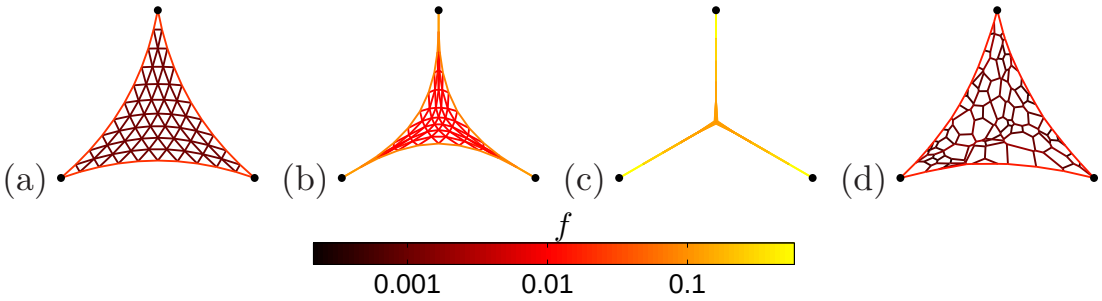

Figure 3.4: Contraction of an ACN with triangle shape. (a)-(c) Contracted equilibrium shapes for the triangular reference state. (d) Triangular Voronoi network with 175 nodes and 261 links. Tension values are (from (a) to (d)): $\tau = 10^{-3},\ 10^{-2},\ 10^{-1},\ 10^{-3}$.

explains why no flat parts are observed in the contours of the networks shown in Fig. 3.2. This figure also shows that the formation of inward directed arcs now corresponds to a much more inhomogeneous density distribution of filaments: in the bulk of the network the distance between nodes and thus the filament density remains unchanged, while at the edges filaments start to bundle strongly along the edge. The color code in Fig. 3.2 shows that stress is strongly localized at the periphery. In the interior, the only forces acting are the motor forces τ which balance each other at every node. At the periphery, the force jumps up from τ to much higher values $\tau + EA\Delta\ell_j/\ell$, compare Fig. 3.2(a). The forces are largest close to the adhesion points and decrease towards the center of the boundary. For large tension ($\tau > 10^{-2}$), tubes are formed near the adhesion points and the stress distribution along the contour becomes more inhomogeneous.

Fig. 3.2(e) shows the effect of changed discretization for the same tension value as Fig. 3.2(a). Fig. 3.2(f) demonstrates that for ACN, shape and force values do not depend significantly on network topology. As an instructive example here we use a disordered network topology obtained by a Voronoi construction. Even the presence of relatively large elements in the discretization does not change the invaginated shape feature of the contracted network. We conclude from Fig. 3.2(e) and Fig. 3.2(f) that ACN are surprisingly robust in regard to the details of the network topology. Fig. 3.3(b) gives a more detailed picture for the contour and proves that the lattice constant ℓ has an effect, as it increases the force density along the contour as for the passive networks. However, the effect seems to be considerably weaker than for the passive networks, compare Fig. 3.3(a).

Similar results as obtained in Fig. 3.2 for the square shape are also obtained for other initial cell shapes. We checked this in particular for the triangular shape from Fig. 2.2(b), for which we again observe growing invagination and inhomogeneous boundary stress if we increase τ, see Fig. 3.4(a)-(c). For further increasing τ again tubes are formed and the triangular network collapses onto the CT Fig. 3.4(c). In all cases, stress is strongly localized to the periphery. In addition, by analyzing a Voronoi construction in a triangular shape, we have checked that variation in both cell shape and network topology do not change our basic results for ACNs, Fig. 3.4(d).

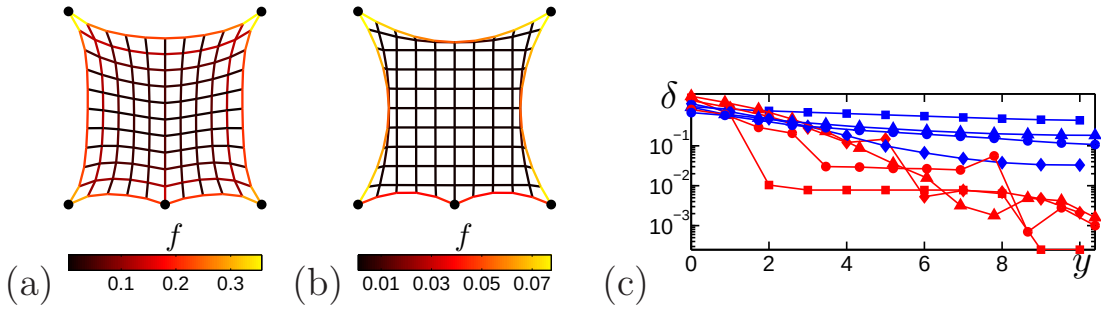

Figure 3.5: Contraction of networks with square shape with an additional adhesion point in the middle of the bottom line. (a) HSN model with $\tau_H = 0.2$. (b) ACN with $\tau = 10^{-2}$. (c) Relative displacement δ of nodes with $x = 5$ (vertical middle line) with and without the additional adhesion point at the bottom. y is the node's y-coordinate in the initial network. The four top lines correspond to the HSN while the four bottom lines represent the ACN. Different symbols show different topologies (square=□, diamond=◇, triangular=△, hexagonal=◯.)

Fig. 3.5 reveals another interesting property of ACN, namely its robustness in regard to addition of new adhesion points. In Fig. 3.5(a,b) we show the equilibrium shapes of the HSN from Fig. 3.1(a) and the ACN from Fig. 3.2(b) with one adhesion point added in the middle of the bottom line. This change in adhesion geometry leads to a strong change in the global structure of the HSN, but much less so for the ACN. In case of the ACN model this change at the bottom of the network has little influence on the positions of nodes not directly connected to the bottom line. In contrast, for the HSN the additional adhesion point affects the shape of the opposite arc, becoming more curved in the center. In Fig. 3.5(c) we plot by which distance δ the nodes in the vertical middle line are pulled down in the negative y-direction upon addition of the new adhesion point. The plot of $\log \delta$ versus y is not smooth for numerical reasons, but clearly shows that the effect decays much more rapidly for the ACN versus the HSN. In addition to square and triangular network topologies, here we also show results for rotated square (diamond) and hexagonal networks. Intriguingly, stress in the contour behaves very differently, compare the color coding of Fig. 3.5(a,b). While in the HSN stress in the bottom line stays approximately the same, in the ACN it decreases to half its value, indicating a strong effect on contour forces.

In summary, ACNs behave very differently from HSNs (and therefore also from the mostly equivalent PCNs). Vaguely speaking, they act more locally than globally. They are more robust in regard to network topology and adhesion geometry and show strong localization of the stress to the periphery. Shape and contour stress seems to be mainly determined by the local adhesion geometry and therefore will be analyzed in more detail below.

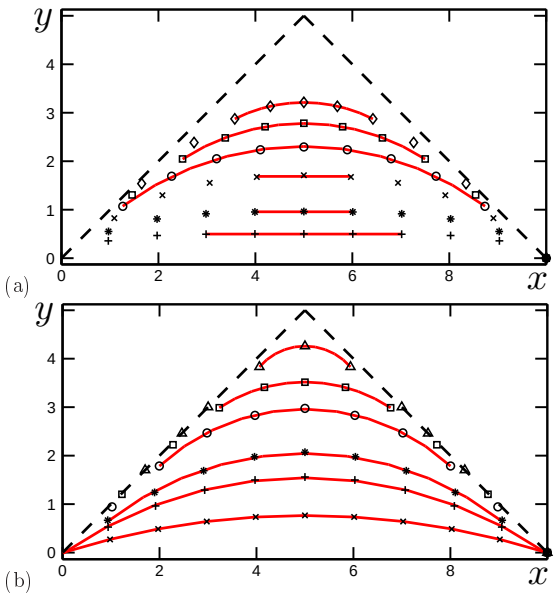

Figure 3.6: Arc fits for HSN and ACN. (a) Arc analysis for a tensed HSN. From bottom to top: $\tau_H = 0.1$ (+), 0.2 ($*$), 0.4 ($\times$), 0.6 ($\bigcirc$), 0.8 ($\square$), 1 ($\Diamond$). Symbols: Contour. Lines: Straight fits of the linear contour parts (the three bottom lines), least square fits of round contour parts to arcs with constant curvature (the three top lines). $*$ corresponds to the bottom line from the networks shown in Figs. 3.1a and c. (b) Contour analysis for the bottom line of an ACN with $\tau = 10^{-3}$ ($\times$), 10^{-2} (+), 2.5×10^{-2} ($*$), 10^{-1} ($\bigcirc$), 2.5×10^{-1} ($\square$), 5×10^{-1} ($\triangle$) from bottom to top. Symbols denote node positions of the network arcs while the lines are least square fits of the contours to arcs of constant curvature. $\times$, +, $\bigcirc$, and dashed line correspond to the bottom lines from Figs. 3.2a-d.

3.2 Contour Shape and Tension-Elasticity Model

In contrast to HSNs, the contour of ACNs appears to be more circular. Indeed, a circular arc morphology has been noted before for the shapes of cells adhering to micropatterned substrates and therefore this shape feature is an important motivation to study ACNs [15]. We now investigate this important aspect in more detail. In Fig. 3.6(a) and (b) we show contours of the HSN and ACN from Fig. 3.1 and Fig. 3.2, respectively. In addition, we vary the tension in the edges (τ_H and τ, respectively) and therefore observe more invaginated contours for increased tension.

For the HSN, small tension allows the network to reach the unconstrained reference shape and therefore the best fit to the middle part of the contour is a straight line. For larger tension, the unconstrained reference shape cannot be reached anymore and circular shapes become better fits. This crossover is in marked contrast to the ACN from Fig. 3.6(b), where circular arcs fit very well for all values of τ. For large τ, the overall contour starts to deviate from the perfect arc shape because the networks starts to collapse into tubes near the adhesion points. However, locally (in between the tubes) the contour stays circular. Another difference between the two network types lies in the observation that for HSNs, network shape strongly depends on lattice constant ℓ, while for ACNs, the equilibrium contour is relatively independent of ℓ.

It has been argued before that the circular arc shape feature of the ACNs can be explained by an analytical theory, the tension-elasticity model (TEM) [15]. For clarity, here we repeat this analysis and compare it in detail with our network simulations. Because ACNs do not propagate compression and the motor forces represent a constant pull in the network, in the TEM the bulk contractility is modeled by a structure-less surface tension σ. However, elasticity is crucial to understand how the contour reacts to

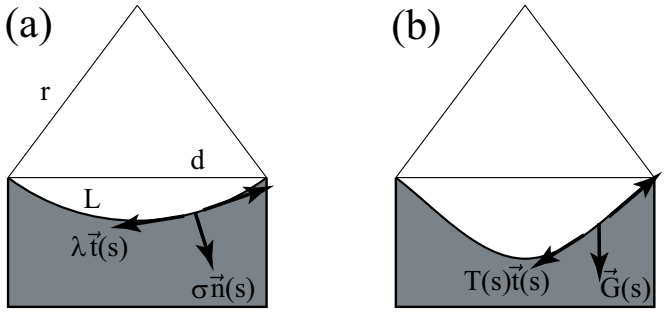

Figure 3.7: Schematic representation of the two contour models. (a) In the tension-elasticity model (TEM), an isotropic surface tension σ pulls the contour in along the normal direction, while the counteracting line tension λ acts along the tangential direction. r is arc radius, L is contour length, and d is spanning distance. (b) In the elastic catenary model, the inward pull is vertical and thus leads to an inhomogeneous line density of force along the elastic contour.

the internal pull. Therefore the elastic nature of the mechanical network is represented by an elastic line tension λ, which prevents the contour from collapsing under the inward pull of the bulk network. This line tension is written as

$$\lambda = EA\frac{L - L_0}{L_0} \tag{3.1}$$

where L is the contour length and L_0 is its resting length. Note that we use the same value EA like for the single links because the elastic line tension will be dominated by the contribution from the most peripheral line of links. We further assume $L_0 = \alpha d$, where d is the initial (*spanning*) distance d between two neighboring adhesion points (which in the simulations above has been chosen to be 10) and α is a dimensionless resting length parameter (compare Fig. 3.7 for a schematics). In the following we restrict ourselves to $\alpha = 1$, that is we assume that a completely relaxed contour is straight, but without internal tension. This implies that we neglect the contribution of the active contractility in the periphery to the line tension.

The relation between surface tension σ and network tension τ, which depends on network topology and discretization, can be obtained numerically. For this purpose, we simulate the pulling of a rectangular sheet of network. Surface tension σ then follows as total force on the pulling boundary divided by its width. Due to this normalization, the result does not depend much on link length ℓ, thus we use $\ell = 1$ for the simulations. For all considered network geometries, we find a linear relation:

$$\sigma_{square} = 0.9907\ \tau_{square}, \tag{3.2}$$
$$\sigma_{triangular} = 1.6892\ \tau_{triangular}, \tag{3.3}$$
$$\sigma_{diamond} = 1.0867\ \tau_{diamond}, \tag{3.4}$$
$$\sigma_{hexagonal} = 0.5517\ \tau_{hexagonal}. \tag{3.5}$$

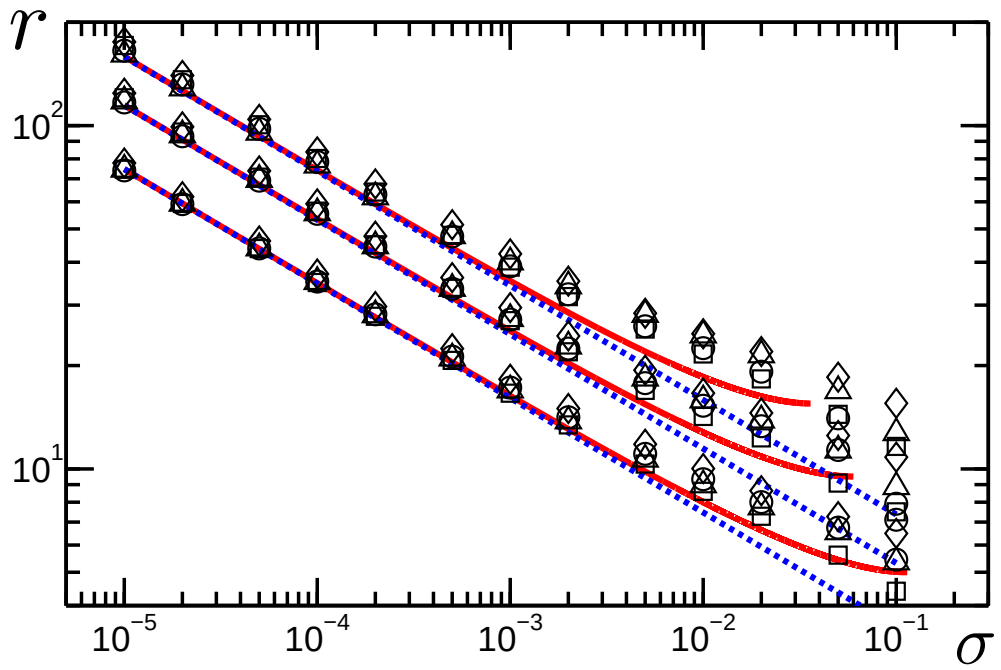

Figure 3.8: Relation of arc radii to internal tension of ACN for different dot distances and comparison to the tension-elasticity model (TEM). Symbols denote simulation results (□ corresponds to square, ◊ to diamond, △ to triangular, and ◯ to hexagonal topology), the solid line is the numerical solution of Eq. (3.9) and the dashed line the analytical result Eq. (3.10). Side lengths are (from bottom to top): $d = 10$, 19, 31, with critical tensions $\sigma_c \approx 0.114$, 0.060, 0.036.

The constant for the square lattice is close to 1 because here all links pull essentially perpendicular to the boundary.

Given the forces assumed by the TEM, one can derive the shape of the contour from the force balance. While the surface tension σ acts in the direction of the normal $\vec{n}$, the line tension λ acts in the tangential direction $\vec{t}$ (compare Fig. 3.7). Because the elastic line tension is a global quantity, it does not vary with the contour length s and therefore the contour tension is $\vec{T}(s) = \lambda\vec{t}(s)$. Then the force balance reads

$$\sigma\vec{n} = \frac{d\vec{T}}{ds} = \lambda\frac{d\vec{t}}{ds} = \frac{\lambda}{r}\vec{n} \tag{3.6}$$

where for the second part we have used the geometrical relation $d\vec{t}/ds = \vec{n}/r$ with r being the radius of curvature. We thus conclude that the TEM predicts circular arcs with a radius

$$r = \frac{\lambda}{\sigma} \ . \tag{3.7}$$

Although this results looks like a simple Laplace law in two dimensions, it is more complicated, because the arc radius r will depend on global properties like spanning distance d through the elastic line tension λ from Eq. (3.1).

In order to arrive at an expression for arc radius r as a function of adhesion geometry and network tension, we use the trigonometric relation

$$\sin\left(\frac{L}{2r}\right) = \frac{d}{2r} \tag{3.8}$$

to replace contour length L by spanning distance d, compare Fig. 3.7. In combination with Eq. (3.1) (in dimensionless form) and Eq. (3.7), this gives

$$r = \frac{1}{\sigma}\left(\frac{2r}{d}\arcsin\left(\frac{d}{2r}\right) - 1\right). \tag{3.9}$$

Since this equation cannot be solved analytically for r, it has to be solved numerically for given values of d and σ. For small values of σ, the invagination is small and one can expand the geometrical relation in $d/r \ll 1$. This leads to the analytical result

$$r = 24^{-\frac{1}{3}} d^{\frac{2}{3}} \sigma^{-\frac{1}{3}}. \tag{3.10}$$

In Fig. 3.8 we compare the results from computer simulations for r over a large range of network tension τ to the results of the TEM with the corresponding range of surface tension σ, both for the numerical solution of Eq. (3.9) and the analytical solution Eq. (3.10). We note that the predicted power law behavior applies over a very large range of tensions, and only breaks down at very large tension $\sigma > 10^{-2}$, see Fig. 3.8. Moreover the numerical analysis of Eq. (3.9) is limited, since for geometrical reasons r must always be greater than $d/2$. Therefore, a critical σ_c exists above which Eq. (3.9) cannot be solved anymore.

The inverse relation between r and σ in Fig. 3.8 represents a modified Laplace law for ACNs and thus demonstrates that the concept of an isotropic surface tension works well to explain cell shape. With the linear relation between σ and τ, this implies that $r \sim \tau^{-\frac{1}{3}}$. In Fig. 3.8 we also vary the dot distance and again find excellent agreement between computer simulations and TEM. Thus the elastic effects mediated by the spanning distance d are well captured by the concept of an elastic line tension.

In summary, the analytical TEM results in a surprisingly good description of the contour shape of ACNs. In particular, it nicely explains the appearance of circular arcs and the relation between arc radius r and spanning distance d. As we will discuss in the next section, however, agreement is less good regarding contour forces.

3.3 Contour Forces and Elastic Catenary Model

Fig. 3.9(a) shows how stress and strain vary throughout a cross-section parallel to the x-axis of a network with square topology. In the HSN stress decays into the sample, while for ACN, it jumps up at the periphery. Fig. 3.9(a) also shows that forces in

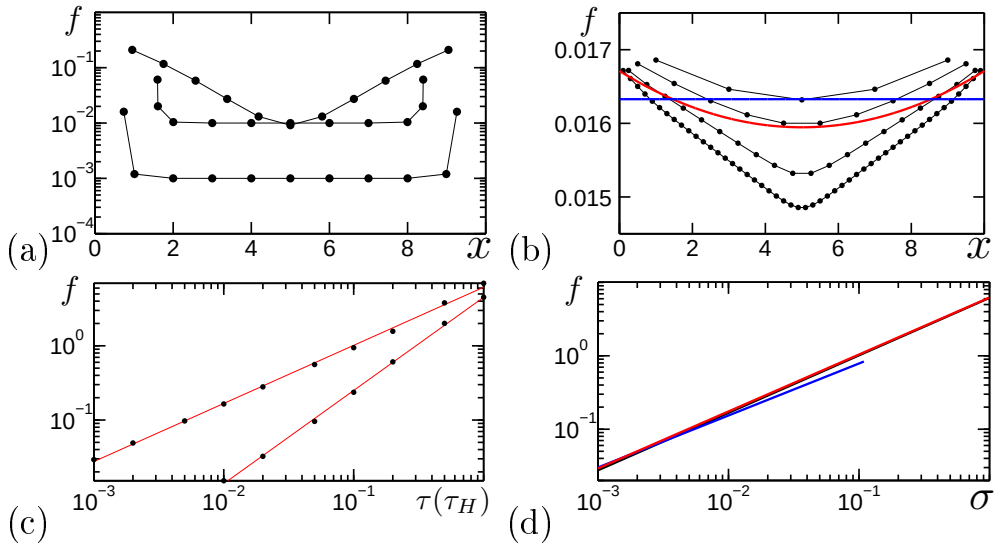

Figure 3.9: Force distribution in adherent networks. (a) Force of vertical links which cross the straight line $y = 5.5$ in the HSN from Fig. 3.1(a) (top) and the ACNs from Fig. 3.2(a,b) (bottom, center). (b) Force in the bottom line links of an ACN with $\sigma = 10^{-3}$ for different lattice constants (symbols). From top to bottom: $\ell = 2$, 1, 0.5, 0.2. The straight line gives the line tension obtained via the TEM, the curved line follows from Eq. (3.19). In both, (a) and (b), on the x-axis we have the x-coordinate of the center of mass of the links. (c) Forces on adhesion dots exerted by the ACN (top) and HSN (bottom). Simulation results are shown as dots, while lines give the power law fits. For the ACN we obtain $f = a\tau^b$ with $a \approx 6.16$ and $b \approx 0.783$ and for the HSN $f = a\tau_H^b$ with $a \approx 4.51$ and $b \approx 1.26$. (d) Power law fits of adhesion dot force vs. surface tension. ACN and elastic catenary results (top line, collapsed) and TEM (low line).

HSNs are much larger than those in ACNs with a comparable equilibrium shape. The stress distribution in the boundary of an ACN depends on the lattice constant ℓ of the network, as shown in Fig. 3.9(b). For both passive and active networks, the force which is exerted on an adhesion site follows a power law as τ_H (τ) is increased, see Fig. 3.9(c). For $\tau = \tau_H$ force is much smaller in the HSN than in the ACN. For active and passive networks of a comparable shape, however, e.g. $\tau_H = 0.2$ and $\tau = 10^{-2}$, we observe the opposite behavior.

Although on an absolute scale the variation is not very strong, Fig. 3.2(c) and Fig. 3.9(b) both demonstrate that for ACNs under large network tension, peripheral force varies along the contour. In contrast, the tension-elasticity model (TEM), which is very successful in explaining shape, predicts homogeneous force $\lambda = r\sigma$ along the boundary. Fig. 3.2 suggests one reason which could explain this discrepancy. For ACN, the links essentially telescope in under contraction and therefore their density along the contour varies for strong curvature along the contour. This suggests that in order to explain the spatially varying force in the contour, one has to revisit the assumption of an isotropic surface tension σ.

As an alternative to the TEM, we now investigate another analytical model which incorporates the effect of varying link density, namely the elastic catenary [118]. In the elastic catenary, the pulling force on the contour is not along the normal, but along the direction perpendicular to the original contour, similar to the situation in networks with square topology. Due to the linear elasticity in the contour, the line density of links along the contour varies. Since forces in the contour are an order of magnitude larger than motor forces, see Fig. 3.9(a), we assume the contour links as Hookean springs when pulled inward. Let σ be the inward force per unit length in the relaxed state. If the unit length element is under tension it has length $1 + T$. Therefore we have $\sigma/(1 + T)$ as force per unit length. We consider an initially horizontal contour which is pulled downward by a vertical force (as by gravity, compare Fig. 3.7). We call this inward force again surface tension σ, although now it does not act in the normal direction. Due to the elastic nature of the contour, the downward force varies along the contour as $\vec{G}(s) = (0, -\sigma/(1+T(s)))$, where $\vec{T}(s) = T(s)\vec{t}(s)$ is the contour tension acting in tangential direction. The force balance reads

$$\frac{d\vec{T}}{ds} + \vec{G} = 0 \ . \tag{3.11}$$

Because the tangent is normalized, it can be written as $\vec{t} = (\cos\phi, \sin\phi)$, where ϕ is the tangential angle [119]. Different from the TEM, we now have to solve two equations:

$$\frac{d}{ds}T(s)\cos(\phi(s)) = 0 \tag{3.12}$$

$$\frac{d}{ds}T(s)\sin(\phi(s)) = \frac{\sigma}{1+T(s)}, \tag{3.13}$$

Eq. (3.12) can directly be integrated, leading to $T\cos(\phi) = const = \lambda_c$, while Eq. (3.13) can be solved via the substitution $\tan(\phi) = \sinh(p)$. This gives

$$x(p) = \frac{\lambda_c}{\sigma}p + \frac{\lambda_c^2}{\sigma}\sinh(p) + x_0, \tag{3.14}$$

$$y(p) = \frac{\lambda_c}{\sigma}\cosh(p) + \frac{\lambda_c^2}{2\sigma}\cosh^2(p) + y_0, \tag{3.15}$$

with a parameter $p \in [-p_0, p_0]$ which cannot be eliminated from the equations. The integration constants x_0 and y_0 are determined by the positions of the adhesion sites. For an infinitely stiff boundary, this equation results in the catenary shape. For a vanishing resting length, it gives a parabola. Note that circular arcs result rigorously only for an isotropic surface tension acting along the normal, while here we assume a vertical force. While in the TEM we assume the line tension λ to be constant along the whole boundary line, for the elastic catenary only the x-component of tension, λ_c, is constant.

With the boundary conditions $x(p = 0) = x_0 = d/2 \Rightarrow x(p_0) = d$ we get an equations system for λ_c and p_0,

$$\sigma d = 2\lambda_c\left(p_0 + \lambda_c\sinh(p_0)\right), \tag{3.16}$$

$$2\sigma d(\lambda_c + 1) = \lambda_c\left(2\lambda_c p_0 + 4\sinh(p_0) + \lambda_c\sinh(2p_0)\right), \tag{3.17}$$

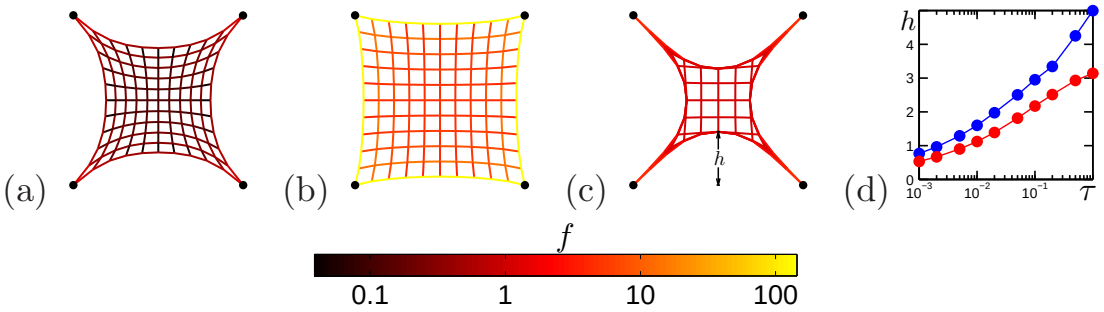

Figure 3.10: Contracted networks with worm-like chain (WLC) mechanics. (a) PCN with $\tau_H = 0.47$. (b) PCN with $\tau_H = 0.47$ and $\ell_n = 0.5$. (c) ACN with $\tau = 1$ and $\ell_n = 0.5$. (d) Maximum invagination h of linear and non-linear ACN.

which for given σ and d has to be solved numerically. With $y_0 = d - \lambda_c/\sigma \cosh(p_0) - \lambda_c^2/2\sigma \cosh^2(p_0)$ the boundary line is fully determined.

Consider a circle with center $(x_m, y_m) = (x_0, 2\lambda_c/\sigma + 3\lambda_c^2/3\sigma + y_0)$. This gives

$$(x(p) - x_m)^2 + (y(p) - y_m)^2 = \left(\frac{\lambda_c(1+\lambda_c)}{\sigma}\right)^2 + \mathcal{O}(p^4). \tag{3.18}$$

So the boundary line collapses with a circular arc with radius $r = \lambda_c(1+\lambda_c)/\sigma$. As long as σ is not larger than 10^{-2} the relative deviation $(\lambda - \lambda_c(1+\lambda_c))/\lambda$ of this radius from the one obtained via the TEM is only 4%, that is in this regime, the elastic catenary model leads essentially to the same result as the TEM with circular arcs. However, in contrast to the TEM this model predicts a spatially varying boundary tension of

$$T(p) = \lambda_c \cosh(p) \ . \tag{3.19}$$

The curve without symbols in Fig. 3.9(b) shows that this model qualitatively predicts the observed minimum in the stress distribution. The force acting on an adhesion dot is predicted to be

$$f = \sqrt{2}\lambda_c \left(1 + \sinh(p_0)\right). \tag{3.20}$$

Fig. 3.9(d) shows that this prediction is quite accurate.

3.4 Strain Stiffening

So far, we have treated the network links as cables or springs, in which force increases linearly with elongation. Hence, the link length is unlimited in principle. As the links represent filament bundles, in practice they cannot be elongated above a finite contour length. Another important effect related to the finite contour length is the observation that thermal fluctuations lead to a non-linear force-extension curve, with a strong increase of the pulling force at an extension approaching the contour length (*strain stiffening*) [120]. To include these physically important effects in our approach,

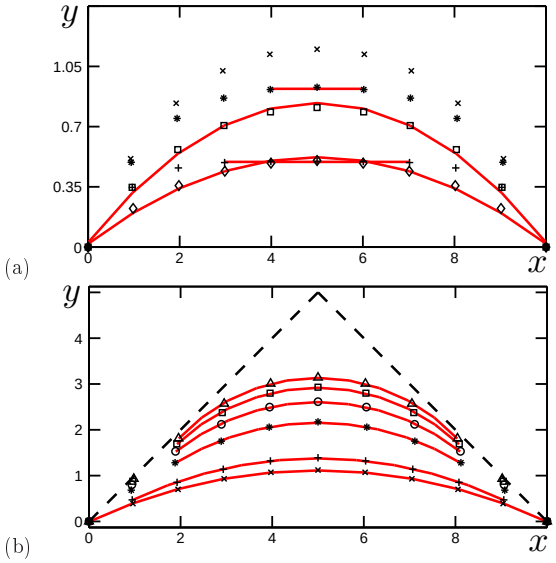

Figure 3.11: Arc fits for PCN and ACN with non-linear links. (a) Contour of the PCN-WLC from Fig. 3.10(b). Symbols belong to different values of τ_H: 0.1 (+), 0.2 (∗), 0.3 (×), 0.43 (□), 0.47 (◊). ◊ correspond to the bottom line of the network from Fig. 3.10(b). (b) Contour of the ACN-WLC from Fig. 3.10(c). Symbols are bottom line node positions, while the lines are circular fits. Motor force values are $\tau = 10^{-2}$ (×), 2×10^{-2} (+), 10^{-1} (∗), 2.5×10^{-1} (◯), 5×10^{-1} (□), 1 (△). Note, △ gives the bottom line from Fig. 3.10(c).

we now describe the elastic response of the network links by the worm-like-chain (WLC) model. The WLC model has been used before to model semiflexible biopolymers like DNA [121], actin [122, 123] and spectrin [71, 72]. While the WLC proper has vanishing resting length, here we combine it with a finite resting length to also include the effect of compression. Thus we use the WLC model to describe the mechanical links as they are tensed away from their reference state, while the compressed state is modeled as above (linear response for springs and no response for cables).

Complementing Eq. (2.2) for the PCN, we get

$$\vec{F}_{ij} = \begin{cases} \left(\frac{L_{ij}-L_0}{L_n} + \frac{1}{4} \left(\frac{1}{(1-(L_{ij}-L_0)/L_n)^2} - 1 \right) \right) \frac{k_B T}{L_0} \vec{e}_{ij}, & L_0 \le L_{ij}, \\ 0, & L_{ij} < L_0 \end{cases} \tag{3.21}$$

Here L_n is the difference between maximal extension and reference length. In dimensionless form we have:

$$\vec{f}_{ij} = \begin{cases} \left(u_{ij} + \frac{1}{4} \left(\frac{1}{(1-u_{ij})^2} - 1 \right) \right) \vec{e}_{ij} & u_{ij} > 0, \\ 0 & u_{ij} < 0 \end{cases} \tag{3.22}$$

Force is now given as multiples of $k_B T/L_0$, while length is again scaled with L_0. Strain is now defined as $u_{ij} = (\ell_{ij} - 1)/\ell_n$. Effectively there is only one difference to the original model, namely the additional term which diverges if the strain u_{ij} approaches 1. Without strain, this term vanishes.

For ACNs, Eq. (2.5), we obtain in dimensionless form:

$$\vec{f}_{ij} = \begin{cases} \left(u'_{ij} + \frac{1}{4} \left(\frac{1}{(1-u'_{ij})^2} - 1 \right) + \tau \right) \vec{e}_{ij}, & 1 < \ell_{ij}, \\ \tau \vec{e}_{ij}, & \ell_c \le \ell_{ij} \le 1 \\ \tau \frac{\ell_{ij}}{\ell_c} \vec{e}_{ij} & \ell_{ij} < \ell_c \end{cases} \tag{3.23}$$

We choose $\ell_n = 0.5$, that is the maximal extension is 1.5 L_0. For small tension, $\tau_H < 0.2$, the non-linearity does not affect the shape of the PCN much and we observe the same invagination as in Fig. 3.1. Fig. 3.10(a,b) shows a comparison between linear and WLC-networks for a large value of tension, $\tau_H = 0.47$. Obviously the strain-stiffened network shows a much larger resistance to invagination. We also note that forces are two orders of magnitude larger in the non-linear model.

ACNs are affected less by the non-linearity, as shown in Fig. 3.10(c). Here we use $\tau = 1$ and again $\ell_n = 0.5$. Comparison with Fig. 3.2(d) reveals that the ACN collapses to a lesser degree than without strain stiffening. This can be quantified by the arc height $h(\tau)$, defined as the maximum distance between initial and current edge in the equilibrium shape. h is significantly reduced by the non-linearity, Fig. 3.10(d). Thus much higher motor forces are needed to reach the collapsed state.

In Fig. 3.11(a), the contour of the strain stiffening PCN is analyzed in more detail. Circle/linear fits are shown as lines. The bottom two are given by straight lines. For $\tau_H < 0.3$ the contour of the PCN-WLC is qualitatively the same as that of the linear one, shown in Fig. 3.6(b). At $\tau_H = 0.3$ the contour cannot be fitted well by circle or line. If τ_H is increased beyond 0.3, the network does not contract any further, but again expands outward. This surprising effect is special to passive networks and does not appear for ACNs. For $\tau_H > 0.4$ the arcs appear to be circular. The ACN-WLC contour, Fig. 3.11(b), only differs little from the linear ACN contour, Fig. 3.6(b). Arcs are always circular (except at the regions where tubes form). With increasing τ they continuously move inward. Comparison with Fig. 3.6(a) reveals that radii typically are larger in the non-linear case.

In summary, the shapes and forces of ACNs are also surprisingly robust in regard to the inclusion of non-linear force-extension curves, in particular in regard to the strain stiffening effects which are expected to occur for actin filaments and bundles.

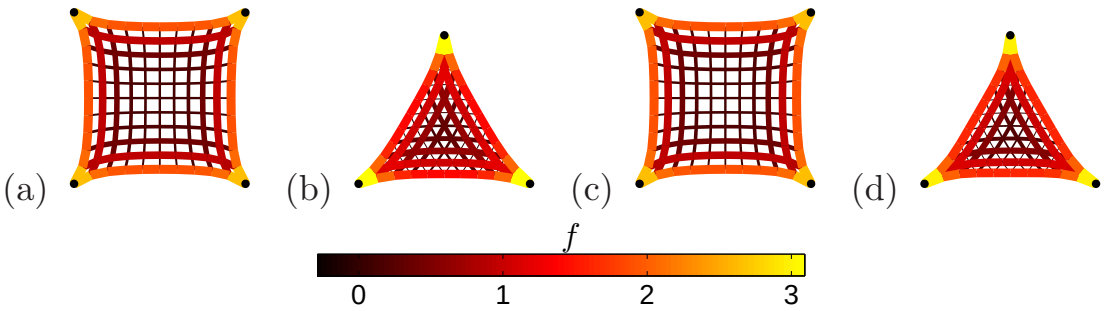

Figure 3.12: Equilibrium shapes for passive adaptive networks. (a) HSN in square geometry. On the boundary: $ea \approx 9.40$, at the center: $ea \approx 1.75$. (b) HSN in triangular geometry. $ea \approx 9.59$ on the boundary, $ea = 1$ on the thin arms leading to the adhesion points. (c) PCN in square geometry. Identical to (a). (d) PCN in triangular geometry. $ea \approx 9.55$ on the boundary, $ea = 1$ on the thin arms. Parameters are: $[ea]_1 = 10$, $f_0 = 0.5$.

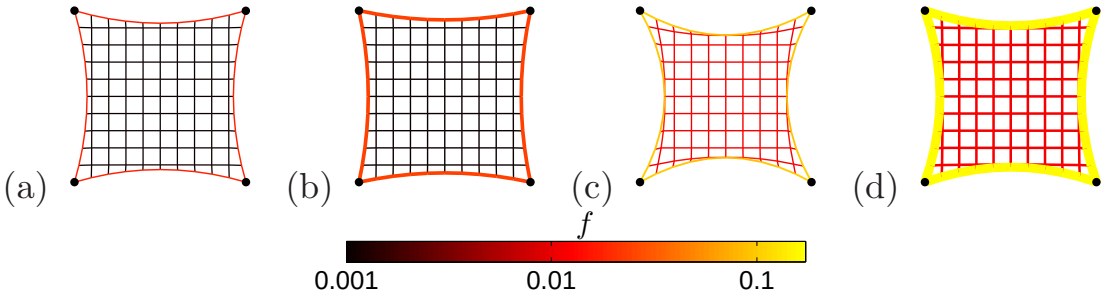

Figure 3.13: Equilibrium shapes for active adaptive networks. (a) Square ACN with $ea_p \approx 1.15$ for the peripheral links and $ea_i \approx 1.15$ for the internal links. (b) Here: $ea_p \approx 2.9$ and $ea_i \approx 1.1$. (c) Here: $ea_p \approx 1.5$ and $ea_i \approx 1.5$. (d) Here: $ea_p \approx 7.1$ and $ea_i \approx 2$. Parameters are: $\tau_0 = \tau_1 = 10^{-3}$ (in (a) and (b)), $\tau_0 = \tau_1 = 10^{-3}$ (in (c) and (d)), $[ea]_1 = 1$ (in (a) and (c)), $[ea]_1 = 10$ (in (b) and (d)), $f_0 = 0.1$.

3.5 Link Adaptation

Adherent cells are known to strongly adapt their cytoskeleton to the physical properties of their environment. During recent years, it has become clear that the actin cytoskeleton tends to reinforce under load [124]. In addition, mechanical loading of adhesion contacts leads to regulatory signals which increase myosin motor activity inside the cell. Network models are especially suited to study these biologically important effects in a theoretical framework. In the following, we will investigate which changes occur in the network if the elastic constant EA and the motor force density T are increasing with load.

For simplicity, we assume the same force-dependence for both EA and T. We assume that both quantities initially increase in a linear fashion and then saturate at constant values, which is the simplest assumption for a process based on enzymatic regulation:

$$EA(F) = [EA]_0 + [EA]_1 \frac{F}{F + F_0}, \tag{3.24}$$

$$T(F) = T_0 + T_1 \frac{F}{F + F_0}, \tag{3.25}$$

where the force scale F_0 determines when half the maximal increase has been reached. We again use dimensionless parameters. Forces EA, T, F are measured in units $[EA]_0$, i.e. we define $\tau := TL_0/[EA]_0$ (the same for τ_0 and τ_1), $ea := EA/[EA]_0$ (the same for $[ea]_1$, $[ea]_0 = 1$) and $f := F/[EA]_0$ (the same for f_0).

For passive networks only Eq. (3.24) must be considered. The results are shown in Fig. 3.12, where we use the reference states from Fig. 2.2 and apply regulation. The thicker the link is displayed the stiffer it is. For both, HSN and PCN, the peripheral links show the largest values of ea. Links parallel to the boundary exhibit stiffnesses smoothly decreasing with distance from the boundary.

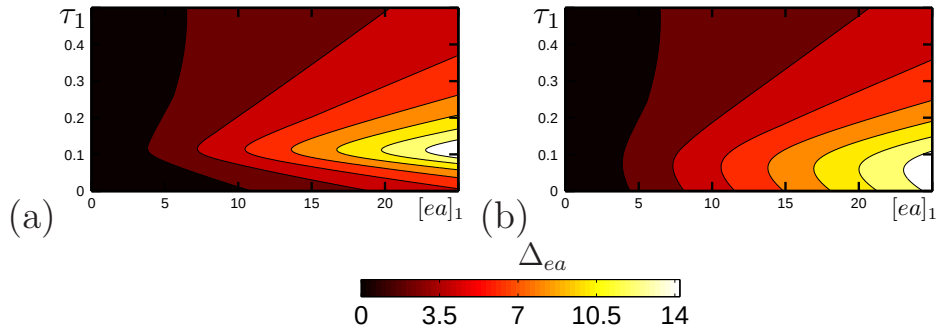

Figure 3.14: Inhomogeneity Δ_{ea} of the ACN as a function of parameters τ_1 and $[ea]_1$. Parameter values are $f_0 = 0.1$ and $\tau_0 = 10^{-3}$ (in (a)), $\tau_0 = 10^{-2}$ (in (b)).

We next analyze the ACN from the reference state shown in Fig. 2.2(a) in combination with Eqs. (3.24) and (3.25). Fig. 3.13 shows the equilibrium shapes. To be able to compare to the non-adaptive case (Fig. 3.2(a,b)), we choose the same motor forces here. For $[ea]_1 = 1$ we do not observe strong inhomogenization. However, if $[ea]_1$ is increased to 10, Fig. 3.13(b,d), the peripheral links clearly become stiffer than the internal ones. For the adhesion geometry considered here, all the peripheral links have almost the same stiffness. The same holds for the rest of the links. We can therefore describe different shapes just by measuring their maximum M_{ea} and minimum m_{ea} equilibrium link stiffness. In Fig. 3.14 we present $\Delta_{ea} := M_{ea} - m_{ea}$ as function of $[ea]_1$ and τ_1. Increase of $[ea]_1$ or τ_1 leads to stiffer links. Increase of $[ea]_1$ at constant τ_1 leads to a larger difference between stiffness in boundary and interior. Beyond a certain threshold (≈ 0.1 in Fig. 3.14(a)) increase of τ_1 leads to equal stiffnesses in boundary and interior of the network.

In summary, for passive networks the adaptation response is spatially continuous, while for actively contracting networks, it is strongly localized to the rim. This nicely agrees with experimental observations that strong peripheral actin bundles typically line the cell contour [15]. In particular, our model suggests that this effect is strongly determined by the mechanical properties of the underlying networks.

3.6 Relation to Tissue Shape

Tissue contraction with discrete pinning sites is very similar to cell contraction since adherent tissues also show invaginated arcs [15, 125]. However, in this case the spatial dimensions of the pinning objects tend to be relatively large. In order to include this effect, we have simulated a circular network contracting around four circular dots of finite size, see Fig. 3.15(a). All nodes on the circles are fixed in space. Motor force τ is increased stepwise and nodes coming closer to each other than $\ell_c = 0.01$ are glued together and in the following act as one [44]. Relative dimensions are taken from [125], where a microtissue tethered to four cylindrical posts is analyzed. With the ACN we

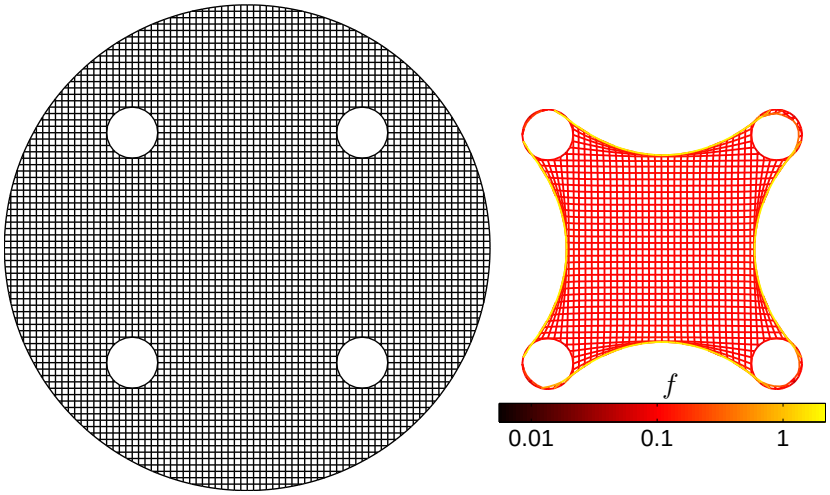

Figure 3.15: Contraction of an ACN anchored to dots of finite size. (a) Initial situation. Round tissue with radius r_t adherent to 4 round dots of finite radius r_d which form a square with side length d_d: (b) Contracted tissue. Parameters are: $r_t = 38$, $r_d = 4$, $d_d = 36$, $\tau = 0.1$.

are able to reproduce the typical arc morphology of the contracted microtissues, see Fig. 3.15(b). We note that this is not possible with a FEM model approach, as this leads to flat contours as for HSN [125]. Thus ACN are a useful model both for cells and tissues.

3.7 Homogenization

In the networks considered up to this point, the bond length of the undeformed reference state was assumed to be 100 nm. However, tissue cell dimensions normally are up to 100 μm, i.e. 1000 times larger. Hence, in this section we view the cell cytoskeleton as a continuous material. We discuss a homogenization approach of the presented models. Thereby, we follow a homogenization technique which was used previously to describe actin networks growing from a cylinder surface [78].

Consider again the square network from Fig. 2.2(a) but for large n, see Fig. 3.16 (left). Then each node in the undeformed reference state can be addressed via $(\nu_x, \nu_y) \in \{0, .., n\}$, Fig. 3.16 (middle). The homogenization step transforms the discrete variables (ν_x, ν_y) into coordinates $(\lambda_x, \lambda_y) \in [0; d]^2$, Fig. 3.16 (right) (with $\lambda_i = \nu_i \ell$, $i = x, y$). The node positions in the deformed state are given by a continuous function $\vec{\varphi}(\lambda_x, \lambda_y)$.

In the square topology two links, $\vec{B}_x$ and $\vec{B}_y$, are sufficient to span each cell, Fig. 3.16 (middle). In λ_x-direction we can use a Taylor expansion to get

$$\vec{\varphi}(\lambda_x + \ell, \lambda_y) \approx \vec{\varphi}(\lambda_x, \lambda_y) + \ell \partial_{\lambda_x} \vec{\varphi} \tag{3.26}$$

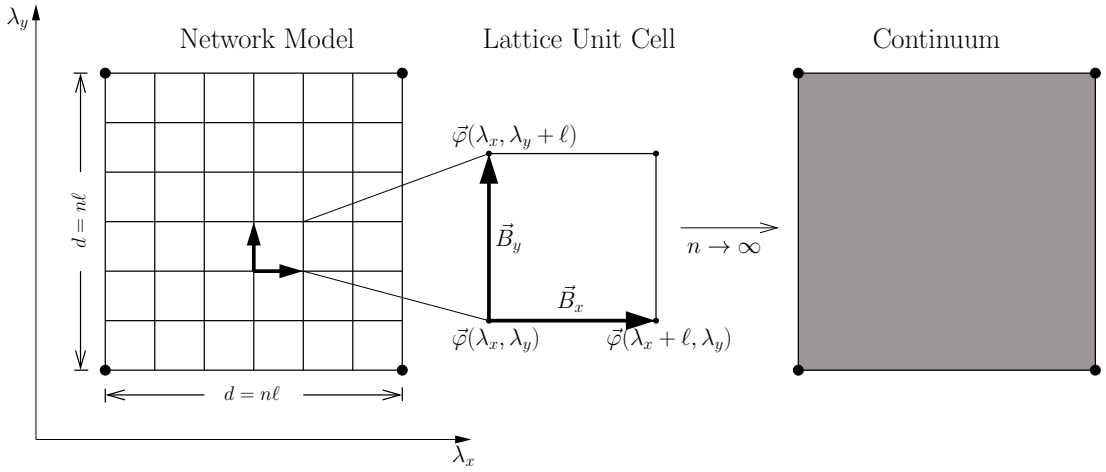

Figure 3.16: Homogenization of square networks. The lattice unit cell (LUT) in the S1 network is spanned by the basis $\{\vec{B}_x, \vec{B}_y\}$. Therefore, $\vec{B}_x$ and $\vec{B}_y$ span the whole network. In the limit $n \to \infty$ the network becomes a continuum.

and therefore

$$\vec{B}_x \approx \ell \partial_{\lambda_x} \varphi \tag{3.27}$$

The situation for λ_y is completely analog: $\vec{B}_y \approx \ell \partial_{\lambda_y} \varphi$. In the following we will abbreviate $\partial_i := \partial_{\lambda_i}$ for $i = x, y$.

For one lattice unit cell (LUT) of the HSN the free elastic energy is given by:

$$\begin{aligned} \mathrm{f}(\vec{B}_x, \vec{B}_y) &= \frac{k}{2}\left((|\vec{B}_x| - \ell_0)^2 + (|\vec{B}_y| - \ell_0)^2\right) = \\ \mathrm{f}(\vec{\varphi}) &= \frac{k\ell^2}{2}\left((|\partial_x \vec{\varphi}| - \overline{\tau}_H)^2 + (|\partial_y \vec{\varphi}| - \overline{\tau}_H)^2\right). \end{aligned} \tag{3.28}$$

Here $\ell_0 \leq \ell$ denotes the springs' resting length, which is related to the tension of HSNs τ_H via $\ell_0/\ell = 1 - \tau_H$. In the following we abbreviate $\overline{\tau}_H := 1 - \tau_H$. k is the spring constant. For the whole network f has to be integrated

$$\begin{aligned} F[\vec{\varphi}] &= \frac{1}{\ell^2} \int\limits_{[0;d]^2} dxdy \mathrm{f}(\vec{\varphi}(x,y)) \\ &= \frac{k}{2} \int\limits_{[0;d]^2} dxdy \left((|\partial_x \vec{\varphi}| - \overline{\tau}_H)^2 + (|\partial_y \vec{\varphi}| - \overline{\tau}_H)^2\right). \end{aligned} \tag{3.29}$$

The first variation of the free energy F with respect to the continuous function $\vec{\varphi}$ is given by $\delta F = \partial_\epsilon F[\vec{\varphi} + \epsilon \delta\vec{\varphi}]|_{\epsilon=0}$. This gives:

$$\delta F = \frac{k}{2} \int\limits_{[0;d]^2} dxdy \left(\frac{|\partial_x \vec{\varphi}| - \overline{\tau}_H}{|\partial_x \vec{\varphi}|}(\partial_x \vec{\varphi}) \cdot (\partial_x \delta\vec{\varphi}) + \frac{|\partial_y \vec{\varphi}| - \overline{\tau}_H}{|\partial_y \vec{\varphi}|}(\partial_y \vec{\varphi}) \cdot (\partial_y \delta\vec{\varphi})\right) \tag{3.30}$$

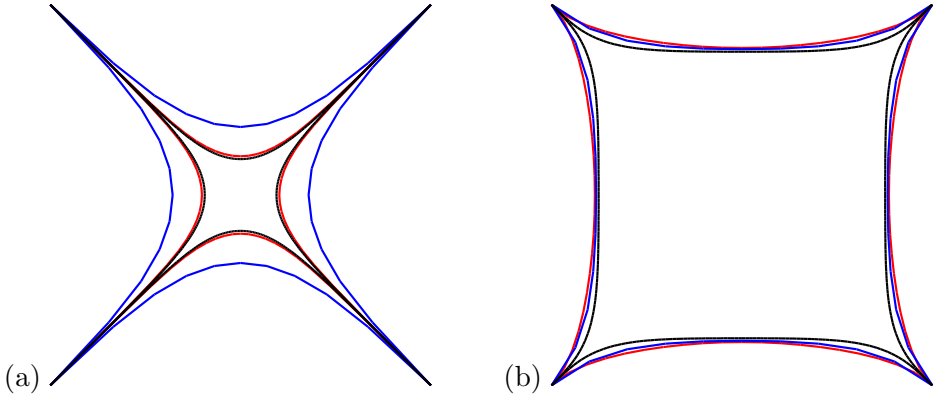

Figure 3.17: Boundary line for HSN obtained by homogenization. (a) The blue line gives the result from the numerical simulation with $\overline{\tau}_H = 0$ and $\ell = 1$. The simulation result for $\ell = 0.1$ and $\overline{\tau}_H = 0$ (black) and the solution of the Laplace equation (red) are almost perfectly collapsed. (b) Boundary lines for simulations $\tau_H = 0.25$ and solutions of Eq. (3.32) with $\overline{\tau}_H = 0.75$. Colors are analog to those in (a). The side length of the networks is $d = 10$. We use $dx = 0.5$ for the finite differencing algorithm.

Integrating by parts gives, since the boundaries are not varied ($\delta\vec{\varphi} = 0$ at adhesions):

$$\delta F = -k \int\limits_{[0;d]^2} dxdy \left(\partial_x \left(\frac{|\partial_x\vec{\varphi}| - \overline{\tau}_H}{|\partial_x\vec{\varphi}|}(\partial_x\vec{\varphi}) \right) + \partial_y \left(\frac{|\partial_y\vec{\varphi}| - \overline{\tau}_H}{|\partial_y\vec{\varphi}|}(\partial_y\vec{\varphi}) \right) \right) \cdot \delta\vec{\varphi}. \quad (3.31)$$

Because the test function $\delta\vec{\varphi}$ was chosen arbitrarily, $\delta F = 0$ requires

$$\partial_x\vec{S}_x + \partial_y\vec{S}_y = 0, \quad (3.32)$$

with the stresses $\vec{S}_x$, $\vec{S}_y$ given by

$$\vec{S}_x = \frac{|\partial_x\vec{\varphi}| - \overline{\tau}_H}{|\partial_x\vec{\varphi}|}(\partial_x\vec{\varphi}), \quad (3.33)$$

$$\vec{S}_y = \frac{|\partial_y\vec{\varphi}| - \overline{\tau}_H}{|\partial_y\vec{\varphi}|}(\partial_y\vec{\varphi}). \quad (3.34)$$

The adhesions at the corners are kept fixed, hence we have Dirichlet boundary conditions (BCs):

$$\varphi_1(0,0) = \varphi_1(0,d) = \varphi_2(0,0) = \varphi_1(d,0) = 0, \quad (3.35)$$

$$\varphi_1(d,0) = \varphi_1(d,d) = \varphi_2(0,d) = \varphi_1(d,d) = d. \quad (3.36)$$

The stress orthogonal to the cell boundary must vanish in equilibrium:

$$S_\perp = 0. \quad (3.37)$$

Hence, the system of equations (3.32)-(3.37) can be solved numerically. For $\overline{\tau}_H = 0$ ($\tau_H = 1$) this equation system reduces to the Laplace equation $\Delta\vec{\varphi} = 0$ with the

Dirichlet BCs, Eqs. (3.35),(3.36), and the Neumann BCs $\partial_x\vec{\varphi} = 0$ and $\partial_y\vec{\varphi} = 0$ at the free edges. This system can easily be solved with finite difference methods, see the appendix A.1 for more information. Fig. 3.17(a) shows the solution of the Laplace equation in comparison to simulation results. For large lattice constant $\ell = 1$ the homogenized boundary is not a good approximation, but for finer lattices the boundary fits very well. The homogenization can be seen as the limit of small lattice constants, as one could expect.

For $\tau_H < 1$ the situation is more difficult, because then the stresses Eqs. (3.33) and (3.34) cannot be simplified. Motivated by the boundary line from Fig. 3.3(a), which shows that HSNs for moderate tensions $\tau_H \approx 1$ only close to the boundary differ from the freely compacting shape, we assume homogeneous contraction of the network orthogonal to the boundary. For the Neumann BCs this yields:

$$\partial_x\varphi_1(0,y) = \partial_x\varphi_1(d,y) = \overline{\tau}_H, \tag{3.38}$$
$$\partial_y\varphi_2(0,y) = \partial_y\varphi_2(d,y) = 0, \tag{3.39}$$
$$\partial_x\varphi_1(x,0) = \partial_x\varphi_1(x,d) = 0, \tag{3.40}$$
$$\partial_y\varphi_2(x,0) = \partial_y\varphi_2(x,d) = \overline{\tau}_H \quad \forall x,y \in [0,d]. \tag{3.41}$$

The numerical solution of Eq. (3.32) for $\overline{\tau}_H = 0.75$, i.e. $\tau_H = 0.25$ in combination with Eqs. (3.38)-(3.41) is shown in Fig. 3.17(b). Qualitatively, there is good agreement between the homogenization solution and the simulation result for $\ell = 1$. But this boundary is definitely not the continuum limit of the network, see in particular the corners which for $\ell \to 0$ become very thin. This cannot be reproduced in the homogenization approach, if using the BCs from Eqs. (3.38)-(3.41), which are only exact at the center of the boundary, where the three lines collapse. The problem of closure of the equations is even worse for ACNs, which we cannot homogenize with this technique. Therefore, we shift the homogenization approach of ACNs to the appendix A.2.

3.8 Arc Geometry in 3D Structures

In this section we extend the network models to three spacial dimensions to model ACN cubes. Naively there are two starting points for a 3D extension of the ACN. On one hand there are the experiments on fibroblasts in 3D scaffolds [126], which resemble two-dimensional mats rotated in space. This motivates the discussion of a cube fixed at its corners which only consists of its 6 square surfaces. We show such a contracted cube in Fig. 3.18(a). The invagination on the cube edges is very similar to the invagination of the boundary line for the 2D network. Different to the flat network, the surface shows vertical invaginations as well, see Fig. 3.18(c). On the other hand, we model a complete three-dimensional cube, whose inner is filled with a cubic network, i.e. an actively contracting three-dimensional material. Of course there is stronger invagination of surfaces and edges compared to the hollow situation, see Fig. 3.18(b) and (d). But in both cases the cube edges appear circular.

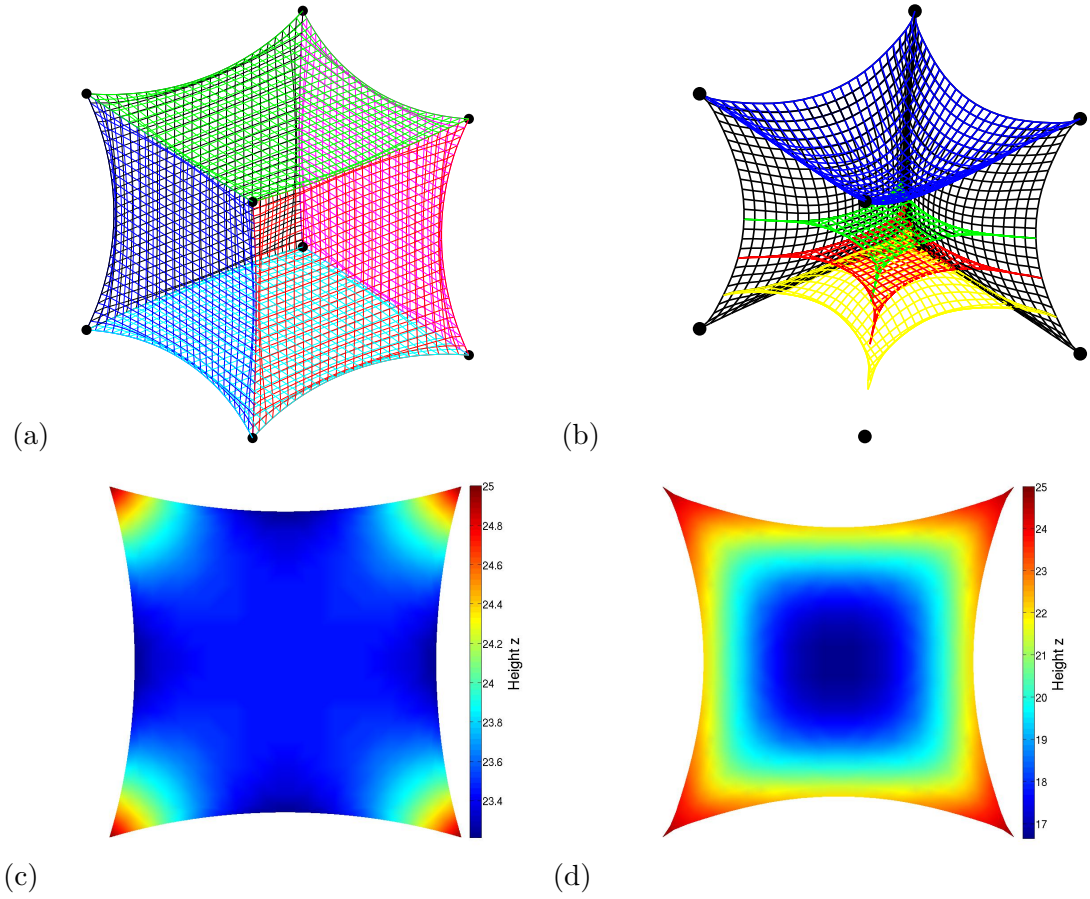

Figure 3.18: 3D shapes of ACN cubes. (a) Only boundary areas. (b) Filled 3D network. For visualization reasons only three surfaces and three initially parallel planes are shown. Dots denote fixed points. (c) and (d) Cubes from (a) and (b) seen from above. Nodes have been interpolated to give a continuous height function. In (a) and (b) different link colors are used for different surfaces. Colors in (c) and (d) give the height of the top surface in z-direction. We chose $\tau = 7 \times 10^{-4}$ and $d = 25\ell$ here.

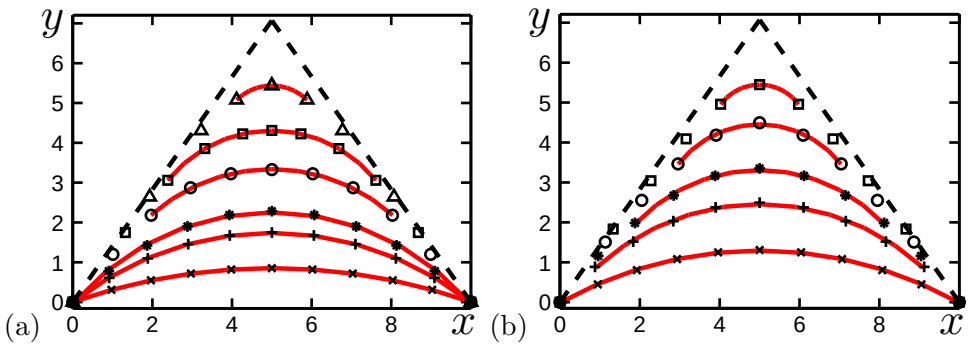

Figure 3.19: Arc fits for ACN in cube shape. (a) Contour analysis of the hollow cube. We plot the line which initially collapses to the x-axis with $\tau = 10^{-3}$ ($\times$), 10^{-2} ($+$), 2.5×10^{-2} ($*$), 10^{-1} ($\bigcirc$), 2.5×10^{-1} ($\square$), 5×10^{-1} ($\triangle$) from bottom to top. Symbols denote node positions of the network arcs while the lines are least square fits of the contours to arcs of constant curvature. (b) Contour analysis of the filled cube. Analog to the analysis in (a), here parameters are $\tau = 10^{-3}$ ($\times$), 10^{-2} ($+$), 2.5×10^{-2} ($*$), 5×10^{-2} ($\bigcirc$), 7.5×10^{-2} ($\square$) from bottom to top.

To test the circularity of the cube edges, we analyzed the cube edge which initially collapses with x-axis. This line is first rotated into the xy-plane, so the same least-square fitting procedure as discussed in section 3.2 can be applied.

We basically observe the same features for the 3D network as for the 2D network, Fig. 3.19. Increase of motor force leads to network collapse to the CT, which is different from the 2D case because the remaining non-adherent node is located at the center of the cube. It has a distance $\sqrt{3}d/2$ to the fixed points. Comparing Fig. 3.19(a) and (b) we learn that there is much less motor force needed to reach the CT if the network is filled. This result is not surprising, since the internal links contribute to invagination.

3.9 Summary

Motivated by the network nature of the actin cytoskeleton and its effectively 2D organization in mature adhesion to flat substrates, we have modeled adherent tissue cell contraction by 2D network models. The main aim of this chapter is to achieve a detailed comparison of the shapes and force patterns for different network types, namely Hookean spring networks (HSNs), passive cable networks (PCNs), and active cable networks (ACNs).

The shape of a HSN can be understood best by considering the shape of its unconstrained reference shape. If tension is not too large, the network contour follows the unconstrained reference shape at regions sufficiently far away from the adhesion sites. Closer to the adhesion sites, the network deforms and stress and strain accumulate. In contrast, the ACN does not have an unconstrained reference shape and without adhesion constraints would contract into a point. Therefore no signature of the unconstrained reference shape (like flat parts for a square-shaped lattice) appear in the

contour. Because it does not resist compression, stress and strain are not propagated much into the network and are strongly localized to the contour.

One of the most striking difference between the different network types revealed by our analysis is the fact that in passive networks, local changes to the adhesion geometry changes the network globally. This is in marked contrast to the active network, where the addition of local adhesions has only a local effect on the boundary. However, in this case the change in spanning distance has a large effect on the stress in the contour, as predicted by the tension-elasticity model (TEM). The TEM is especially suited to quantitatively predict the shape of an ACN, namely the circular arcs observed between neighboring adhesion points and the scaling of their radius with spanning distance and surface tension.

Despite this success, the TEM does not capture all aspects of the network model. While the TEM assumes constant contour tension, the computer simulations reveal that tension varies along the contour. An elastic catenary theory qualitatively predicts that tension decreases towards the middle of an invagination due to local changes in link density along the contour. However, it does neither predict the quantitative details of the contour stress nor the circular arc morphology.

In the case of very large tension, both network types develop different features. For the passive networks, the invaginations tend to become more round, as the unconstrained reference shape becomes so small that the contour cannot reach it anymore. In contrast, the active network develops straight features, because the network collapses into tubes at the adhesion points. Indeed the formation of tubes has been observed experimentally and eventually leads to pearling through a Rayleigh-Plateau instability [82]. The region between the tubes always stays circular for ACN.

Network models are ideally suited for multi-scale modeling because physical properties can be easily added on the level of single link and lead to non-trivial effects on the level of cell shape and forces. In order to demonstrate this important aspect, we have studied two important additional features of the cytoskeleton. First non-linear links were introduced via the worm-like-chain model (WLC). In the WLC case the passive square network first contracts and then expands again as tension is increased. The ACN requires much larger tension values to contract compared to the linear case. Otherwise the arc morphology is essentially the same as in the linear case.

As a biologically very relevant aspect of the cellular cytoskeleton, we also have studied the adaptation response of network links. For certain parameter values, a saturation response for both elasticity and tension leads to a strong difference between EA and T of boundary links, which are strongly increased, and EA and T of internal links, which are increased much less. Similar aspect have been addressed before in the framework of Finite Element Modeling (FEM) [79]. In this case, the biochemical regulation has been modeled with more detail. Both the resulting cell shapes and the formation of stress fibers inside the cell demonstrate that the FEM model strongly resembles the HSN studied here. Therefore it would be interesting to combine the detailed biochemical model with the actively contracting cable network studied here.

Active cable networks have also been shown to describe the circular arc morphology of tissues pinned at discrete sites [15]. Because here arc radius also scales with spanning distance as for the arc radius of strongly adhering cells, the tension-elasticity model seems to capture all essential element of this situation. In the tissue case, the cable network represents the fibrous nature of the collagen matrix and the active contractility corresponds to cell contraction. Because in addition water can flow out of the contracting cell-matrix composite, volume is not conserved and compression is not propagated. Therefore the standard models of elasticity are strictly speaking not appropriate. Indeed they do not predict the circular arc morphology, but rather show flat contours corresponding to the unconstrained reference shape of the elastic model [125].

It remains a challenging task to relate the microscopic network model to a macroscopic continuum theory. By applying a homogenization technique to the HSN, we were able to reproduce its equilibrium shape by solving a partial differential equation. It is desirable to improve this technique and to bridge the gap between the ACN and continuum theories of active materials.

We briefly discussed extensions of the ACN to three spacial dimensions. For this purpose, we modeled cubes of active cables. If the cubes consists only of their surfaces, the cube edges behave similar to the edges of flat square networks. Moreover, for small motor forces, maximum invagination in $3D$ is proportional to maximum invagination in $2D$.

In summary, HSN, PCN and ACN are simple model systems which however show surprisingly rich responses to internal contractility and therefore lead to interesting conclusions about the physical elements required to endow cells with a sense of geometry. ACN seem to be very appropriate to model strongly adherent tissue cells as they not only implement some of the most important fundamental features of the cytoskeleton (asymmetry under tension and compression, contraction by molecular motors), but also lead to functions which are very reminiscent of real cells (robustness under structural re-arrangements and adaptation to local adhesion constraints).

4

Application of the Active Cable Model to Experimental Data

In this chapter we use the ACN model introduced in the previous chapter to analyze the traction stress distribution of several tissue cells adherent to the surface of elastic substrates. Therefore, our experimental collaborators from the Gardel Lab (University of Chicago, IL, USA) provided actin- and paxillin-stained cell images as well as associated traction stress data obtained via TFM for different cell types. We assume that in these cells actin and paxillin are present over the whole cell area. Hence, segmenting e.g. the actin part out of the actin-stained images gives the cell area and segmentation of islands of high intensity out of the paxillin-stained images gives focal adhesion masks. FA masks are necessary to find the network nodes which connect the actin network to the substrate. Using the active cable network, we are able to achieve good agreement with the experimental data in regard of cell shape and traction stress. Please note: Every experimental data we present in this chapter and in the appendix B is courtesy of the Gardel Lab.

4.1 Cells without Stress Fibers

In Fig. 4.1 on the left we show the paxillin-stained images, since we do not have actin data, for two Madin-Darby canine kidney (MDCK) cells ((a): cell A, (b): cell B). After contrast enhancement, cell area can be recognized with the eye. Like in the previous section we assume that the nucleus, the black spot in the center, plays a minor role for lateral contraction. Therefore we disregard it.

We apply the algorithms GrowCut, see section 2.6.2, and DistMesh, see section 2.6.3, to produce the tension-free reference states of the cells. These are shown on the right of Fig. 4.1 as background (red). The contracted equilibrium state (blue) of the ACN is plotted in front of this. The network nodes shown in black coincide with regions of very high signal intensity, i.e. FAs (bright white spots on the paxillin images). Therefore, these nodes are kept fixed during the simulations.

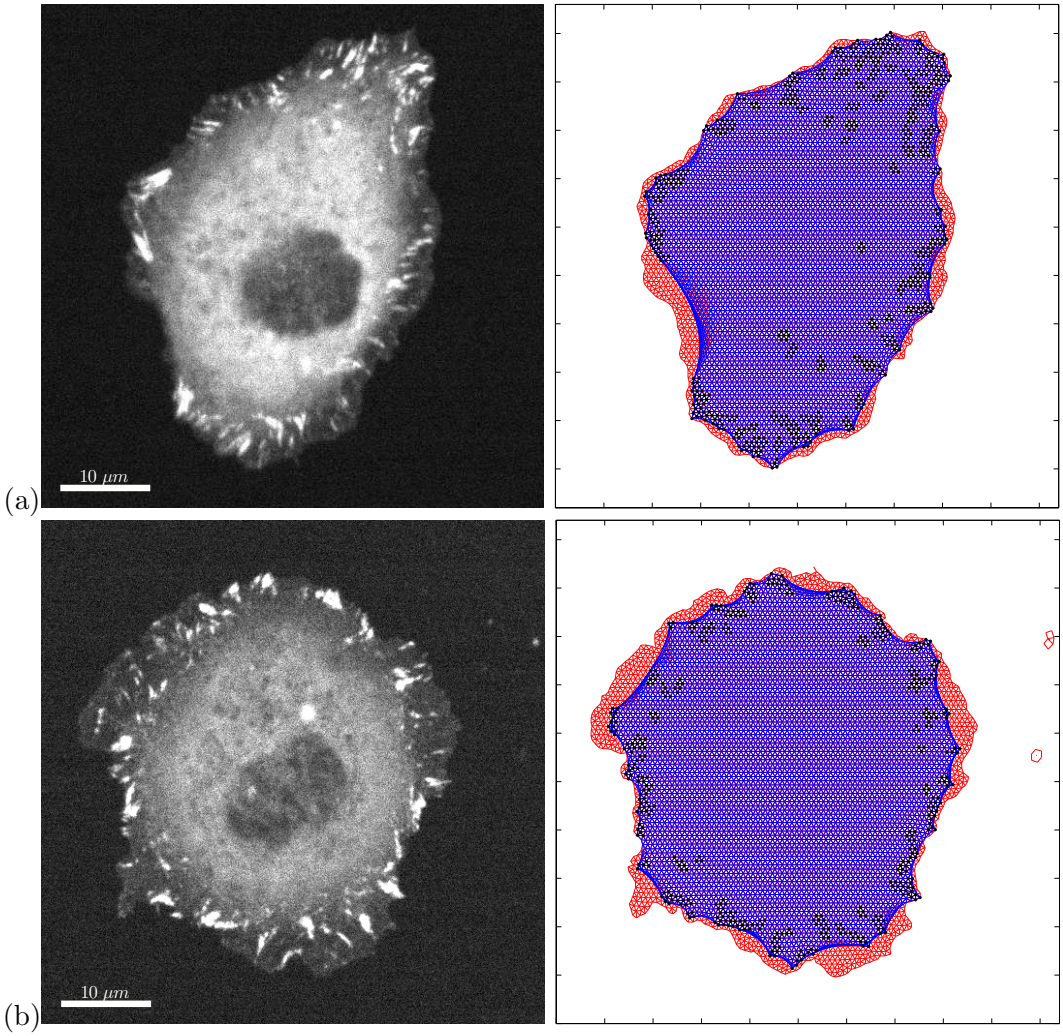

Figure 4.1: Cell shape of MDCK cells. Paxillin-stained images of Madin-Darby canine kidney (MDCK) cells (black and white, paxillin density increases with signal intensity). Tension-free reference states obtained with GrowCut and DistMesh (red), contracted equilibrium states for $\tau = 3 \cdot 10^{-5}$ (blue), mean initial link length $\bar{\ell} = 5\ px$, with $1\ px = 0.107\ \mu m$. To model adhesion we fixed the nodes located at the FAs (marked as black dots). The length of the bar is 10 μm.

We see in both, Fig. 4.1(a) and (b), that the initial (red) area has shrunk to the contracted (blue) area due to motor force. In particular, all links in the intersection have strongly contracted. The boundary between red and blue can be interpreted as the lamellipodium-lamella interface, since the lamellipodium does not adhere to the substrate at the leading edge. In contrast to cell B, cell A exhibits a large spanning distance between two FAs on its left side and therefore strong invagination. If one aims at a more adequate description of cell A, it might therefore be necessary to introduce some boundary reinforcement to prevent this strong invagination.

Now we explore the traction stress the cells apply to the substrate. In the experiments, this is done via TFM. As discussed in the introduction, substrate strain is obtained by measurement of fluorescent marker positions. First, with the cell on the substrate, and then without the cell. This measurement is biased by noise in the cell. Hence, for the traction stress reconstruction the FTTC regularization scheme is applied. We have described it in more detail in section 2.6.4. In contrast to the experiment, simulation results are proper. That is, we know the exact position and traction force on every fixed node, i.e. on every adhesion. In order to put the simulation results on the same level as the experimental ones, we calculate the substrate deformation. For this purpose we use the FEM program celldeform, compare section 2.6.5. We can then apply FTTC with the same regularization parameter to obtain the traction stress distribution.

We show the traction stress magnitudes of MDCK cells in Fig. 4.2. Both cells show stress accumulation at the FAs close to the boundary. Note, there is an abnormality of unknown origin in the center of cell B. If we ignore this abnormality, we find that the traction stress distributions obtained numerically fit the experimental results quite well. See in particular the two maxima at the left of cell A (simulation result). This stress increase results from the large spanning distance of the FAs, hence this can be understood with the TEM. The two large stress peaks at the top of cell A cannot be understood in our framework. We can only speculate, that some actomyosin concentration up there might cause the large stress.

We have analyzed another MDCK cell (see appendix B.1 for details). Although this cell was experimentally studied on a much softer substrate ($E_S = 8.4\ kPa$) than cells A and B ($E_S = 16.2\ kPa$), we numerically find well reproduction of traction stress distribution using the same parameters. For all three cells we use mean link length $\ell = 5\ px$ and motor force density $\tau = 3 \cdot 10^{-5}$, which with Eq. (2.7) and $EA = 50\ nN$, $L_0 = 1\ px = 0.107\ \mu m$ leads to $T \approx 14\ pN/\mu m$. That is, there are 7 myosin II heads bound to one actin filament of length 1 μm at a time, i.e. there is very low myosin II activity in MDCK cells.

In general we can say that the ACN leads to stress accumulation at the boundary peaked at focal adhesions. The larger the distance between the FAs, the higher the stress. This appears to be sufficient for MDCK cells, but for fibroblasts and other cells with stress fibers this is certainly not true, as we will discuss in the next section.

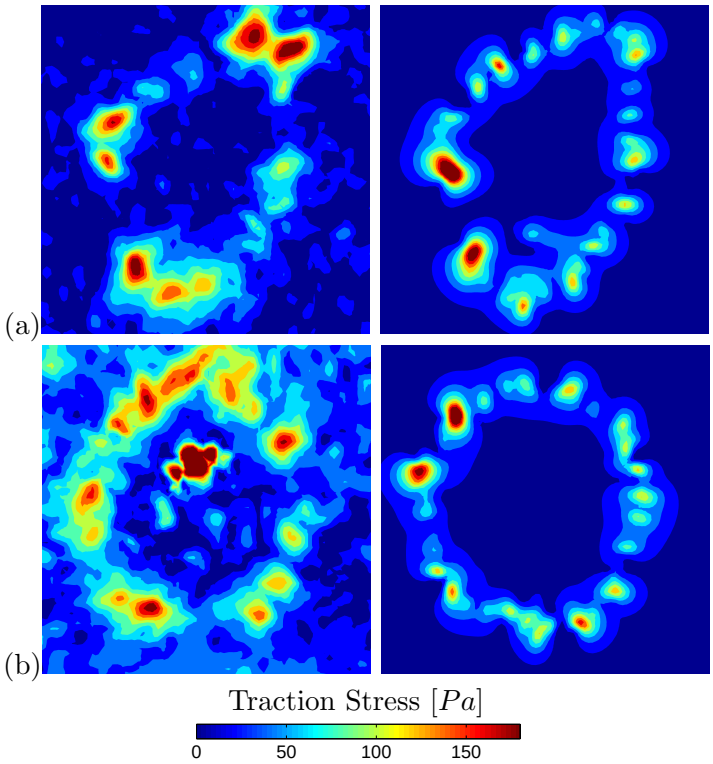

Figure 4.2: Magnitude of the traction stress applied by MDCK cells. For the cells from Fig. 4.1(a) and (b). The experimental result is shown on the left while its corresponding simulations result we depict on the right. Parameters are the same as in Fig. 4.1.

4.2 Cells with prominent Stress Fibers

We performed the same operations also for other cell types. Fig. 4.3(a) and (b) show the cell shapes for U2OS cell and a 3T3 fibroblast, respectively. This figure is arranged similar to Fig. 4.3 with an actin-stained image instead of a paxillin one. In general, cells of these types do not show FAs arranged in such a regular fashion, as found e.g. in Fig. 4.1(b). Hence, modeling fibroblasts and U2OS cells by the simple ACN leads to strong invaginations of the cell boundary accompanied by stress accumulations at FAs with large spanning distances.

Unfortunately due to lack of data for MDCK cells we cannot directly compare the actin images. However, there are many pronounced elongated structures of high intensity, i.e. stress fibers, visible for 3T3 and U2OS cells. The different kinds of SFs can be easily identified by hand. SFs reinforcing the boundary are TVAs, while DSFs usually are oriented orthogonal to the cell boundary with their distal end (the one which is closer to the boundary) at a focal adhesion. VSFs are the long straight structures which can cross the cell center. We model SFs as described in 2.2, namely with different motor force densities, τ for normal network links, τ_d for DSFs, τ_t for TVAs, τ_v for VSFs.

We found that increase of tension per length in DSFs and TVAs compared to normal filaments and VSFs leads the ACN to reproduce cell shape, see Fig. 4.3. Please note, since VSFs are not integrated into the meshwork the force they apply to their associated FAs scales with their total length, whereas DSFs force on FAs only scales with the mean link length of the network.

Fig. 4.4(a) and (b) show the traction stress magnitudes for 3T3 fibroblasts and U2OS cells, respectively. Compared to MDCK cells traction stress is much larger here. We can identify distinct force peaks which can be reproduced with the ACN, left. The stress peaks between boundary and nucleus indicate that these SFs and FAs possibly are not connected in the real cell. This might be an error due to the 2D approximation, because DSFs grow above these FAs.

4.3 Manipulation of Stress Fiber Formation

Fig. 4.5 (left) shows an U2OS cell treated with an inhibitor for the formin mDia. Since this prevents SF formation, their number is drastically reduced compared to U2OS cells in wild type. However, motor force density of the different components is obviously not affected by mDia inhibition. So we find the same optimal parameters valid for mDia inhibited cells as for the wild type U2OS cells. That is, mDia inhibition does not affect the motor force density in existing stress fibers.

4.4 Manipulation of Stress Fiber Contractility

In this section we explore the influence of Y-27632 on SF contractility, i.e. motor tension. Therefore we discuss several U2OS cells treated with different amounts of this agent.

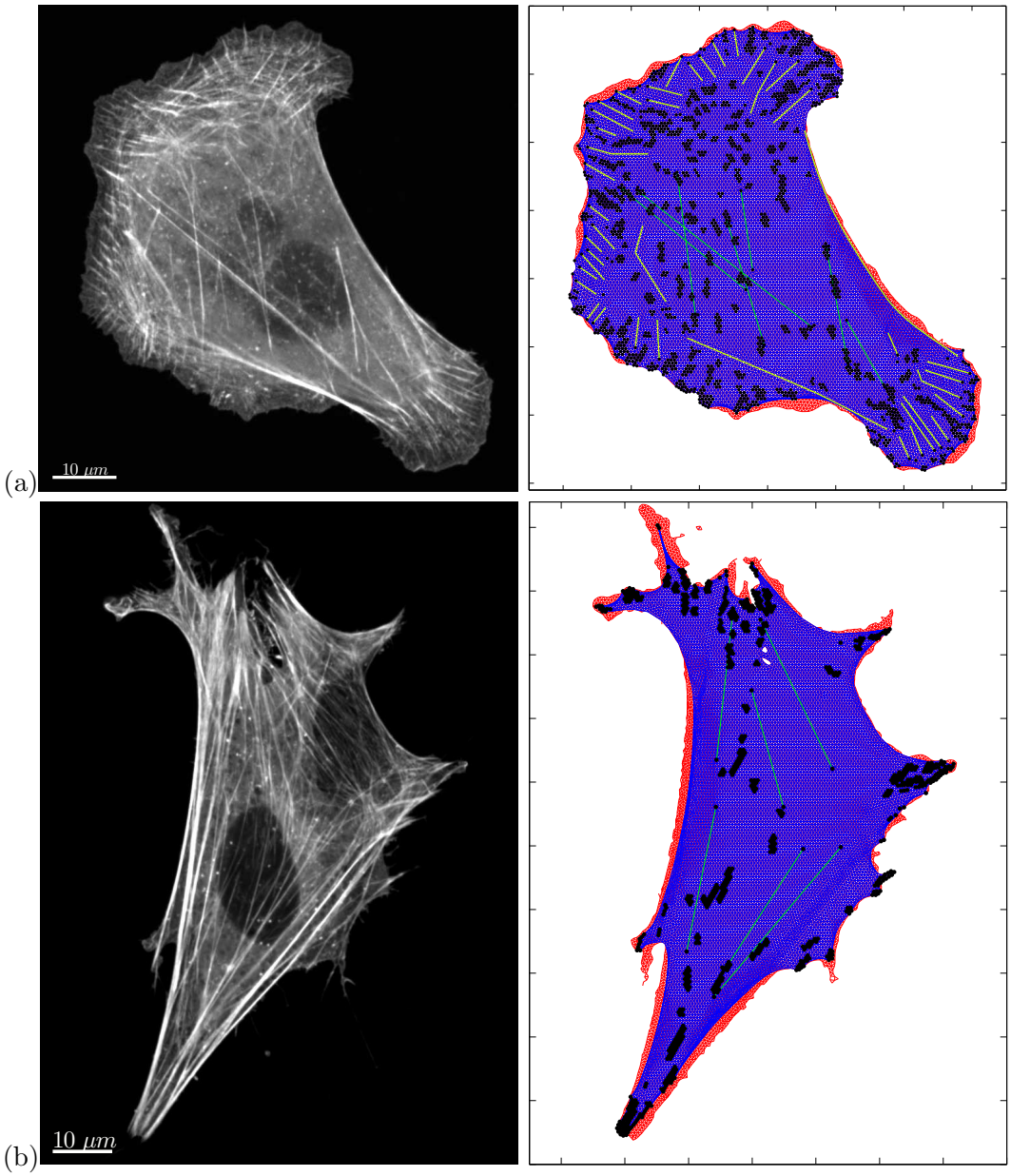

Figure 4.3: Cell shape of 3T3 and U2OS cells. Actin-stained images of a human osteosarcoma (U2OS) cell (a) and a 3T3 mouse fibroblast (b). The setting is the same as in Fig. 4.1 but we model stress fibers differently here. DSFs and TVAs are shown in yellow and ventral stress fibers in green (Only in (a), in (b) DSFs and TVAs are not highlighted.). We use $\tau_d = \tau_t = 0.003$, $\tau_v = \tau = 10^{-5}$, and $\bar{\ell} = 5\ px$ for (a) and $\tau_d = \tau_t = 0.02$, $\tau_v = 10^{-4}$, $\tau = 10^{-5}$, and $\bar{\ell} = 5\ px$ for (b). The length of the bar is 10 μm.

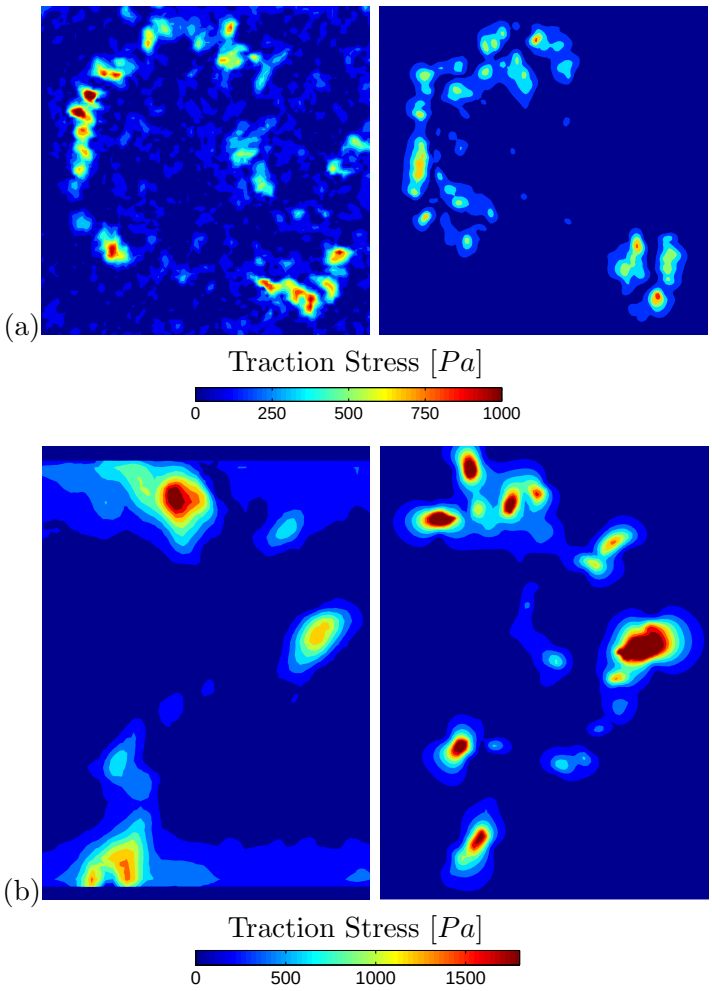

Figure 4.4: Magnitude of the traction stress applied by 3T3 and U2OS cells, for the cells from Fig. 4.3(a) and (b). The experimental result is shown on the left while its corresponding simulation result we depict on the right.

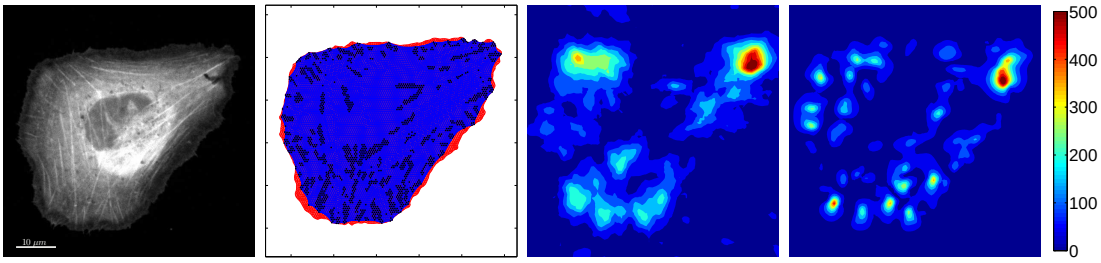

Figure 4.5: Cell shape and traction stress magnitudes of an mDia inhibited U2OS cell. From left to right: Actin-stained image, equilibrium state from network model, experimentally obtained traction stress, traction stress calculated from simulation results. Parameters are those from Fig. 4.3(a). Traction stress is given by a heatmap and in Pa. The length of the bar is 10 μm.

Fig. 4.6(a) and (b) show cell shape and traction stress magnitude for U2OS cells treated with 2 μM and 10 μM, respectively. These cells have more TVAs than U2OS in WT and tend to quite round contours. With increasing Y-27632 concentration traction stresses strongly decrease. The maximum traction stress is several hundreds of Pa without inhibition, and only up to 200 Pa for 2 μM and 50 Pa for 10 μM of y-27632. A maximum traction stress of 50 Pa is obviously already in the regime where thermal fluctuation disturb the measurement of the displacement fields. So the experimentally obtained traction stress distribution has to be interpreted in a more quantitative way.

We analyzed 8 U2OS cells treated with Y-27632 in total (besides 5 U2OS cells without Y-27632). 3 cells for 2 μM, 2 cells for 5 μM and 3 cells for 10 μM. To test whether motor tension is affected by myosin II inhibitor concentration or not, we varied the same parameters for all 8 cells, see appendix B.4 for details. We see that τ_d decreases for increasing inhibitor concentration. This function is shown in Fig. 4.6(c).

4.5 Summary

In this chapter we modeled real cells with the active cable model. Input is generated by segmentation of actin- and paxillin-stained cell images and triangulation. Madin-Darby canine kidney (MDCK) cells, which do not exhibit actin stress fibers, are sufficiently described by the motor force density of network links τ. This does not hold for mouse 3T3 fibroblasts and human osteosarcoma (U2OS) cells. Since the actin cytoskeleton of these cells includes many distinct stress fibers, these must be taken into account explicitly.

We therefore have 4 different motor force densities for the different network links. Simple network links have motor force density τ, transverse arcs (TVAs) have τ_t, dorsal stress fibers (DSFs) τ_d, and ventral stress fibers (VSFs) τ_v. DSFs and TVAs are modeled as serial links integrated into the network, i.e. have the same mean link length as normal network links. In contrast, VSFs are long connections of two focal adhesions (FAs) at the bottom of the cell and therefore are not integrated into the network. We found

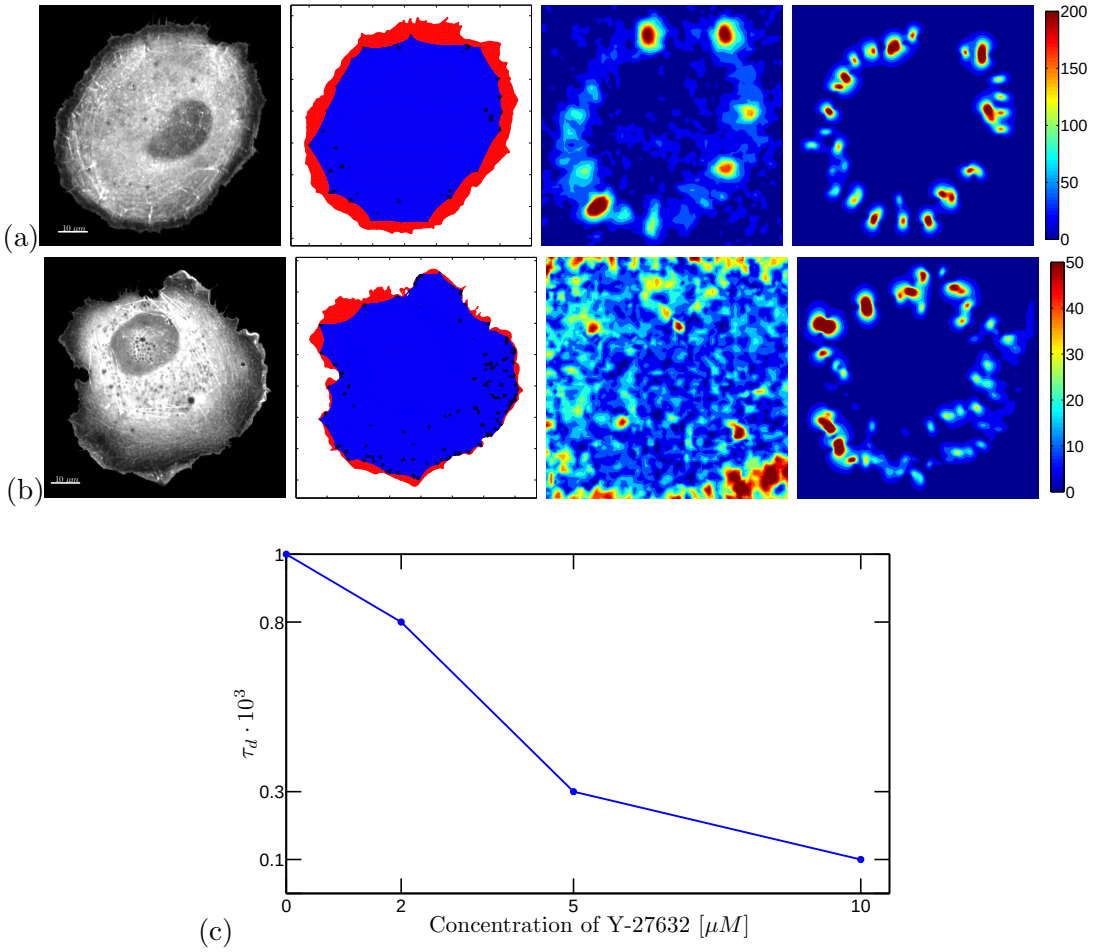

Figure 4.6: U2OS Cells treated with Y-27632. (a) 2 μM Y-27632. (b) 10 μM Y-27632. Cell shape and traction stress magnitudes. From left to right: Actin-stained image, equilibrium state from network model, experimentally obtained traction stress, traction stress calculated from simulation results. We use $\tau_d = 8 \times 10^{-4}$ in (a) and $\tau_d = 10^{-4}$ in (b). The remaining parameters are: $\tau_t = 10^{-4}$, $\tau_v = \tau = 10^{-6}$, $\bar{\ell} = 5\ px$. (c) Motor force density in dorsal stress fibers as function of the concentration of Y-27632 present in cells. For (a) and (b): Traction stress is given by a heatmap and in Pa. The length of the bar is 10 μm.

that τ_d and τ_t must be of the same magnitude. Both must be at least two orders of magnitude larger than τ and τ_v. Then the cell shapes and traction stress distributions give good agreement between simulation and experiment.

We used a FEM model of the substrate to compute its deformation from the traction force field. That way we put the simulation results on the same level as the experimental results. We hope that in future work this procedure can help to define the noise level in the traction stress distributions. If the simulation is done in a proper way, the difference between simulation result and experimental result must be due to noise.

We found that all simulated (wild type) cells of the same type fit best to the experimental results if the same set of parameters is used. Hence, with the ACN model including stress fibers we can calculate traction forces of adherent cells by the knowledge only of shape, stress fiber distribution, and FA distribution. We found that τ_d and τ_t are 10 times higher for 3T3 fibroblasts than for U2OS cells.

We also analyzed cells under different conditions, i.e. after several inhibitors have been added. mDia is important for stress fiber formation. If it is inhibited less stress fibers are formed. However, the optimal motor tension parameters stay approximately the same. That is, the inhibitor lets existing stress fibers unaffected. This picture changes if myosin II inhibitor Y-27632 is added to U2OS cells. Y-27632 decreases motor force density in DSFs.

5

Rupture Dynamics of Cytoskeletal Networks

In contrast to the previous chapters, now the bond networks are used to study rupture dynamics. We assume stochastic rupture of bonds according to the Bell equation. This approach differs from the threshold-based network models of fracture commonly used. We study the statistical properties of stochastically rupturing bond networks and compare them to those of threshold-based models. First we discuss constantly strained networks and in the second part we extend the model to include strain which increases linearly in time. In analogy to chapter 3 we use networks of square external shape. We find that for fast increasing strain, stochastic bond rupture and threshold-based bond rupture give similar results.

5.1 Constant Displacement

5.1.1 Average Network Lifetime without Strain

We start the analysis with the triangular network topology T1 and without rebinding. That is, in case of vanishing prestrain, $e = 0$, we simply study bond percolation on a triangular lattice. Thus, using results from percolation theory we can calculate the average network lifetime analytically.

The bond percolation threshold for the triangular network is well known to be $p_t = 2\sin(\pi/18) \approx 0.3473$ [127], i.e. equally distributed removal of on average $\sim 65\%$ of the bonds of a network with zero prestrain leads to failure for the first time. The total number of bonds of that network be N_{tb}. Without prestrain the rupture rate is constant, $a_i = 1$ for all bonds $1 \leq i \leq N_{tb}$. Furthermore, all rupture events are independent of each other. Therefore the rates simply add up, i.e. initially we have a rate $a = \sum_{i=1}^{N_{tb}} a_i = N_{tb}$ for the first bond of the network to break. The average waiting time for the first rupture event is then given by $t_0 = 1/N_{tb}$. The second bond breaks

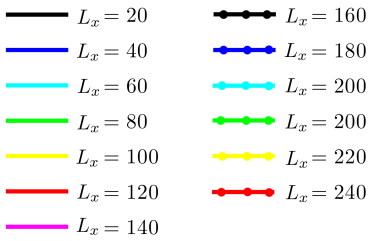

Figure 5.1: Definition of line colors used for figures which show the results for several network sizes.

after another waiting time $t_1 = 1/(N_{tb} - 1)$ and so on. This gives for the lifetime of the network in total

$$T = \sum_{i=0}^{(1-p_t)N_{tb}-1} \frac{1}{N_{tb} - i}, \tag{5.1}$$

since the network on average loses bond percolation after removal of a fraction of $1 - p_t$ of the initial bonds. Eq. (5.1) can be written as:

$$\begin{aligned} T &= \sum_{i=p_t N_{tb}+1}^{N_{tb}} \frac{1}{i} = \sum_{i=1}^{N_{tb}} \frac{1}{i} - \sum_{i=1}^{p_t N_{tb}} \frac{1}{i} \\ &= \ln(N_{tb}) - \ln(p_t N_{tb}) + \mathcal{O}(\frac{1}{N_{tb}}) \\ &\xrightarrow[N_{tb}\to\infty]{} -\ln(p_t). \end{aligned} \tag{5.2}$$

In the third step we have used the logarithmic approximation to the harmonic series. For $p_t = 2\sin(\pi/18)$ we get $T \approx 1.06$ for the average lifetime of the T1 network.

5.1.2 Probability of Failure

In the following we present the results from numerical calculations. We discuss the average behavior of bond networks which are subject to strain. Hereby, we do not only vary strain but also system size N_{tb}. For easier comparability we show the averaged results for the different system sizes in one single figure. Different colors and line-styles are used for the different system sizes. Unless otherwise stated we use the color code defined in Fig. 5.1.

Note, we use the Gillespie algorithm in this section. Nevertheless, for the statistics we note percolation state and number of broken bonds at discrete time steps.

We start the discussion with the probability p_F of network failure. During the simulation of a clamped network at discrete time steps we checked the network for percolation. If it percolates, the probability of failure $p_F(t)$ is set to 0, if it does not, $p_F(t)$ is set to 1. The average over many samples then gives a smooth curve.

In Fig. 5.2(a) we show the results for the average failure probability $p_F(t)$. p_F monotonously increases in time. If network size is increased, this 'anti-percolation transition' becomes sharper, see Fig. 5.2(a) top. We also observe a point symmetry about $(1.06, 0.5)$ if $e = 0$, which is independent of system size. That is, all networks fail on average at the same time. Application of strain $e > 0$ changes this behavior.

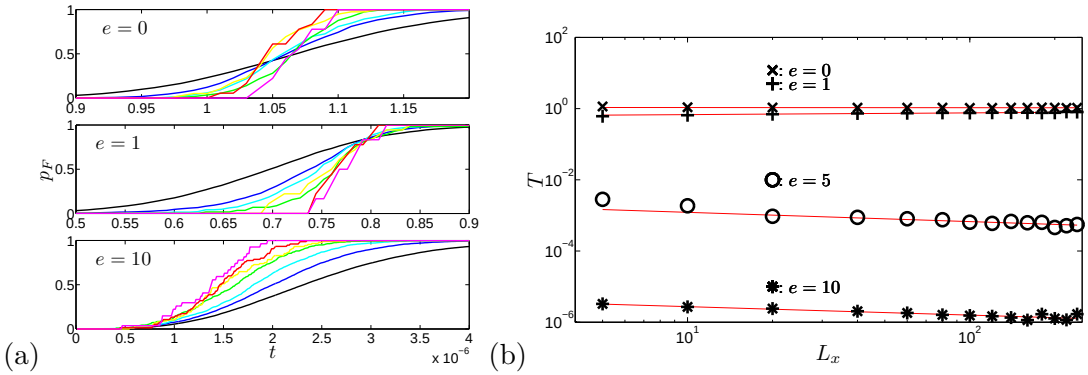

Figure 5.2: Probability of network failure and average network lifetime. (a) The probability p_F for a network subject to prestrain e to lose percolation vs. simulation time t. The steepness of the curves increases with system size. (b) Scaling of the mean network lifetime. Symbols show simulation results for the network lifetime T plotted vs. side length L_x, lines give power law fits $T = bL_x^a$.

For $e = 1$ the jump in the probability of failure is shifted to longer times if system size is increased, Fig. 5.2(a) middle. Interestingly, for $e = 10$ the opposite happens, see Fig. 5.2(a) bottom.

All functions $p_F(t)$ shown in Fig. 5.2(a) appear to be approximately point symmetric about a point with $p_F \approx 0.5$. Thus, the average lifetime T can be found via $p_F(T) \approx 0.5$. For $e = 0$ we find $T \approx 1.06$, independent of system size. So we have reproduced the analytical result, Eq. (5.2). In Fig. 5.2(b) we show the average lifetimes as function of the side length L_x of the network. T exhibits a power law scaling. For $e = 0$ the scaling exponent is zero. For small strain ($e = 1$) it is larger than zero but very small, i.e. the mean lifetime slowly increases with system size. For $e \geq 5$ we find a slow decrease of the network's mean lifetime if the network size is increased. The fit parameters are discussed below in more detail.

5.1.3 Broken Bond Distribution

Next we analyze the number of broken bonds $N_{bb}(t)$, which in the absence of rebinding monotonously increases up to failure. Without prestrain, the relative number of broken bonds $N_{bb}(t)/N_{tb}$ increases up to approximately 0.65, the anti-percolation threshold, see Fig. 5.3(a) top. If prestrain is increased, the fatal fraction of broken bonds drops below 0.65. This happens because of the spatial arrangement of bonds. Bond rupture is biased by the forces in these bonds, i.e. the breaking of fewer "stabilizing" bonds (= bonds under high force) leads to global system failure. If strain is small enough ($e \leq 1$), Fig. 5.3(a) top and middle, the curves of all network sizes collapse to one master curve. As shown in Fig. 5.3(a) bottom, the distributions of broken bonds of systems under large strains do not collapse. The larger the system the sooner it fails and the smaller is the fraction of broken bonds at failure. Interestingly, after a short non-linear transient,

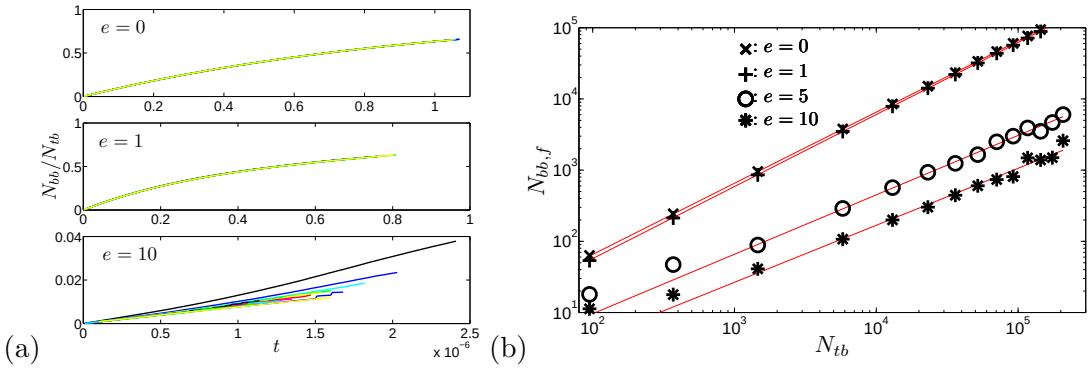

Figure 5.3: Number of broken bonds in the system. (a) Time evolution of the relative number of broken bonds N_{bb}/N_{tb}. For (a) bottom: Lifetime decreases with system time. (b) Scaling of the mean number of broken bonds at failure $N_{bb,f}$ vs. the number of total bonds N_{tb}. Symbols: simulation results, lines: power law fits of $N_{bb,f} = bN_{tb}^{a}$.

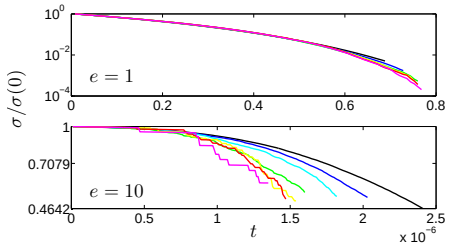

Figure 5.4: Time evolution of the normalized stress in the system. Stress σ is defined as the force the network applies to one clamped side divided by side length L_y. For the bottom figure: Lifetime decreases with system time.

N_{bb}/N_{tb} seems to increase linearly in time. In reality we have a saturating curve. We find this independent of prestrain and system size.

The average number of broken bonds at failure $N_{bb,f}$ scales like a power law for increasing network size N_{tb}, compare Fig. 5.3(b). The scaling exponent is smaller than 1 and decreases with the applied strain.

5.1.4 Evolution of Network Stress

Next we discuss the stress σ the network applies to its clamped sides. In Fig. 5.4 we plot the normalized stress vs. time for different network sizes and strains. In case of no strain we get $\sigma \equiv 0$ for all times (trivial, therefore not shown). Increase of prestrain leads to a monotonously decreasing stress up to failure. At the beginning of the simulation, relative stress is identical for all network sizes and quickly decreasing. Before failure is reached, decrease is exponentially. For very large networks there are two distinct regimes: almost constant stress followed by exponential decay. Furthermore, with

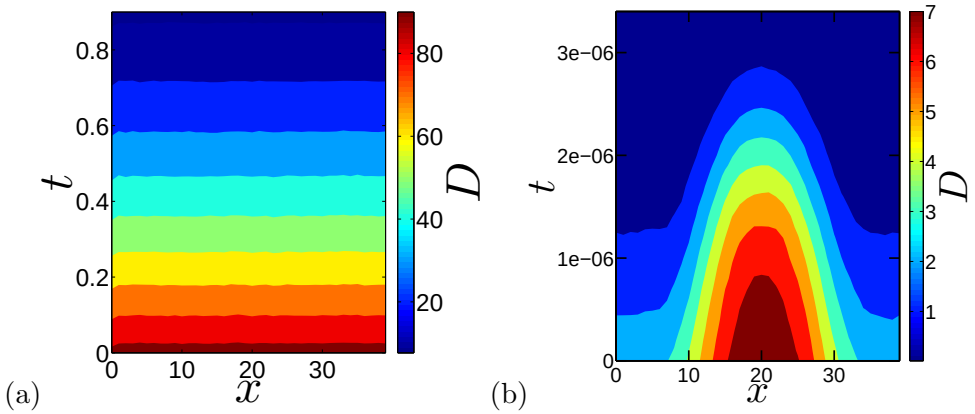

Figure 5.5: Damage density. Colors give the number of bonds at a given x-position which break from a given time point t up to failure. Parameters: $L_x = 40$, $e = 0$ (left), $e = 10$ (right).

increasing prestrain, the curve splits up for the different network sizes. The larger the network the faster the stress decreases.

5.1.5 Fracture Localization

As mentioned before when discussing the differences between Fig. 5.3(a) top and middle, with increasing $e > 0$ the stability of the network is not sufficiently described by the number of bonds which are broken, in contrast to the case of parallel bonds [95]. In [95] the cluster fails if and only if all bonds are broken. The crucial question here is the one of fracture localization, which has been addressed before by a large fracture community, see e.g. [84, 88]. We will also use this concept in the case of linear displacement.

The interesting quantity is the damage density D. To obtain D the bottom line of the network (without strain) is subdivided into bins of equal size. For each bin every broken bond, whose center of mass has its x-component in this bin, is counted. This function is called the damage profile [88]. Because fracture can happen everywhere along the x-axis, the average over lots of samples would be flat. Therefore, we align the damage profiles by their centers of mass before averaging [88]. Since we are interested in the behavior of the system during time, we add all the damage profiles after a given time point t, i.e. we get as damage density $D(x,t)$ a function of two variables, time t and coordinate x.

For vanishing strain the damage density is independent of x and monotonously decreases in time, see Fig. 5.5 (left), i.e. the network diffusely dissolves with many small isolated cracks, since rupture of one bond does not correlate with rupture of its neighboring bonds. For large prestrain damage density becomes a sharply peaked function of x, compare the damage density for $e = 10$ which we show in Fig. 5.5 (right). That is, damage is clearly localized. In this case one big master crack is built, which expands and subsequently leads to network failure.

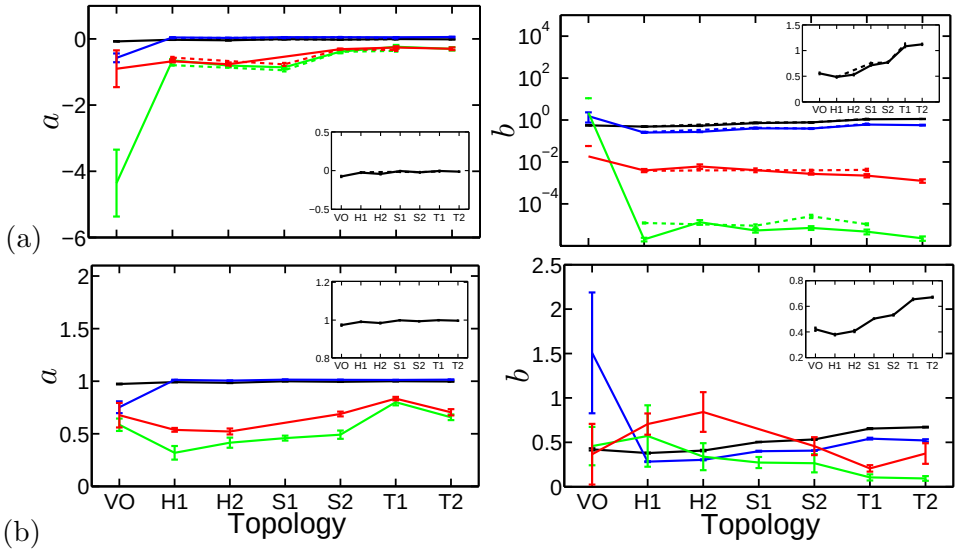

Figure 5.6: Fit parameters a (left) and b (right) vs. topology. (a) Parameters from "Lifetime T vs. side length L_x" (Fig. 5.2(b)). (b) Parameters from "Number of broken bonds at failure $N_{bb,f}$ vs. total bond number N_{tb}" (Fig. 5.3(b)). Prestrain values are: $e = 0$, 1, 5, 10 (indicated by colors black, blue, green, and red). Solid lines are for FBC, dashed lines are for PBC. In the insets we show the parameters for $e = 0$ again. Vertical lines are error bars. The lower end of $e = 5$ and $e = 10$ in (b) right cannot be seen due to the logarithmic scale.

5.1.6 Influence of Topology, Predamage, and Link Mechanics

Next we analyzed if the coordination number (the number of bonds which end at one internal node) has an influence on the properties of the bond network which were discussed above. Therefore we performed the same calculations with the other topologies VO, H1, H2, S1, S2, and T2, see Fig. 2.2(c), as well. To avoid redundancy we do not show Figs. 5.2-5.5 again for the different topologies. All network topologies behave very similar. In particular, all network topologies exhibit the power law scaling of the statistical properties. Let us first discuss the regular topologies and shift the discussion of the VO network to the end.

The interesting quantities are the fit parameters, i.e. a and b from $T = bL_x^a$, Fig. 5.2(b), and $N_{bb,f} = bN_{tb}^a$, Fig. 5.3(b). These are plotted in Fig. 5.6. Here the horizontal axis is the topology axis. For small prestrain $e = 0$, 1 we get $a \approx 0$, see Fig. 5.6(a) left, i.e. the average lifetime of the network is independent of the total number of bonds in the system, independent of topology. However, the proportional-

ity factor b is topology dependent, Fig. 5.6 (a) right. For $e = 0$, b can be calculated analytically by insertion into Eq. (5.2). The results are

$$b(\mathrm{H1}) = b(\mathrm{H2}) = -\ln(1 - 2\sin(\pi/18)) \approx 0.43, \tag{5.3}$$

$$b(\mathrm{S1}) = b(\mathrm{S2}) = \ln(2) \approx 0.69, \tag{5.4}$$

$$b(\mathrm{T1}) = b(\mathrm{T2}) = -\ln(2\sin(\pi/18)) \approx 1.06. \tag{5.5}$$

Here we use the percolation thresholds from the literature [127, 128]. These results are reproduced quantitatively by the simulations, see inset of Fig. 5.6(a) right.

If strain is increased to $e = 10$, b drops down 5 orders of magnitude but still is roughly independent of topology. This does not hold for the exponent a which is negative for large e. The higher the coordination number, the larger the network lifetime, see Fig. 5.6(a).

The number of broken bonds scales linear with system size if strain is small because we have the scaling exponent $a = 1$, see Fig. 5.6(b) left. For vanishing strain in this case we analytically get $a \approx 1$ and for b the well known anti-percolation thresholds:

$$b(\mathrm{H1}) = b(\mathrm{H2}) = 2\sin(\pi/18) \approx 0.35, \tag{5.6}$$

$$b(\mathrm{S1}) = b(\mathrm{S2}) = 0.5, \tag{5.7}$$

$$b(\mathrm{T1}) = b(\mathrm{T2}) = 1 - 2\sin(\pi/18) \approx 0.65. \tag{5.8}$$

These nicely fit to the numerical results, see inset of Fig. 5.6(b) right. For large prestrain ($e = 10$) a becomes topology dependent, increasing with coordination number. The fit parameter b becomes very sensitive to numerical inaccuracy, if prestrain is very large.

Since the mean coordination number of the Voronoi construction is approximately 3, in Fig. 5.6 we plot the results for VO left from the H1 network. For $e \leq 5$ the VO network behaves very similar to its regular counterparts. Only for very large prestrain lifetime decrease with system size is much faster than for the regular networks, see Fig. 5.6. And there are more broken bonds necessary to destroy the network. That is, the regular lattice topology weakens the network of bio-molecular bonds.

For small prestrain $e \leq 1$ predamage does not influence the rupture behavior of the network. All fit parameters change only marginally, see Fig. 5.7. This does no longer hold for large prestrain $e \geq 5$. In this case random bond removal and cuts parallel to strain do not alter the rupture behavior, too. As soon as the cut has a non-zero y-component, the scaling exponents for both, lifetime and number of broken bonds at failure, are drastically reduced. For large network sizes this is no longer balanced by the increase in the associated parameter b. We see that lifetime is significantly reduced several orders of magnitude, and far fewer bonds are necessary for failure, i.e. we observe strong correlations of rupturing bonds. This shows that opposite to small strain a predamage at large strain will grow further and finally lead to network failure.

If we replace the Hookean spring network by a passive cable network, the results do not change (data not shown), since most of the bonds are tensed. Therefore it is

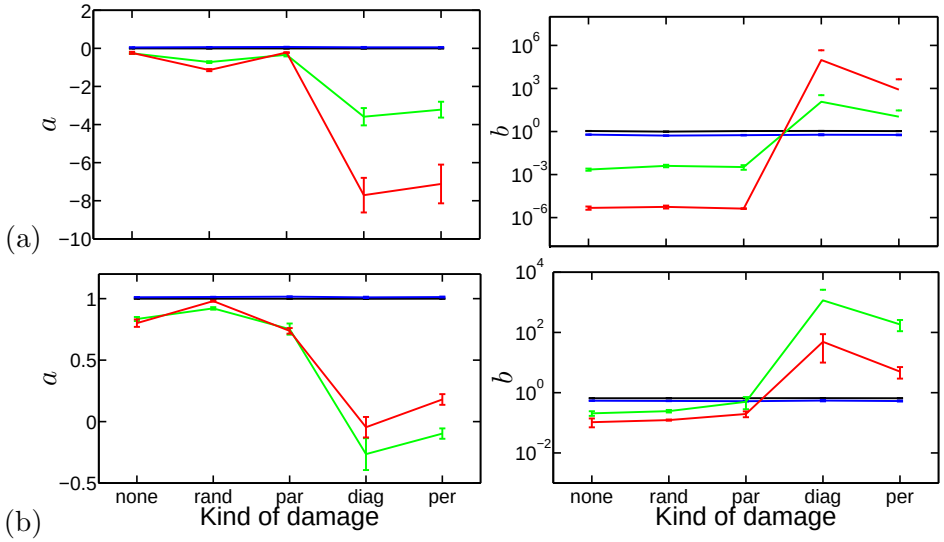

Figure 5.7: Fit parameters a (left) and b (right) vs. kind of predamage. (a) Parameters from "Lifetime T vs. side length L_x" (Fig. 5.2(b)). (b) Parameters from "Number of broken bonds at failure $N_{bb,f}$ vs. total bond number N_{tb}" (Fig. 5.3(a)). Prestrain values are: $e = 0$, 1, 5, 10 (indicated by colors black, blue, green, and red). Solid lines are for FBC, dashed lines are for PBC. Vertical lines are error bars. The lower end of $e = 5$ and $e = 10$ in (a,b) right cannot be seen due to the logarithmic scale.

more interesting to study the active cable network. Of course we expect the differences to the spring network to be marginal if prestrain is large, since then elastic forces will dominate the contractile motor forces. This expectation appears to be true, compare Fig. 5.8. For vanishing prestrain the scaling exponent a has values -0.02 and -0.117 for $\tau = 0.1$ and $\tau = 1$. b drops down to 0.451 for $\tau = 1$. Indeed, there is a strong decrease of lifetime with motor force. The mean number of broken bonds at failure stays approximately constant for $\tau \leq 0.1$. For $\tau = 1$ fewer bonds break up to failure.

5.1.7 Short Comment on Rebinding

For vanishing prestrain all the rupture rates are given by $\rho = \exp(0) = 1$, which is constant over the whole simulation. Hence, the minimal rebinding rate to avoid network failure is given by $\gamma = 1$. We hereby assume that the network has infinite memory. Fig. 5.8 shows the time evolution of the fraction of broken bonds for a small network with side length $L_x = 20$ and for different rebinding rates γ. For $\gamma = 0$ we obtain the same curve as shown in Fig. 5.3, i.e. increase up to $N_{bb}/N_{tb} \approx 0.65$ at $t \approx 1.06$. $\gamma > 0$ increases the lifetime of the network. When it approaches 1, the network gets stabilized. First, the curves are equal, but then split up towards longer lifetimes. For $\gamma = 0.8$ the network lifetime increases an order of magnitude. The network seems to have stabilized but then it abruptly fails. The fatal fraction of broken bonds is ~ 0.55

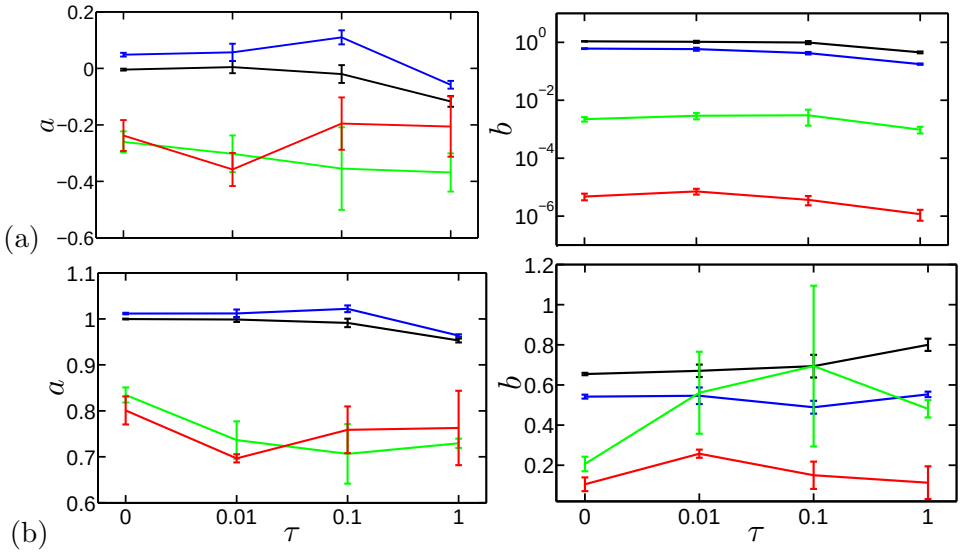

Figure 5.8: Fit parameters a (left) and b (right) vs. motor force. (a) Parameters from "Lifetime T vs. side length L_x" (Fig. 5.2(b)). (b) Parameters from "Number of broken bonds at failure $N_{bb,f}$ vs. total bond number N_{tb}" (Fig. 5.3(a)). Prestrain values are: $e = 0$, 1, 5, 10 (indicated by colors black, blue, green, and red). Solid lines are for FBC, dashed lines are for PBC. Vertical lines are error bars.

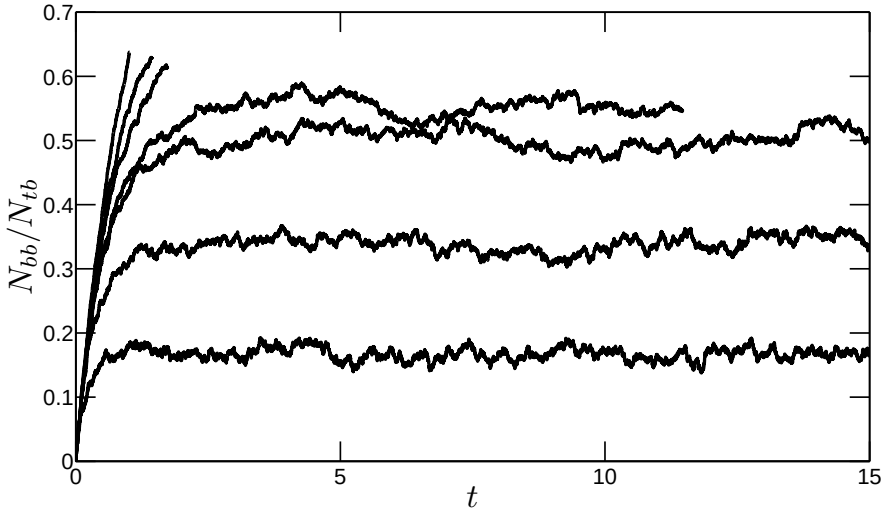

Figure 5.9: Time evolution of the relative number of broken bonds N_{bb}/N_{tb} with rebinding for one sample. Parameters are: $L_x = 20$, $e = 0$, $\gamma = 0$, 0.3, 0.5, 0.8, 1, 2, 3 (from top to bottom).

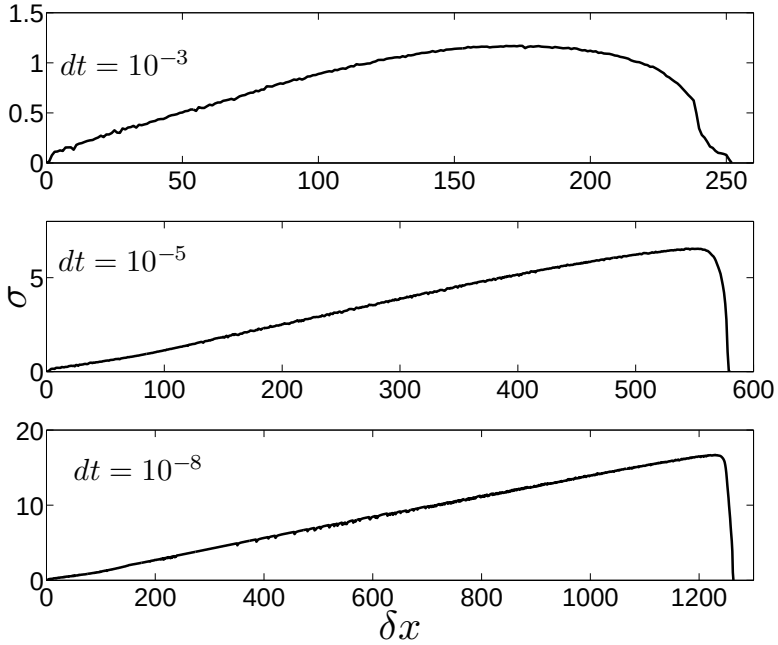

Figure 5.10: Stress-extension curve of a typical sample. Stress $\sigma = F/L_y$ is plotted vs. the displacement δx of the network's clamped sides. F is the force the network applies to one of its clamped sides. Parameters: $L_x = 240$, $L_y = 144 \cdot \sqrt{3}$, $i = 12$. Free boundary conditions.

and therefore smaller than the anti-percolation threshold. In the case of $\gamma = 1$ the curve jumps up to ~ 0.5 and stays approximately at this value. Further increase of the rebinding rate γ to 2 and 3 leads to network stabilization at fewer broken bonds.

Although rebinding can avoid failure of the unstrained network and maybe only little strained ones ($e \leq 1$), it only delays failure for largely strained networks. Rebinding closes small cracks but cannot avoid the fatal crack as soon as it is big enough (data not shown). This general problem also affects increasing strain. Therefore we do not discuss rebinding in the next section.

5.2 Linear Displacement

In this section we analyze a network under linear displacement, i.e. the clamped nodes at the network sides (Fig. 2.3) are not kept fixed during the simulation but pulled apart step-wise. We follow the procedure described in section 2.5.2. That is, pulling speed is given by $v = dx/dt$. A very important aspect of this section is the discussion of the measured quantities in comparison to those from [88], in which the statistical properties of a random spring model (RSM) are studied.

5.2.1 Stress Strain Relation

For illustration purpose in Fig. 5.10 we plot the network stress σ vs. the displacement δx of the network for a typical simulation sample. For low pulling speed we observe initially a linearly increasing stress followed by a broad plateau phase and ended by a rapid decay, Fig. 5.10 (top). For very large speed we get a linear force response up to a distinct maximum with very large curvature followed by an almost vertical force decay, Fig. 5.10 (middle) and (bottom). Since pulling speed is constant during the simulation, the lifetime of the networks is simply $\delta x_f \cdot dt$. Here, δx_f refers to the value of δx at failure. From Fig. 5.10 we therefore see that the faster one pulls the shorter is the network lifetime. But for every dt, there is a maximum in the force-extension curve which increases with pulling speed. Thus, the faster one pulls the more stress the network can bear before failure. The displacement is always applied to both clamped sides simultaneously. Hence, in the words of the previous section, the analyzed example network bears maximum strains 2.11, 4.83, 10.54 (for $dt = 10^{-3}$, 10^{-5}, 10^{-8}) before it fails.

5.2.2 Fracture Localization

With increasing pulling speed, the behavior of the network before and after peak load becomes more and more distinct. This motivates the analysis of the "prepeak regime" (from start to peak load) and the "postpeak regime" (from peak load to failure) [84, 88].

Without rupture, the increase of displacement simply leads to a linear increase of σ. The same happens in the RSM before peak load is reached [88]. After peak load, this network force rapidly decreases to zero (failure). We also get this behavior in the case of high pulling speed Fig. 5.10 (bottom). That is, only few diffusely distributed bonds break in the prepeak regime, weakening the network only marginally. For the RSM holds: If the increase of δx is stopped during the prepeak regime, the network will survive and not fail [88]. In the postpeak regime it will fail anyway. For the network of bio-molecular bonds the network will always fail, because of thermal fluctuations, at least if the rebinding rate is small enough.

Next we discuss the damage density D in these two regimes. To calculate D we proceed as follows. The present situation of the deformed and damaged network is mapped back to the initial undeformed and intact lattice, i.e. while removing (and inserting) bonds in the network under tension the same is done with the initial network [88]. For the RFM both representations are identical.

To define the degree of localization, the x-axis is subdivided into bins of equal size. For each bin every broken bond whose center of mass has its x-component in this bin is counted. Because fracture can happen everywhere along the x-axis, the average over lots of samples would be flat. Therefore, we first align the damage profile by its center of mass [88]. The damage density profile for the prepeak regime is shown in Fig. 5.11(a) while for the postpeak regime we depict it in Fig. 5.11(b). Please note, Fig. 5.11(b) does not show D but ΔD, where the diffusive bottom (D in the prepeak regime) has been subtracted.

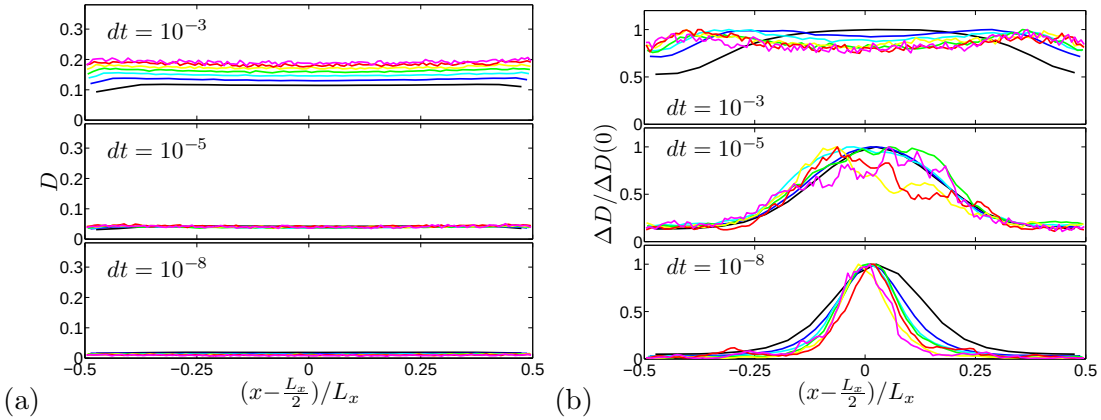

Figure 5.11: Damage profiles of the different regimes in the bond network subject to linear displacement. (a) Prepeak regime. (b) Postpeak regime. Lines show the ratio of broken bonds vs. their x-positions.

In the case of large dt, the difference between prepeak and postpeak regime is very small. Both damage profiles are flat, implying diffusion dominated damage over the whole simulation, Fig. 5.11(a) top, and (b) top. If we pull the network faster, the prepeak damage density drops down, i.e. fewer bonds are broken in the prepeak regime and a clear difference between the two damage profiles arises, Fig. 5.11(b) bottom. Now, in the prepeak regime damage is diffusive, while in the postpeak regime it is clearly localized. This behavior is similar to that of the RSM [88]. The damage profile in the postpeak regime collapses to one master curve with non-exponential tails. Contrary to the RSM, for $dt \geq 10^{-5}$ we get some "background noise" in the postpeak regime, i.e. we always have $\Delta D > 0$. Due to the stochastic bond rupture also less stretched or even force-free bonds can break in the postpeak regime. Background noise vanishes for very fast pulling ($dt = 10^{-8}$).

These results lead to the conclusion that contrary to the RSM the network of molecular bonds for low pulling speed is not destroyed in a fatal avalanche, one crack which grows until it spans over the whole network (up to failure), but by many diffusely distributed and small cracks which weaken and dissolve the material. The accumulation of force on crack tips is not important for fracture in this regime. For fast pulling the bond network acts similar to the RSM.

5.2.3 Broken Bond Distribution

We calculated the probability density function (PDF) for the fraction of broken bonds at peak load N_{bb}/N_{tb}. Unfortunately, many samples are necessary to get a smooth curve, therefore we show the cumulative distribution function (CDF) instead of the PDF, see Fig. 5.12(a). The CDF is obtained from the PDF by summing up all values up to a given one. For all pulling speeds studied there is one distinct jump in the CDF, i.e. a peak in the PDF, for each dt and network size. For $dt = 10^{-3}$ this jump is shifted

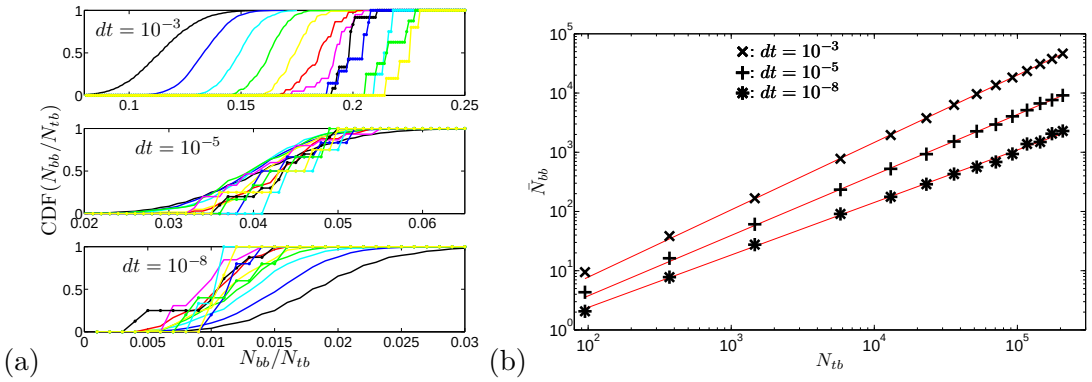

Figure 5.12: Number of broken bonds at peak load. (a) Cumulative distribution of the number of broken bonds at peak load. (b) Scaling of the mean number of broken bonds $\bar{N}_{bb}$ at peak load. Symbols: simulation results, lines: power law fits $\bar{N}_{bb} = bN_{tb}^{a}$.

to larger values if network size is increased. For larger pulling speeds ($dt < 10^{-5}$) the jumps are shifted to lower N_{bb}/N_{tb} for increasing system sizes, Fig. 5.12(a) bottom.

Now we study the broken bond distribution in more detail. Therefore we plot the average $\bar{N}_{bb}$ vs. N_{tb} and fit it by a power law, compare Fig. 5.12(b). For all dt we find a good agreement with the power law behavior. The exponent for $dt = 10^{-3}$ is slightly larger than 1. This might be due to the finite size of the analyzed networks. However, for $dt < 10^{-3}$ the fits give exponents less than 1, i.e. in the limit $N_{tb} \to \infty$ the prepeak regime vanishes. For example at $dt = 10^{-8}$ we get $a = 0.89$, which is the RSM limit of our model, since for the RFM / RSM the exponent is about 0.91 [129] / 0.92 [88]. In the limit of large networks for high pulling speed there are no bonds broken in the prepeak regime. As soon as the first bond breaks, the catastrophe occurs which leads to the rapid force decay and, subsequently, network failure.

5.2.4 Fracture Strength

Fracture strength σ_F is defined as the peak load divided by the clamped side length (L_y). Like the number of broken bonds at peak load N_{bb}, the fracture strength distribution itself is sharply peaked around its maximum, Fig. 5.13(a). In analogy to the distribution of broken bonds at peak load, we show the CDF here instead of the PDF.

If system size is increased, the mean peak load decreases monotonously. But as already mentioned when discussing Fig. 5.10: the faster one pulls the higher is the fracture strength σ_F. Interestingly, if we decrease dt by five orders of magnitude the increase in fracture strength is only one order of magnitude.

In Fig. 5.13(b) we plot the mean fracture strength vs. the network side length. We also did power law fitting here. The fracture strength for the RFM/RSM does not follow a power law. But the peak load vs. network side length shows the scaling law $F_{peak} = C_0 L^{\alpha} + C_1$ [88].

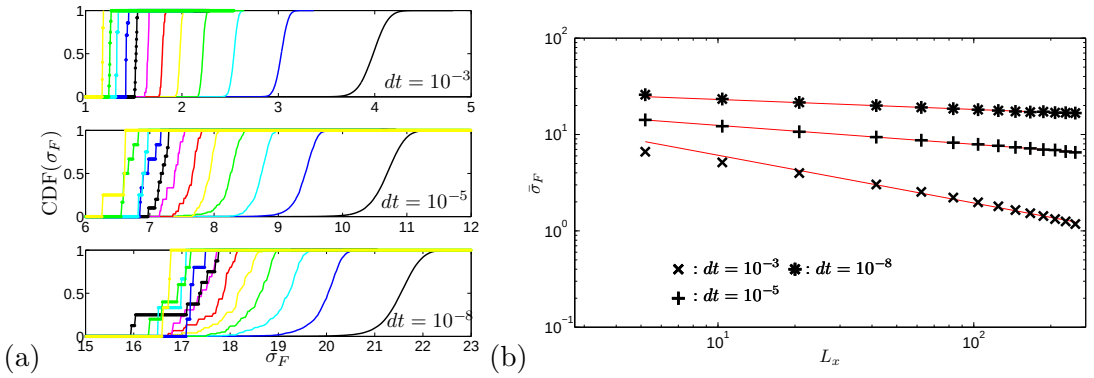

Figure 5.13: Fracture strength. (a) Cumulative fracture strength distribution. (b) Scaling of fracture strength. Mean fracture strength $\bar{\sigma}_F$ as function of network side length. Symbols are simulation results while lines denote power law fits of $\bar{\sigma}_F = bL_x^a$.

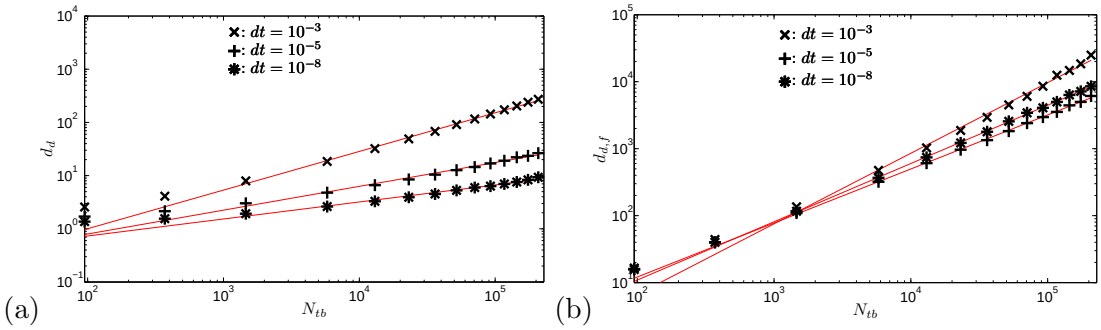

Figure 5.14: Degree of degeneracy d_d. (a) Scaling of the average degree of degeneracy. Average degree of degeneracy without final breaking event vs. total number of bonds. Simulation results are shown as symbols, power law fits $d_d = bN_{tb}{}^a$ as lines. (b) Scaling of the final degree of degeneracy. Size of the last breaking event vs. total bond number. Simulation results are shown as symbols, power law fits $d_{d,f} = bN_{tb}{}^a$ are shown as lines.

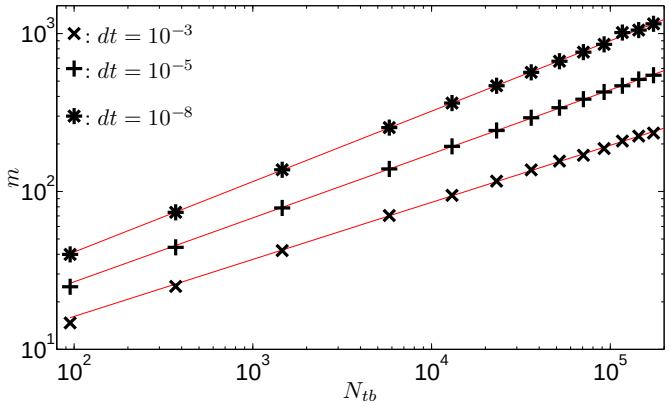

Figure 5.15: Mean number of steps m taken up to failure. Symbols are simulation results while lines denote power law fits of $m = bN_{tb}^a$.

5.2.5 Degeneracy

In the FBM, RFM, and RSM avalanches (bursts in the language of the FBM) are defined as the bonds breaking between two unit displacements. The avalanche size is given by the number of bonds which break during one avalanche. In this thesis we call avalanches the degree of degeneracy d_d because all these bonds break during the same time interval dt and in parallel, not serially.

Similar to the avalanches in the RSM, we expect a very different behavior of the degree of degeneracy before (d_d) and after ($d_{d,f}$) peak load. To calculate d_d we only take into account bond rupture events before peak load. The time between peak load and failure is very short for all pulling speeds, see Fig. 5.10. Therefore, we call the number of bonds which break between peak load and failure the final degree of degeneracy $d_{d,f}$. Fig. 5.14(a) shows the mean degree of degeneracy d_d as function of system size N_{tb}. We find a power law scaling. For $dt = 10^{-3}$ we get $d_d \approx 0.15\%$, for $dt = 10^{-5}$ $d_d \approx 0.01\%$ and for $dt = 10^{-8}$ even on magnitude less. $d_{d,f}$ is several orders of magnitude larger than the average d_d before peak load. It also scales like a power law, Fig. 5.14(b).

In the RSM the final avalanche scales with system size according to a power law with exponent 0.68, [88]. This is far away from the exponents we find for large pulling speeds, namely 0.81 for $dt = 10^{-5}$ and 0.87 for $dt = 10^{-8}$.

For linear displacement lifetime increases with system size, Fig. 5.15. This is not contradictory to the lifetime of constantly displaced networks which decreases with system size, Fig. 5.2(b), because here each displacement is of size 1 and therefore independent of system size. The number of steps m taken up to failure follows a power law, $m = bN_{tb}^a$, with an exponent a independent of dt. But b increases with pulling speed and so does m.

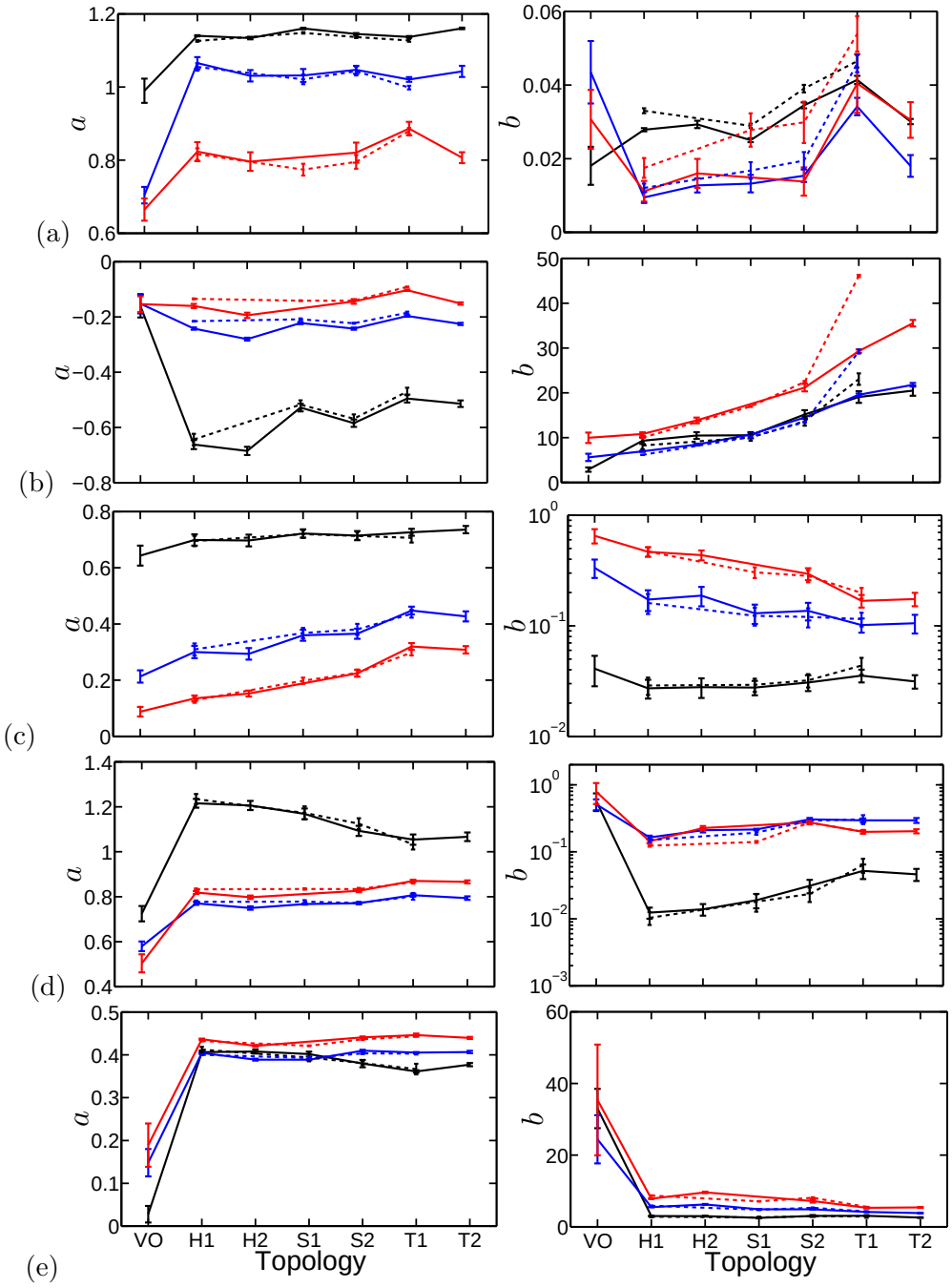

Figure 5.16: Fit parameters a and b vs. topology. (a) Broken bonds at peak load vs. total number of bonds. (b) Peak load vs. side length. (c) Average degree of degeneracy vs. total number of bonds. (d) Final degree of degeneracy vs. total number of bonds. (e) Steps to failure vs. total number of bonds. Parameters are: $dt = 10^{-3}, 10^{-5}, 10^{-8}$ (indicated by colors black, blue, and red). Solid lines are for FBC, dashed lines are for PBC. Vertical lines are error bars.

5.2.6 Influence of Predamage, Topology, and Link Mechanics

Analog to the discussion of the constant displacement in the previous section, here we discuss the fit parameters for the different topologies and boundary conditions, which are plotted in Fig. 5.16. Results for FBC and PBC are very similar. For the discussion we restrict ourselves to large networks, i.e. in this case the scaling parameter a is crucial for the statistical properties of the bond networks.

As long as the network is regular, the scaling exponent of the number of broken bonds at peak load does not depend on the network topology, see Fig. 5.16(a) left. For the irregular Voronoi construction a is significantly lower. That is, for irregular networks fewer bonds break before peak load. For $dt = 10^{-3}$ independent of lattice topology a is larger than 1. For $dt = 10^{-5}$ a is approximately 1 and for $dt = 10^{-8}$ a is smaller than 1, independent of lattice topology as long as it is regular.

Fracture strength for irregular networks appears to be independent of pulling speed, Fig. 5.16(b) left. But for the regular lattices fracture strength increases with pulling speed and coordination number. Hence, the triangular networks can bear more stress than the other regular topologies. But for low pulling speeds the irregular networks can bear even more stress ($dt = 10^{-3}$).

The mean degree of degeneracy is constant for $dt = 10^{-3}$, but for smaller dt its scaling exponent increases with coordination number, i.e. during an average time step most bonds break in the triangular networks, Fig. 5.16(c) left. The irregular network has the smallest degree of degeneracy. Also the final degree of degeneracy $d_{d,f}$ is smallest for irregular networks, Fig. 5.16(d) left. For $dt = 10^{-3}$ $d_{d,f}$ decreases with coordination number but its scaling exponent a is always larger than 1. For regular networks with $dt \leq 10^{-5}$ the exponent is constant at $a \approx 0.75$.

The number of elongation steps up to failure is smallest for the irregular networks, compare Fig. 5.16(e) left. Interestingly, for all the regular network topologies the scaling exponent a is independent of pulling speed and topology constant at $a \approx 0.4$. Of course, the prefactor b increases with pulling speed, but as long as regular it is independent of topology, see Fig. 5.16(e) right.

As we can see in Fig. 5.16 the difference between the behavior of networks with FBC and those with PBC is only marginally. But we observe that the corresponding damage profiles in the postpeak regimes do not collapse. For the PBC the tails decrease more rapid, compare the example shown in Fig. 5.17. This means that for PBC the average fatal crack is slightly more pronounced.

In Fig. 5.18 we plot the force-extension curve for a typical T1 network with a cut perpendicular to the applied strain. For slow pulling the force-extension curve appears to be independent of cut size, Fig. 5.18(top). But if pulling is faster we can observe two things. First, peak load decreases and second, the network fails after much less elongation steps. The lower dt the larger the influence of predamage. See in particular Fig. 5.18 (middle). A little orthogonal cut of only 10% of the network's height drastically reduced the dimensionless fracture strength from ~ 6.55 to ~ 3.95, a decrease of approximately 40%. Further increase of cut size leads to further decrease in fracture strength, although less drastic. The same happens for the number of steps up

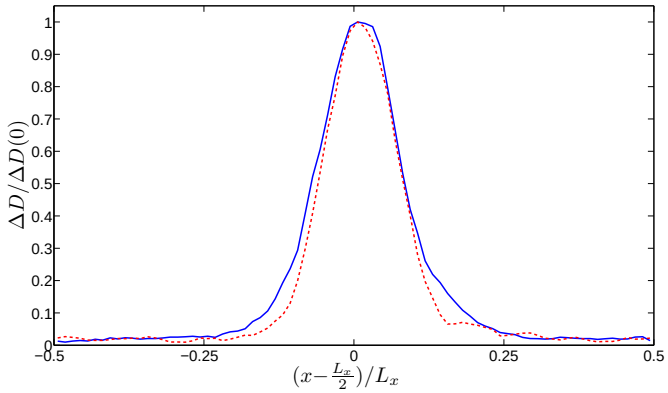

Figure 5.17: Damage profile in the postpeak regime for the different boundary conditions. FBC are shown as solid, PBC as dashed lines. Parameters: T1 network, $L_x = 80$, $dt = 10^{-8}$.

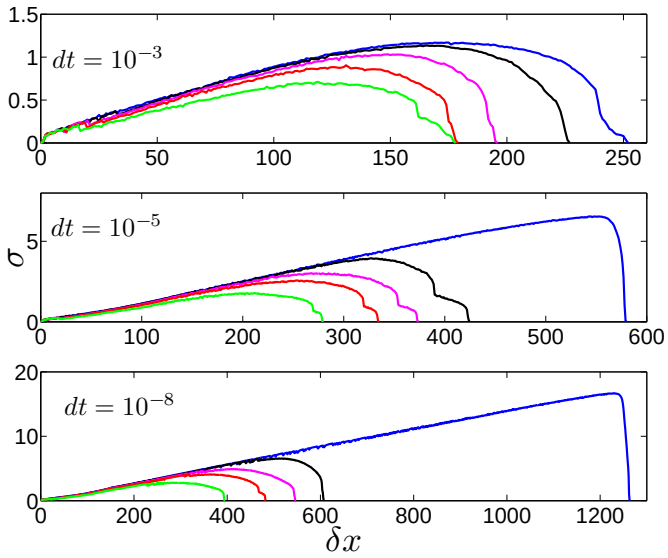

Figure 5.18: Force-extension curve of predamaged networks. Stress $\sigma = F/L_y$ is plotted vs. the displacement δx of the network clamped sides. F is the force the network applies to one of its clamped sides. Parameters are: $L_x = 240$, $L_y = 144 \cdot \sqrt{3}$, $i = 12$ and $p = 0.1$, 0.2, 0.3, 0.5 with decreasing peak load. The central cut is oriented perpendicular to strain.

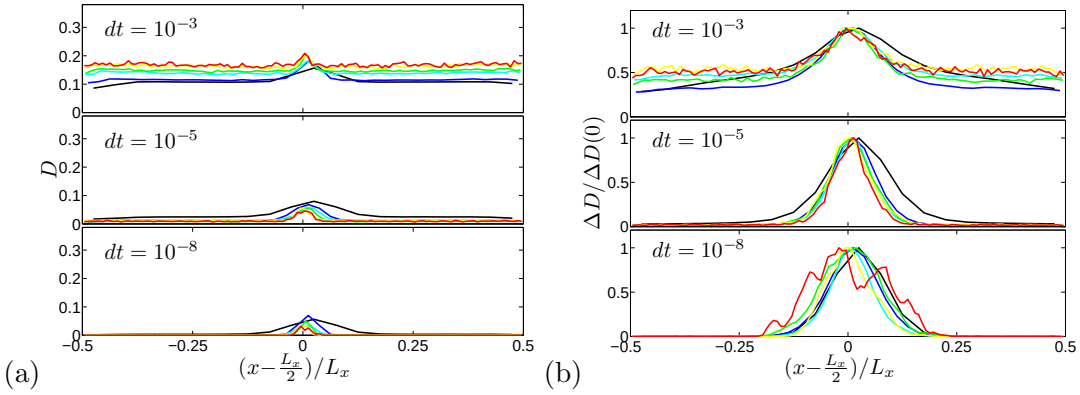

Figure 5.19: Damage profiles of the different regimes in the predamaged network. (a) Prepeak regime. (b) Postpeak regime. Lines show the number of broken bonds vs. their x-positions. Parameters: $p = 0.1$. Central cut is perpendicular to strain.

to failure, a loss from 580 to 425 ($\sim 27\%$). There is a sharp bend in the force-extension curve of predamage networks subject to fast pulling. What happens is the following. The predamage crack grows due to force accumulation at its tip. This leads to two distinct percolation paths from one clamped side to the other, one above the crack and one below it. Breakage of one of these leads to the sharp bent, since for a short time strain can be increased at constant stress.

Comparing Fig. 5.19 to Fig. 5.11 we see that predamage has only little influence on the damage profiles for $dt = 10^{-3}$. The top figures are basically identical, except for the small peak in Fig. 5.19(a) top. This peak is just predamage itself because the damage profile does not fully flatten before peak load. Postpeak there is a flat valley at the location of the crack, Fig. 5.19(b) top. This gives in total a diffusion dominated damage in the predamaged network at low pulling speed. For faster pulling the prepeak behavior is very similar, see a middle. But for very fast pulling there are no bonds broken before peak load. See Fig. 5.19(a) bottom: the peak in the center is only the previously placed crack. For $dt \leq 10^{-3}$ damage is clearly localized in the postpeak regime, see (b) middle and bottom. Without predamage this does not happen, compare Fig. 5.11(b). For $dt = 10^{-3}$ the damage profile is diffusive even in the postpeak regime. For very fast pulling of a predamaged network only bonds in the close vicinity of the crack are broken. This leads to a very narrow peak in the damage profile. Also the background noise observed in Fig. 5.11(b) bottom vanishes.

We also checked the different kinds of predamage in the case of linear displacement. The fit parameters are shown in Fig. 5.20. For random damage and parallel cutting the number of bonds which break up to peak load does not change. But with a cut component in y-direction N_{bb} will decrease an order of magnitude, Fig. 5.20(a). Peak load also decreases only for diagonal and perpendicular cuts, Fig. 5.20(b). The stress accumulation only marginally influences the mean number of bonds which break during

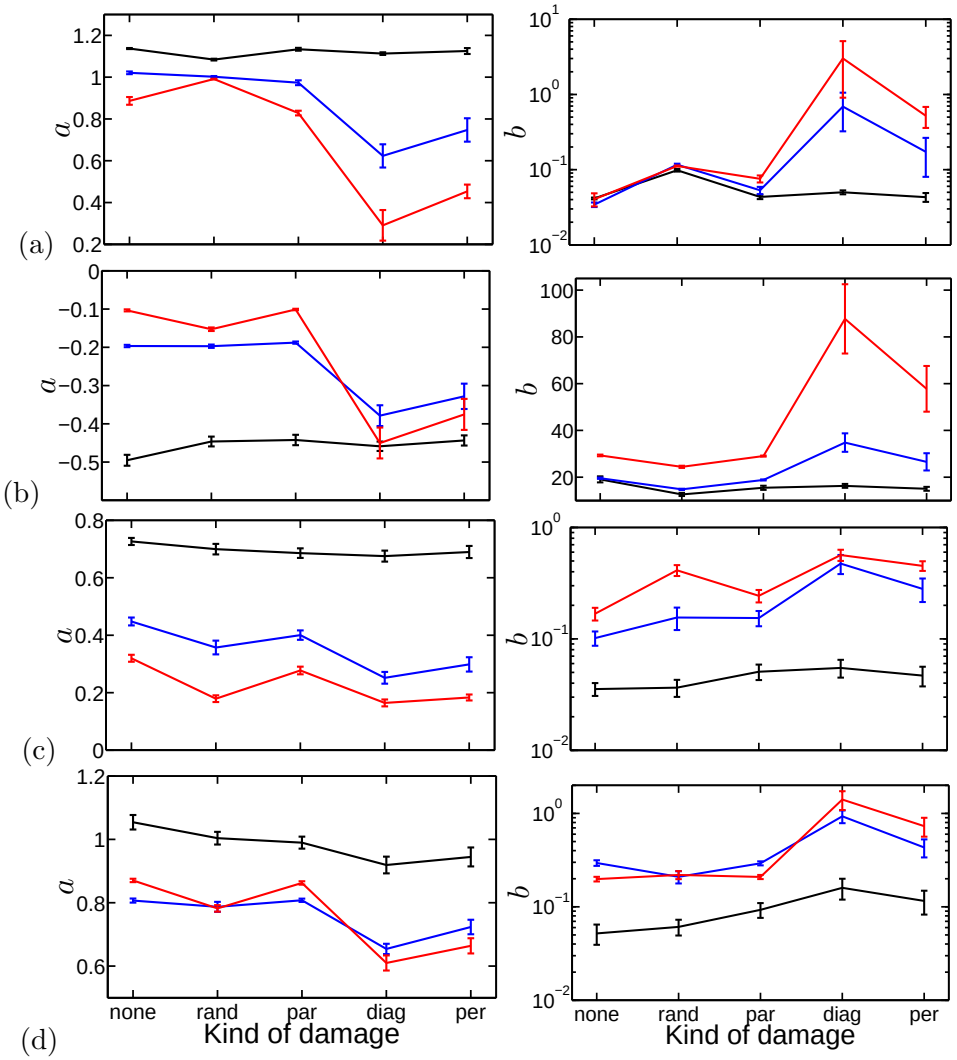

Figure 5.20: Fit parameters a and b vs. kind of predamage. (a) Broken bonds at peak load vs. total number of bonds. (b) Peak load vs. side length. (c) Average degree of degeneracy vs. total number of bonds. (d) Final degree of degeneracy vs. total number of bonds. Parameters are: $dt = 10^{-3}$, 10^{-5}, 10^{-8} (indicated by colors black, blue, and red). Solid lines are for FBC, dashed lines are for PBC. Vertical lines are error bars.

one time step. It tends to decrease, Fig. 5.20(c). The fatal degeneracy also tends to decrease, but not significantly, Fig. 5.20(d).

We also modeled the network bonds as active cables. For fast pulling the results differ only marginally from those obtained with the Hookean spring model. Analog to the discussion of active cables under large constant displacement, we conclude that elastic forces dominate active forces and therefore the active nature of the bonds plays a minor role, see Fig. 5.21.

So far we have discussed the bond network only for $\gamma = 0$. The other extreme rebinding case, $\gamma = \infty$, means that every broken bond will immediately close during the next time step. This will be limited by $\ell_{max} < \infty$, i.e. as soon as crack-size is larger than ℓ_{max} rebinding will be prohibited. After that the network will be destroyed by a single fatal crack.

5.3 Summary

Motivated by fracture processes which appear in several biological systems on sub-, super- and single cellular level, we have studied the statistical properties of failure of networks of bio-molecular bonds under force. Bio-molecular bonds break according to a rate which is proportional to the exponential of the force in the bond. This approach is in stark contrast to that of common bond network models for fracture of hard macroscopic materials. A macroscopic bond breaks if the force it carries exceeds a fixed threshold.

For our simulations we took networks of square shape in which we clamped the peripheral nodes of two opposing sides. We extended the distance between the two clamped sides to apply a strain on the network. Hereby, every movement is modeled as instantaneous, i.e. the network is treated as always in equilibrium. The two opposing non-clamped sides can be allowed to move freely, i.e. free boundary conditions, or as if they were closed and the network would form a cylinder of infinite radius, i.e. periodic boundary conditions.

The two clamped network sides are displaced in two ways. First, we apply a strain and calculate the equilibrium. Now rupture is allowed. This procedure is referred to as the "constant displacement (CD)". The other displacement protocol is pulling the network with a constant speed while it ruptures, the so-called "linear displacement (LD)".

The CD with vanishing strain is identical to a simple percolation investigation of the network. For both, vanishing and non-vanishing strain, we analyzed the time dependence of the number of broken bonds, the failure probability, and the force the network applies to one clamped side. We found that failure probability is very steep, in particular for large networks. In the absence of rebinding the number of broken bonds increases monotonously with time. Close to failure this increase is linear. Stress decreases exponentially when approaching network failure. The statistical properties which we studied in the CD case were the lifetime of the network, which decreases very slowly with system size, and the total number of bonds breaking up to failure, which

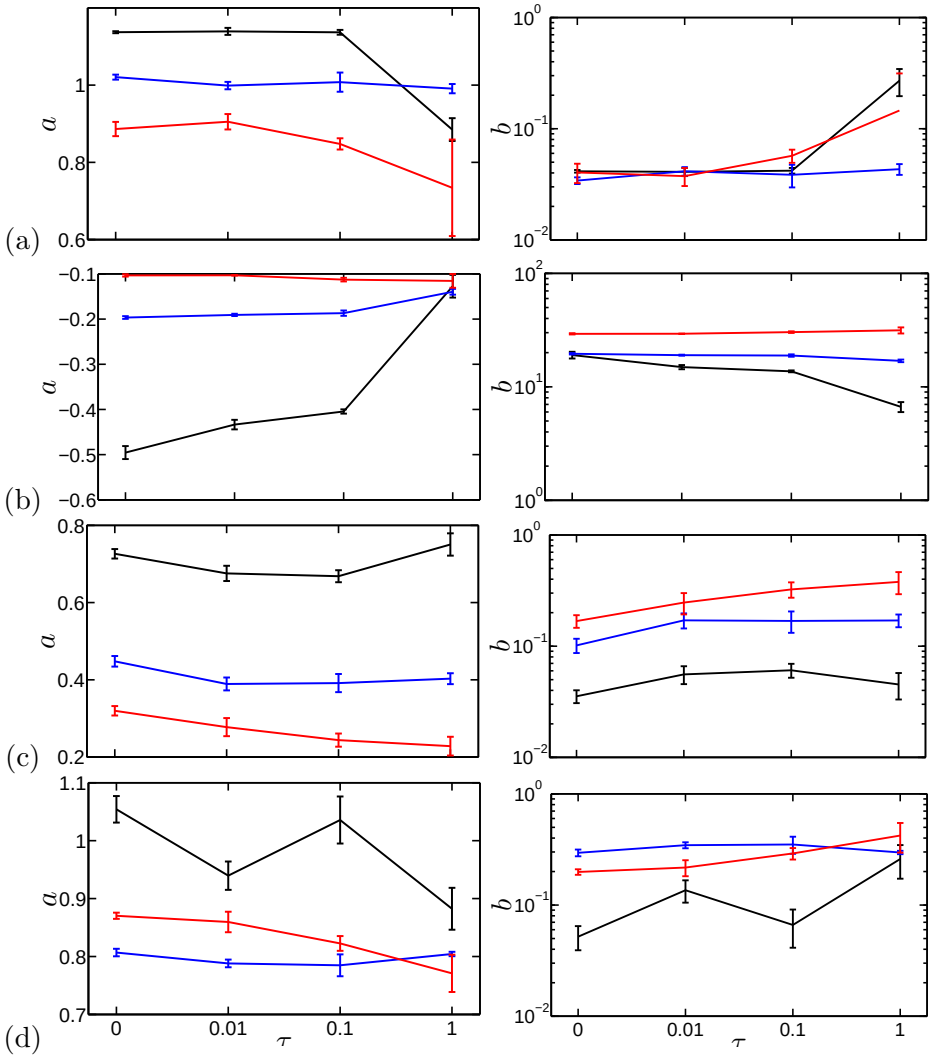

Figure 5.21: Fit parameters a and b vs. motor force. (a) Broken bonds at peak load vs. total number of bonds. (b) Peak load vs. side length. (c) Average degree of degeneracy vs. total number of bonds. (d) Final degree of degeneracy vs. total number of bonds. Parameters are: $dt = 10^{-3}$, 10^{-5}, 10^{-8} (indicated by colors black, blue, and red). Solid lines are for FBC, dashed lines are for PBC. Vertical lines are error bars.

increases with system size. Lifetime scales as a power law of the side length of the network, The number of broken bonds at failure scales as a power law of the total bond number. Increase of strain drastically decreases lifetime and number of broken bonds at failure. The latter results from correlations in the bond network. We quantitatively analyzed this by calculation of the damage profile. This shows that without strain bonds break in an uncorrelated fashion, but with increasing strain damage is clearly localized, i.e. a fatal crack destroys the network. This effect is even more pronounced if we centrally cut the network orthogonal to strain. Such a predamage leads to accumulation of stress and therefore dramatically decreases lifetime and the number of broken bonds necessary for system failure.

The investigation of different regular topologies revealed that triangular networks live longest. We also compared the results obtained with regular networks to those obtained with a network of irregular topology. We found that irregularity stabilizes the bond network.

In large part, in this section we model bonds as harmonic springs, but we also compared the results obtained using the spring model to those we get if the bonds act as passive or active cables. As long as motor forces are small these are dominated by the elastic forces. Hence, the differences between springs and cables as bond models is marginal for small motor forces. For the CD using active cables instead of springs slowly decreases lifetime.

The LD under fast pulling speed is very closely related to the random spring model (RSM). Therefore we studied the same statistical properties which are also investigated in common fracture mechanics. The force-extension curve of a network of bio-molecular bonds subject to a linearly increasing displacement, starts at zero, then it increases to a maximum, the so-called peak load, followed by a force decay up to zero, failure. Hereby we observe that the faster we pull the network the higher the strain it can stand / the higher peak load / the shorter the network lifetime. For fast pulling the behavior before and after peak load become more and more distinct. This can be seen on the damage profiles, which are used to study fracture localization. Before peak load, damage is diffusely distributed over the network. But for high pulling speed after peak load it clearly localizes. In stark contrast to the RSM, for slow pulling damage does not localize in the postpeak regime, the damage profile stays almost constant.

We find that the mean number of broken bonds at peak load, the mean degree of degeneracy which is defined as the mean number of bonds which break during one time-step up to peak load, the final degree of degeneracy which is defined as the mean number of bonds which break from peak load to failure, and the number of elongation steps taken during the simulation all scale as power laws as function of the total bond number. The scaling exponent is always positive, i.e. all these statistical quantities increase with system size. The fracture strength which is defined as peak load divided by clamped side length shows a power law dependence from the network's side length. Here the scaling exponent is negative, hence fracture strength decreases with system size.

If it has a non-vanishing component perpendicular to the applied strain, predamage decreases peak load and the strain at failure. It furthermore sharpens the distinction of pre- and postpeak regime, even at intermediate pulling speeds clear fracture localization after peak load is observed. A central cut will grow until it spans over the whole network. Only very few bonds break diffusely; i.e. rupture due to thermal fluctuations is almost switched off. But for very slow pulling speed the statistical behavior of the bond network is not influenced by predamage.

Appendix A

Homogenization

A.1 Finite Difference Method

The finite difference method offers an intuitive way to solve partial differential equations by only taking into account equidistant data points spaced by $\Delta > 0$. That is, we only calculate $f(i\Delta, j\Delta)$ for $i, j \in \mathbb{N}_0$. Here, f may represent φ_x or φ_y from the continuous deformation function $\vec{\varphi} = (\varphi_x, \varphi_y)$. The partial derivatives can then be approximated by:

$$\partial_x f(i\Delta, j\Delta) \approx \frac{f((i+1)\Delta, j\Delta) - f((i-1)\Delta, j\Delta)}{2\Delta}, \tag{A.1}$$

$$\partial_x^2 f(i\Delta, j\Delta) \approx \frac{f((i+1)\Delta, j\Delta) + f((i-1)\Delta, j\Delta) - 2f(i\Delta, j\Delta)}{\Delta^2}. \tag{A.2}$$

The inaccuracy is $\mathcal{O}(\Delta^2)$ as can be easily verified by inserting the Taylor expansions

$$\begin{aligned} f((i \pm 1)\Delta, j\Delta) = {} & f(i\Delta, j\Delta) \pm \Delta \partial_x f(i\Delta, j\Delta) + \frac{1}{2}\Delta^2 \partial_x^2 f(i\Delta, j\Delta) \\ & \pm \frac{1}{6}\Delta^3 \partial_x^3 f(i\Delta, j\Delta) + \mathcal{O}(\Delta^4) \end{aligned} \tag{A.3}$$

into Eqs. A.1 and A.2. $\partial_y f(i\Delta, j\Delta)$ and $\partial_y (i\Delta, j\Delta)^2$ are approximated in a completely analog way.

If Eqs. (3.32)-(3.37) are discretized in the prescribed manner solving these partial differential equations reduces to calculating the root of a large system of equations. We are aware that it appears strange to assume a discretized square lattice after homogenization of a square network.

A.2 A Homogenization Approach to ACNs

To avoid a piecewise defined function in the homogenized equations, here we replace the force-extension relation Eq. (2.5) for $\tau = \ell = 1$ ad hoc by

$$\vec{f}_{ij} = (\ell_{ij} - c)^3 \, \vec{e}_{i,j}, \text{ with } c = \frac{3\ell - 1}{d}. \tag{A.4}$$

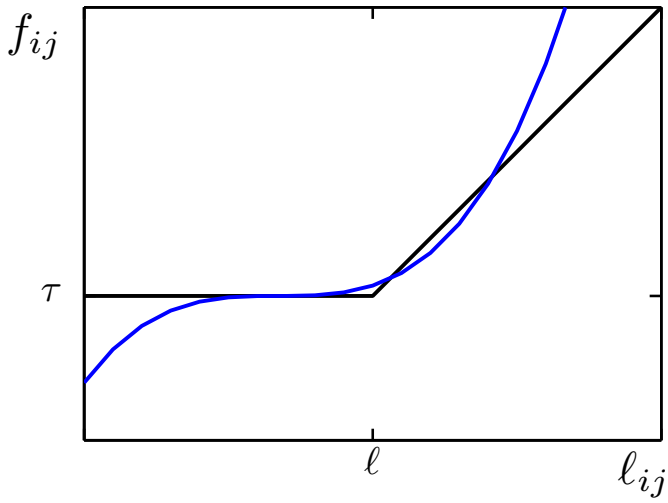

Figure A.1: Smoothed force-extension curve for an ACN. Black line: Force-extension curve for the ACN, see Eq. (2.8). Blue line: Force-extension curve according to Eq. (A.4).

This approximation is reasonable at least in the vicinity of the inital link length ℓ, see Fig. A.1. If we follow the homogenization technique discussed in section 3.7 for the ACN we get the following equation:

$$\partial_x \left(\frac{(|\partial_x \vec{\varphi}| - c)^3}{|\partial_x \vec{\varphi}|} \partial_x \vec{\varphi} \right) + \partial_y \left(\frac{(|\partial_y \vec{\varphi}| - c)^3}{|\partial_y \vec{\varphi}|} \partial_y \vec{\varphi} \right) = 0 \tag{A.5}$$

and vanishing stress orthogonal to the contour as boundary condition. Stresses are given by:

$$\vec{S}_x = \frac{(|\partial_x \vec{\varphi}| - c)^3}{|\partial_x \vec{\varphi}|} (\partial_x \vec{\varphi}), \tag{A.6}$$

$$\vec{S}_y = \frac{(|\partial_y \vec{\varphi}| - c)^3}{|\partial_y \vec{\varphi}|} (\partial_y \vec{\varphi}). \tag{A.7}$$

Appendix B

Overview of the analyzed Experimental Data

B.1 Wild Type MDCK Cells

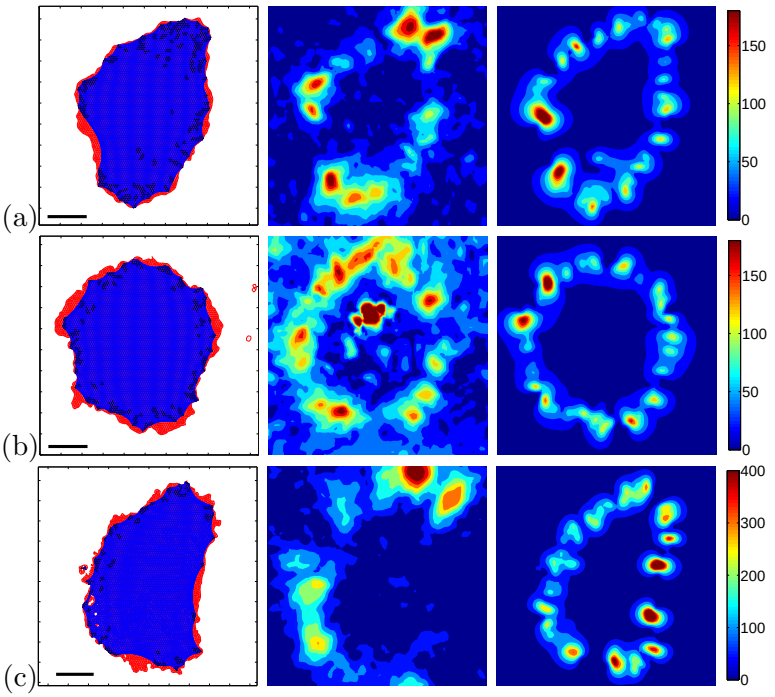

Figure B.1: Equilibrium states and traction stress magnitudes for MDCK cells. The contracted equilibrium states are shown on the left. Color codes give traction stress magnitudes (middle figures: experimental data, right figures: simulation result). Used parameters are: $\tau = 3 \times 10^{-5}$, $\bar{\ell} = 5\ px$. Traction stress is given by a heatmap and in Pa. The length of the bar is 10 μm.

B.2 Wild Type Mouse 3T3 Fibroblasts

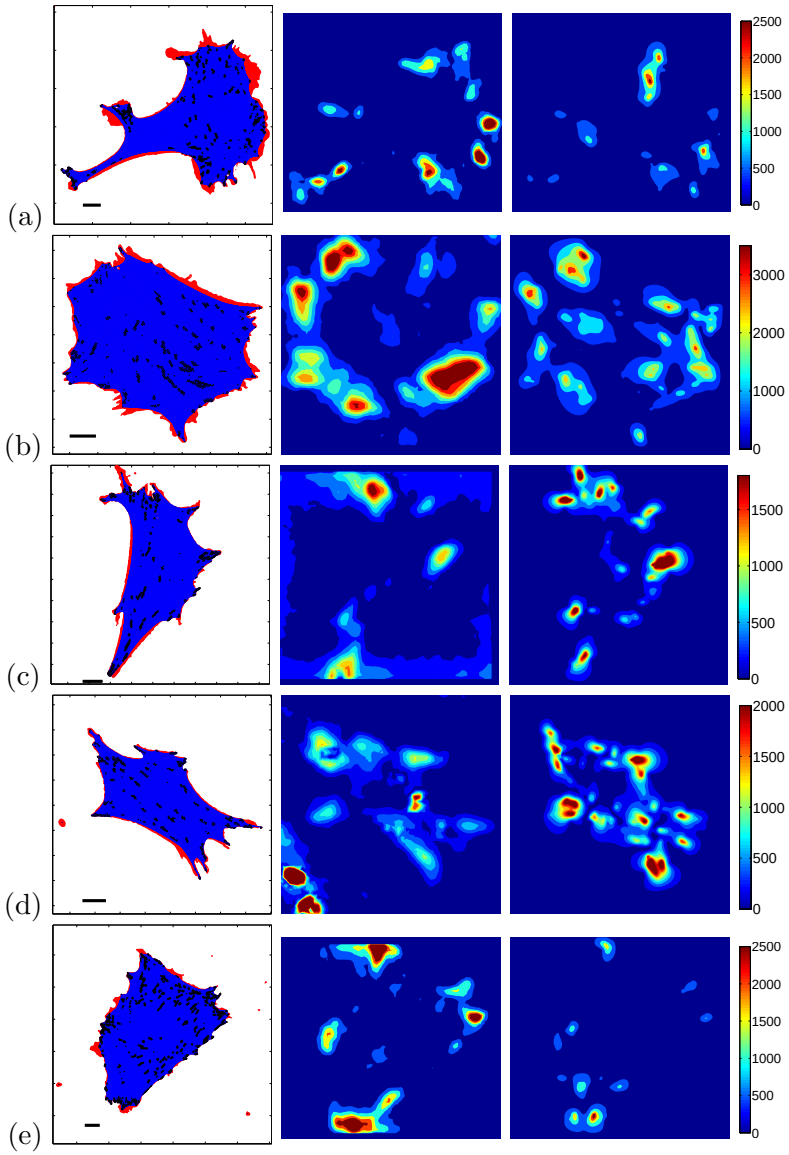

Figure B.2: Equilibrium states and traction stress magnitudes for 3T3 fibroblasts. The contracted equilibrium states are shown on the left. Color codes give traction stress magnitudes (middle figures: experimental data, right figures: simulation result). Used parameters are: $\tau_d = \tau_t = 0.02$, $\tau_v = 10^{-5}$, $\tau = 10^{-4}$, $\bar{\ell} = 5\ px$ (for (a),(c),(d)). $\tau_d = \tau_t = 0.03$, $\tau_v = 10^{-5}$, $\tau = 10^{-4}$, $\bar{\ell} = 5\ px$ (for (b),(e)). Traction stress is given by a heatmap and in Pa. The length of the bar is 10 μm.

B.3 Wild Type and mDia inhibited U2OS Cells

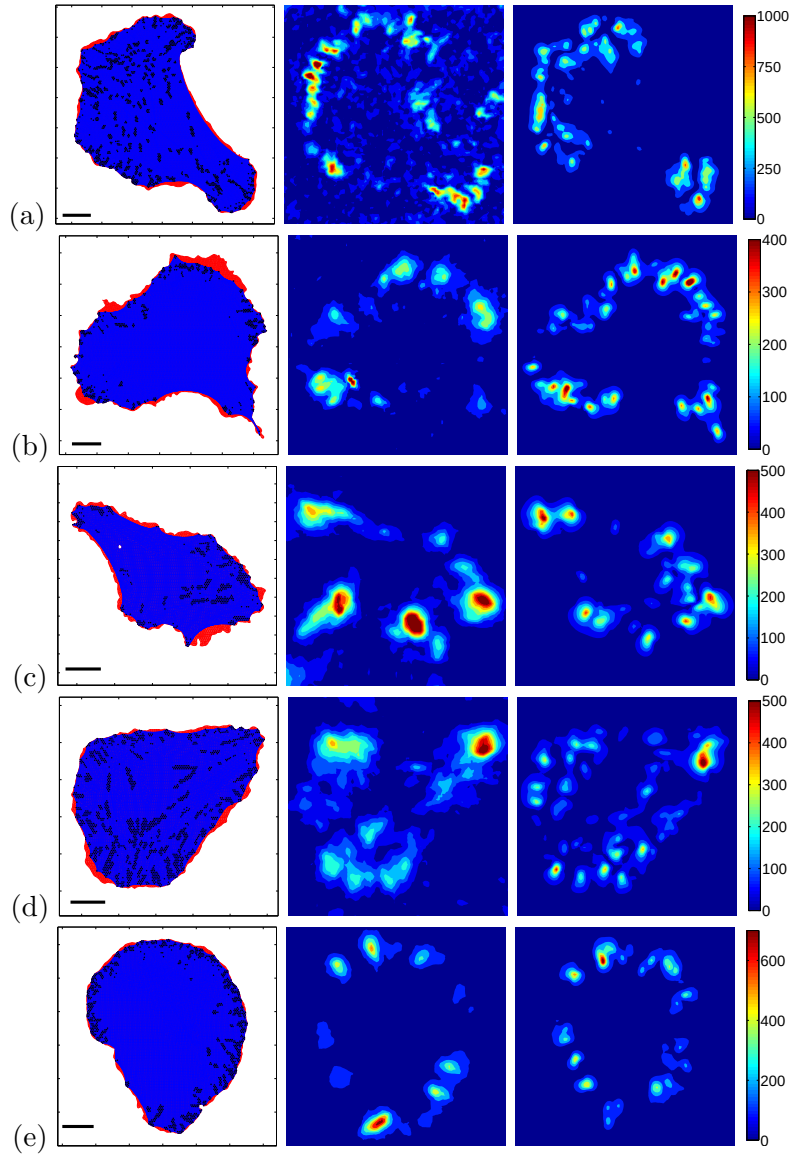

Figure B.3: Equilibrium states and traction stress magnitudes of WT and mDia1 inhibited U2OS cells. (a) and (b) wild type cells. (c)-(e) mDia1 inhibited cells. The contracted equilibrium states are shown on the left. Color codes give traction stress magnitudes (middle figures: experimental data, right figures: simulation result). Used parameters are: $\tau_d = \tau_t = 10^{-3}$, $\tau_v = \tau = 10^{-5}$, $\bar{\ell} = 5\ px$. Traction stress is given by a heatmap and in Pa. The length of the bar is 10 μm.

Figs. B.1, B.2, and B.3 show cell shape and traction stress distribution for the optimal parameters of MDCK cells, 3T3 fibroblasts, and U2OS cells, respectively. The optimal tension parameters vary only slightly within one cell type, but by orders of magnitude for the different cell types. Hence, our model captures the features of contractile cells very well.

B.4 U2OS Cells treated with Y-27632

Figs. B.4 and B.5 show that optimal parameters vary slightly for cells treated with the same inhibitor concentration, but much stronger if inhibitor concentration is changed. In contrast to the previous sections, we do not plot the results for the optimal parameters here but for the same two parameter values for each of the analyzed cells. This shows that stress fiber contractility decreases with myosin inhibitor concentration.

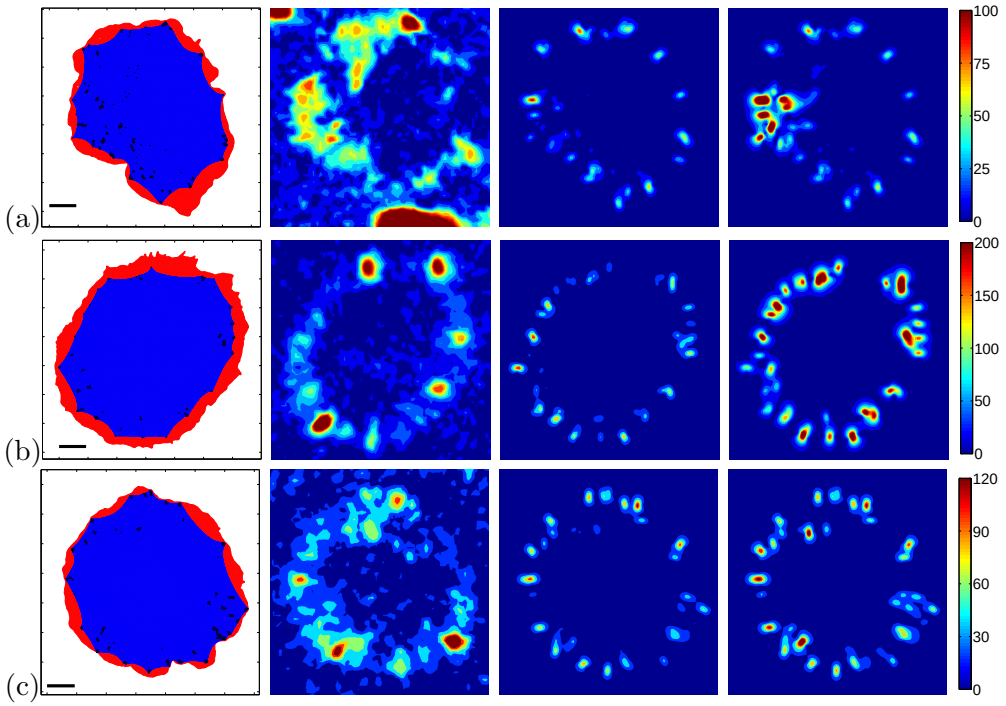

Figure B.4: Equilibrium states and traction stress magnitudes for U2OS cells treated with 2 μM of Y-27632. The contracted equilibrium states for $\tau_d = 8 \times 10^{-4}$ are shown on the left. Color codes give traction stress magnitudes (second from the left: experimental data, third from the left: simulation results for $\tau_d = 10^{-4}$, right: simulation results for $\tau_d = 8 \times 10^{-4}$). Other used parameters are: $\tau = \tau_v = 10^{-6}$, $\tau_t = 10^{-4}$, $\bar{\ell} = 5\ px$. Traction stress is given by a heatmap and in Pa. The length of the bar is 10 μm.

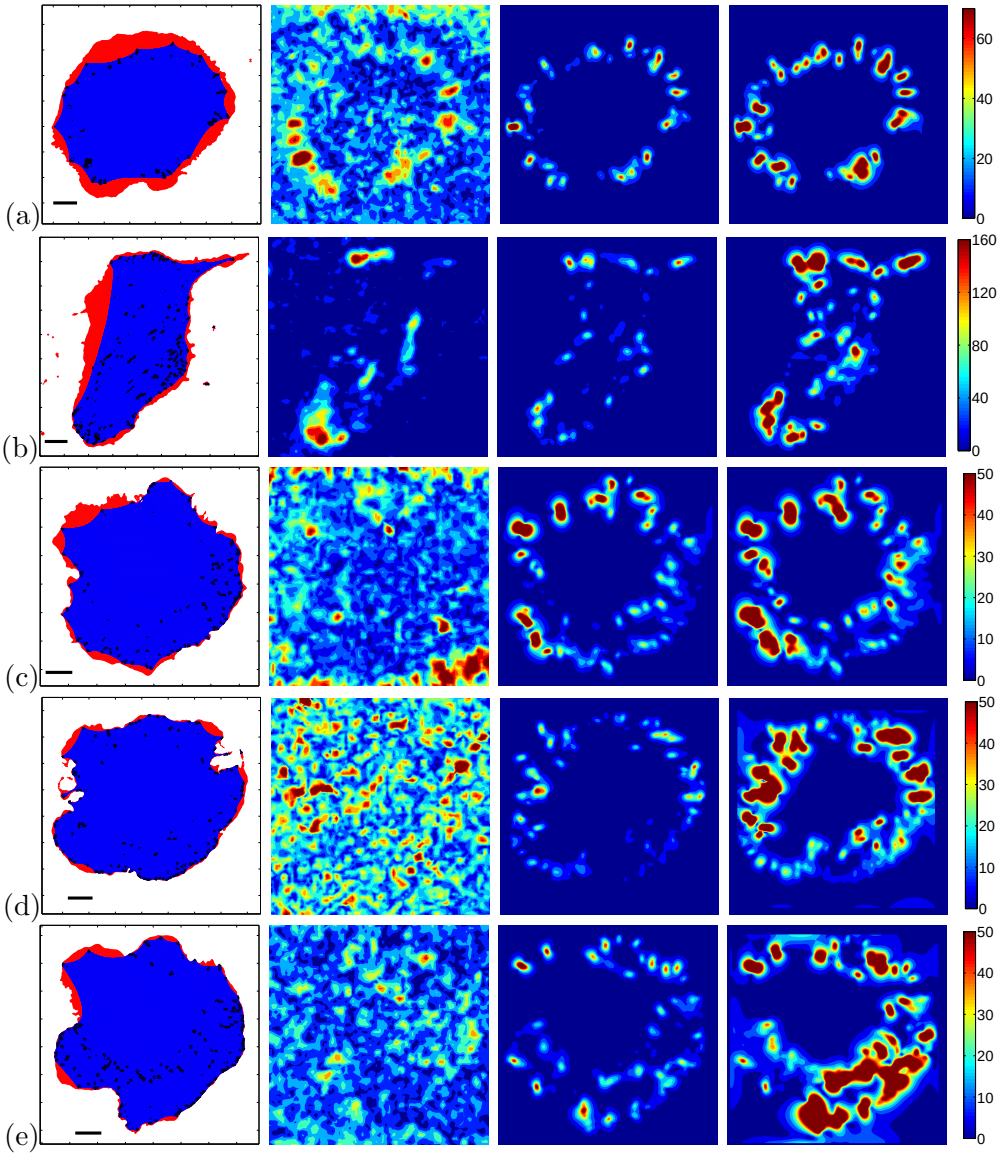

Figure B.5: Equilibrium states and traction stress magnitudes for U2OS cells treated with 5 μM and 10 μM of Y-27632. (a),(b) 5 μM Y-27632. (c)-(e) 10 μM Y-27632. The contracted equilibrium states for $\tau_d = 3 \times 10^{-4}$ (a),(b) and $\tau_d = 10^{-4}$ (c)-(e) are shown on the left. Color codes give traction stress magnitudes (second from the left: experimental data, third from the left: simulation results for $\tau_d = 10^{-4}$, right: simulation results for $\tau_d = 8 \times 10^{-4}$). Other used parameters are: $\tau = \tau_v = 10^{-6}$, $\tau_t = 10^{-4}$, $\bar{\ell} = 5\ px$. Traction stress is given by a heatmap and in Pa. The length of the bar is 10 μm.

B. OVERVIEW OF THE ANALYZED EXPERIMENTAL DATA

References

[1] B. Alberts, A. Johnson, J. Lewis, M. Raff, K. Roberts, and P. Walter. *Molecular Biology of the Cell*. Garland Science, New York, 2002.

[2] A. Ott, M. Magnasco, A. Simon, and A. Libchaber. **Measurement of the persistence length of polymerized actin using fluorescence microscopy**. *Phys. Rev. E*, **48**:R1642–R1645, 1993.

[3] J. L. Podolski and T. L. Steck. **Length distribution of F-actin in Dictyostelium discoideum**. *J. Biol. Chem.*, **265**:1312–1318, 1990.

[4] R. J. Pelham Jr and F. Chang. **Actin dynamics in the contractile ring during cytokinesis in fission yeast**. *Nature*, **419**:82–86, 2002.

[5] T. M. Svitkina, A. B. Verkhovsky, K. M. McQuade, and G. G. Borisy. **Analysis of the Actin-Myosin II System in Fish Epidermal Keratocytes: Mechanism of Cell Body Translocation**. *J. Cell Biol.*, **139**:397–415, 1997.

[6] B. Geiger, J. P. Spatz, and A. D. Bershadsky. **Environmental sensing through focal adhesions**. *Nat. Rev. Mol. Cell Biol.*, **10**:21–33, 2009.

[7] J. Howard. *Mechanics of Motor Proteins and the Cytoskeleton*. Sinauer Associates, Inc., Sunderland, Massachusetts, 2001.

[8] M.-F. Carlier, V. Laurent, J. Santolini, R. Melki, D. Didry, G.-X. Xia, Y. Hong, N.-H. Chua, and D. Pantaloni. **Actin Depolymerizing Factor (ADF/Cofilin) Enhances the Rate of Filament Turnover: Implication in Actin-based Motility**. *J. Cell Biol.*, **136**:1307–1322, 1997.

[9] M. Evangelista, S. Zigmond, and C. Boone. **Formins: signaling effectors for assembly and polarization of actin filaments**. *J. Cell Sci.*, **116**:2603–2611, 2003.

[10] T. D. Pollard. **Regulation of actin filament assembly by Arp2/3 complex and formins**. *Annu. Rev. Biophys. Biomol. Struct.*, **36**:451–477, 2007.

[11] J. E. Molloy, J. E. Burns, J. Kendrick-Jones, R. T. Tregear, and D. C. S. White. **Movement and force produced by a single myosin head**. *Nature*, **378**:209–212, 1995.

[12] L. Kreplak, H. Herrmann, and U. Aebi. **Tensile Properties of Single Desmin Intermediate Filaments**. *Biophys. J.*, **94**:2790–2799, 2008.

[13] P. A. Janmey, U. Euteneuer, P. Traub, and M. Schliwa. **Viscoelastic Properties of Vimentin Compared with Other Filamentous Biopolymer Networks**. *J. Cell Biol.*, **113**:155–160, 1991.

[14] D. Lehnert, B. Wehrle-Haller, C. David, U. Weiland, C. Ballestrem, B. A. Imhof, and M. Bastmeyer. **Cell behaviour on micropatterned substrata: limits of extracellular matrix geometry for spreading and adhesion**. *J. Cell Sci.*, **117**:41–52, 2004.

[15] I. B. Bischofs, F. Klein, D. Lehnert, M. Bastmeyer, and U. S. Schwarz. **Filamentous network mechanics and active contractility determine cell and tissue shape**. *Biophys. J.*, **95**:3488–3496, 2008.

[16] Y. Aratyn-Schaus, P .W. Oakes, J. Stricker, S. P. Winter, and M. L. Gardel. **Preparation of Complaint Matrices for Quantifying Cellular Contraction**. *J. Vis. Exp.*, **46**:e2173, 2010.

[17] B. Sabass, M. L. Gardel, C. M. Waterman, and U. S. Schwarz. **High resolution traction force microscopy based on experimental and computational advances**. *Biophys. J.*, **94**:207–220, 2008.

[18] S. Pellegrin and H. Mellor. **Actin stress fibres**. *J. Cell Sci.*, **120**:3491–3499, 2007.

[19] P. Hotulainen and P. Lappalainen. **Stress fibers are generated by two distinct actin assembly mechanisms in motile cells**. *J. Cell Biol.*, **173**:383–394, 2006.

[20] V. Niggli. **Rho-kinase in human neutrophils: a role in signalling for myosin light chain phosphorylation and cell migration**. *FEBS Letters*, **445**:69–72, 1999.

[21] M. Kovács, J. Tóth, C. Hetényi, A. Málnási-Csizmadia, and J. R. Sellers. **Mechanism of Blebbistatin Inhibition of Myosin II**. *J. Biol. Chem.*, **279**:35557–35563, 2004.

[22] P. A. Janmey, J. P. Winer, M. E. Murray, and Q. Wen. **The hard life of soft cells**. *Cell Motil. Cytoskel.*, **66**:597–605, 2009.

[23] B. Hinz, S. H. Phan, V. J. Thannickal, A. Galli, M.-L. Bochaton-Piallat, and G. Gabbiani. **The Myofibroblast. One Function, Multiple Origins**. *Am J. Pathol.*, **170**:1807–1816, 2007.

[24] R. Zaidel-Bar, S. Itzkovitz, A. Ma'ayan, R. Iyengar, and B. Geiger. **Functional atlas of the integrin adhesome**. *Nat. Cell Biol.*, **9**:858–867, 2007.

[25] R. Zaidel-Bar and B. Geiger. **The switchable integrin adhesome**. *J. Cell Sci.*, **123**:1385–1388, 2010.

[26] B. D. Hoffman, C. Grashoff, and M. A. Schwartz. **Dynamic molecular processes mediate cellular mechanotransduction**. *Nature*, **475**:316–323, 2011.

[27] A. Fire, S. Xu, M. K. Montgomery, S. A. Kostas, S. E. Driver, and C. C. Mello. **Potent and specific genetic interference by double-stranded RNA in Caenorhabditis elegans**. *Nature*, **391**:806–811, 1998.

[28] M. Dembo and Y.-L. Wang. **Stresses at the cell-to-substrate interface during locomotion of fibroblasts**. *Biophys. J.*, **76**:2307–2316, 1999.

[29] J. P. Butler, I. M. Tolić-Nørrelykke, B. Fabry, and J. J. Fredberg. **Traction fields, moments, and strain energy that cells exert on their surroundings**. *Am. J. Physiol. Cell Physiol.*, **282**:C595–C605, 2002.

[30] U. S. Schwarz, N. Q. Balaban, D. Riveline, A. Bershadsky, B. Geiger, and S. A. Safran. **Calculation of forces at focal adhesions from elastic substrate data: The effect of localized force and the need for regularization**. *Biophys. J.*, **83**:1380–1394, 2002.

[31] J. L. Tan, J. Tien, D. M. Pirone, D. S. Gray, K. Bhadriraju, and C. S. Chen. **Cells lying on a bed of microneedles: An approach to isolate mechanical force**. *Proc. Natl. Acad. Sci. USA*, **100**:1484–1489, 2003.

REFERENCES

[32] N. Q. Balaban, U. S. Schwarz, D. Riveline, P. Goichberg, G. Tzur, I. Sabanay, D. Mahalu, S. Safran, A. Bershadsky, L. Addadi, and B. Geiger. **Force and focal adhesion assembly: a close relationship studied using elastic micropatterned substrates**. *Nat. Cell Biol.*, **3**:466–472, 2001.

[33] Z. Liu, J. L. Tan, D. M. Cohen, M. T. Yang, N. J. Sniadecki, S. A. Ruiz, C. M. Nelson, and C. S. Chen. **Mechanical tugging force regulates the size of cell-cell junctions**. *Proc. Natl. Acad. Sci. USA*, **107**:9944–9949, 2010.

[34] V. Maruthamuthu, B. Sabass, U. S. Schwarz, and M. L. Gardel. **Cell-ECM traction force modulates endogenous tension at cell-cell contacts**. *Proc. Natl. Acad. Sci. USA*, **108**:4708–4713, 2011.

[35] I. B. Bischofs, S. S. Schmidt, and U. S. Schwarz. **Effect of adhesion geometry and rigidity on cellular force distributions**. *Phys. Rev. Lett.*, **103**:048101, 2009.

[36] S. W. Grill, P. Gönczy, E. H. K. Stelzer, and A. A. Hyman. **Polarity controls forces governing asymmetric spindle positioning in the Caenorhabditis elegans embryo**. *Nature*, **409**:630–633, 2001.

[37] S. W. Grill, J. Howard, E. Schäffer, E. H. K. Stelzer, and A. A. Hyman. **The distribution of active force generators controls mitotic spindle position**. *Science*, **301**:518–521, 2003.

[38] S. Kumar, I. Z. Maxwell, A. Heisterkamp, T. R. Polte, T. P. Lele, M. Salanga, E. Mazur, and D. E. Ingber. **Viscoelastic retraction of single living stress fibers and its impact on cell shape, cytoskeletal organization, and extracellular matrix mechanics**. *Biophys. J.*, **90**:3762–3773, 2006.

[39] K. Tanner, A. Boudreau, M. J. Bissell, and S. Kumar. **Dissecting Regional Variations in Stress Fiber Mechanics in Living Cells with Laser Nanosurgery**. *Biophys. J.*, **99**:2775–2783, 2010.

[40] J. Colombelli, A. Besser, H. Kress, E. G. Reynaud, P. Girard, E. Caussinus, U. Haselmann, J. V. Small, U. S. Schwarz, and E. H. K. Stelzer. **Mechanosensing in actin stress fibers revealed by a close correlation between force and protein localization**. *J. Cell. Sci.*, **122**:1665–1679, 2009.

[41] M. A. Smith, E. Blankman, M. L. Gardel, L. Luettjohann, C. M. Waterman, and M. C. Beckerle. **A Zyxin-Mediated Mechanism for Actin Stress Fiber Maintenance and Repair**. *Dev. Cell*, **19**:365–376, 2010.

[42] M. Mayer, M. Depken, J. S. Bois, F. Jülicher, and S. W. Grill. **Anisotropies in cortical tension reveal the physical basis of polarizing cortical flows**. *Nature*, **467**:617–621, 2010.

[43] D. Riveline, E. Zamir, N. Q. Balaban, U. S. Schwarz, T. Ishizaki, S. Narumiya, Z. Kam, B. Geiger, and A. D. Bershadsky. **Focal contacts as mechanosensors: Externally applied local mechanical force induces growth of focal contacts by an mDia1-dependent and ROCK-independent mechanism**. *J. Cell. Biol.*, **153**:1175–1186, 2001.

[44] R. Paul, P. Heil, J. P. Spatz, and U. S. Schwarz. **Propagation of mechanical stress through the actin cytoskeleton toward focal adhesions: model and experiment**. *Biophys. J.*, **94**:1470–1482, 2008.

[45] P. Heil and J. P. Spatz. **Lateral shear forces applied to cells with single elastic micropillars to influence focal adhesion dynamics**. *J. Phys. Condens. Matter*, **22**:194108, 2010.

[46] D. Kirchenbüchler, S. Born, N. Kirchgessner, S. Houben, B. Hoffmann, and R. Merkel. **Substrate, focal adhesions, and actin filaments: a mechanical unit with a weak spot for mechanosensitive proteins**. *J. Phys. Condens. Matter*, **22**:194109, 2010.

[47] S. Sivaramakrishnan, J. V. DeGiulio, L. Lorand, R. D. Goldman, and K. M. Ridge. **Micromechanical properties of keratin intermediate filament networks**. *Proc. Natl. Acad. Sci. USA.*, **105**:889–894, 2008.

[48] T. Ackbarow, D. Sen, C. Thaulow, and M. J. Buehler. **Alpha-Helical Protein Networks Are Self-Protective and Flaw-Tolerant**. *PLOS One*, **4**:e6015, 2009.

[49] B. Suki, S. Ito, D. Stamenović, K. R. Lutchen, and E. P. Ingenito. **Biomechanics of the lung parenchyma: Critical roles of collagen and mechanical forces**. *J. Appl. Physiol.*, **98**:1892–1899, 2005.

[50] M. C. Ritter, R. Jesudason, A. Majumdar, D. Stamenović, J. A. Buczek-Thomas, P. J. Stone, M. A. Nugent, and B. Suki. **A zipper network model of the failure of extracellular matrices**. *Proc. Natl. Acad. Sci. USA*, **106**:1081–1086, 2009.

[51] K. M. Yamada. **Fibronectin peptides in cell migration and wound repair**. *J. Clin. Invest.*, **105**:1507–1509, 2000.

[52] B. Geiger, A. Bershadsky, R. Pankov, and K. M. Yamada. **Transmembrane extracellular matrix-cytoskeleton crosstalk**. *Nat. Rev. Mol. Cell Biol.*, **2**:793–805, 2001.

[53] M. Barczyk, S. Carracedo, and D. Gullberg. **Integrins**. *Cell Tissue Res.*, **339**:269–280, 2010.

[54] C. Selhuber-Unkel, T. Erdmann, M. López-García, H. Kessler, U. S. Schwarz, and J. P. Spatz. **Cell Adhesion Strength Is Controlled by Intermolecular Spacing of Adhesion Receptors**. *Biophys. J.*, **98**:543–551, 2010.

[55] R. Merkel. **Force spectroscopy on single passive biomolecules and single biomolecular bonds**. *Phys. Rep.*, **346**:343–385, 2001.

[56] T. A. Springer. **Traffic Signals on Endothelium for Lymphocyte Recirculation and Leukocyte Emigration**. *Ann. Rev. Physiol.*, **57**:827–872, 1995.

[57] T. Funatsu, H. Higuchi, and S. Ishiwata. **Elastic filaments in skeletal muscle revealed by selective removal of thin filaments with plasma gelsolin**. *J. Cell Biol.*, **110**:53–62, 1990.

[58] E. Evans. **Probing the Relation between Force-Lifetime-and Chemistry in Single Molecular Bonds**. *Annu. Rev. Biophys. Biomol. Struct.*, **30**:105–128, 2001.

[59] G. Binnig, C. F. Quate, and C. Gerber. **Atomic Force Microscope**. *Phys. Rev. Lett.*, **56**:930–933, 1986.

[60] A. Ashkin. **Acceleration and trapping of particles by radiation pressure**. *Phys. Rev. Lett.*, **24**:156–159, 1970.

[61] A. Ashkin, J. M. Dziedzic, J. E. Bjorkholm, and S. Chu. **Observation of a single-beam gradient force optical trap for dielectric particles**. *Opt. Lett.*, **11**:288–290, 1986.

[62] E. Evans, K. Ritchie, and R. Merkel. **Sensitive force technique to probe molecular adhesion and structural linkages at biological interfaces**. *Biophys. J.*, **68**:2580–2587, 1995.

[63] D. Rugar, H. J. Mamin, and Guethner P. **Improved fiberoptic interferometer for atomic force microscopy**. *Appl. Phys. Lett.*, **55**:2588–2590, 1989.

[64] D. Boal. *Mechanics of the Cell*. Cambridge University Press, Cambridge, 2002.

[65] J. C. Hansen, R. Skalak, S. Chien, and A. Hoger. **An elastic network model based on the structure of the red blood cell membrane skeleton**. *Biophys. J.*, **70**:146–166, 1996.

[66] J. C. Hansen, R. Skalak, S. Chien, and A. Hoger. **Influence of network topology on the elasticity of the red blood cell membrane skeleton**. *Biophys. J.*, **72**:2369–2381, 1997.

[67] S. K. Boey, D. H. Boal, and D. E. Discher. **Simulations of the erythrocyte cytoskeleton at large deformation. I. Microscopic models**. *Biophys. J.*, **75**:1573–1583, 1998.

[68] D. E. Discher, D. H. Boal, and S. K. Boey. **Simulations of the erythrocyte cytoskeleton at large deformation. II. Micropipette aspiration**. *Biophys. J.*, **75**:1584–1597, 1998.

[69] G. Lim H. W., M. Wortis, and R. Mukhopadhyay. **Stomatocyte-discocyte-echinocyte sequence of the human red blood cell: Evidence for the bilayer-couple hypothesis from membrane mechanics**. *Proc. Natl. Acad. Sci. USA*, **99**:16766–16769, 2002.

[70] H. Noguchi and G. Gompper. **Shape transitions of fluid vesicles and red blood cells in capillary flows**. *Proc. Natl. Acad. Sci. USA*, **102**:14159–14164, 2005.

[71] J. Li, M. Dao, C. T. Lim, and S. Suresh. **Spectrin-level modeling of the cytoskeleton and optical tweezers stretching of the erythrocyte**. *Biophys. J.*, **88**:3707–3719, 2005.

[72] J. Li, G. Lykotrafitis, M. Dao, and S. Suresh. **Cytoskeletal dynamics of human erythrocyte**. *Proc. Natl. Acad. Sci. USA*, **104**:4937–4942, 2007.

[73] D. A. Fedosov, B. Caswell, and G. E. Karniadakis. **A multiscale red blood cell model with accurate mechanics, rheology, and dynamics**. *Biophys. J.*, **98**:2215–2225, 2010.

[74] P. A. DiMilla, K. Barbee, and D. A. Lauffenburger. **Mathematical model for the effects of adhesion and mechanics on cell migration speed**. *Biophys. J.*, **60**:15–37, 1991.

[75] M. E. Gracheva and H. G. Othmer. **A Continuum Model of Motility in Ameboid Cells**. *Bull. Math. Biol.*, **66**:167–193, 2004.

[76] D. Bottino, A. Mogilner, T. Roberts, M. Stewart, and G. Oster. **How nematode sperm crawl**. *J. Cell Sci.*, **115**:367–384, 2002.

[77] I. V. Dokukina and M. E. Gracheva. **A Model of Fibroblast Motility on Substrates with Different Rigidities**. *Biophys. J.*, **98**:2794–2803, 2010.

[78] D. Caillerie, K. John, C. Misbah, P. Peyla, and A. Raoult. **A constitutive law for cross-linked actin networks by homogenization techniques**. 2010. arXiv:1011.3196v1 (Preprint).

[79] V. S. Deshpande, R. M. McMeeking, and A. G. Evans. **A bio-chemo-mechanical model for cell contractility**. *Proc. Natl. Acad. Sci. USA*, **103**:14015–14020, 2006.

[80] M. F. Coughlin and D. Stamenović. **A prestressed cable network model of the adherent cell cytoskeleton**. *Biophys. J.*, **84**:1328–1336, 2003.

[81] M. S. Zand and G. Albrecht-Buehler. **What structures, besides adhesions, prevent spread cells from rounding up?** *Cell Motil. Cytoskel.*, **13**:195–211, 1989.

[82] R. Bar-Ziv, T. Tlusty, E. Moses, S. A. Safran, and A. Bershadsky. **Pearling in cells: A clue to understanding cell shape**. *Proc. Natl. Acad. Sci. USA*, **96**:10140–10145, 1999.

[83] A. A. Griffith. **The phenomena of rupture and flow in solids**. *Philos. Trans. Roy. Soc. (London) A*, **221**:163–198, 1920.

[84] M. J. Alava, P. K. V. V. Nukala, and S. Zapperi. **Statistical models of fracture**. *Adv. Phys.*, **55**:349–476, 2006.

[85] T. Ackbarow, X. Chen, S. Keten, and M. J. Buehler. **Hierarchies, multiple energy barriers, and robustness govern the fracture mechanics of alpha-helical and beta-sheet protein domains**. *Proc. Natl. Acad. Sci. USA*, **104**:16410–16415, 2007.

[86] M. J. Buehler and S. Keten. **Failure of molecules, bones, and the earth itself**. *Rev. Mod. Phys.*, **82**:1459–1487, 2010.

[87] S. Pradhan, A. Hansen, and B. K. Chakrabarti. **Failure Processes in elastic fiber bundles**. *Rev. Mod. Phys.*, **82**:499–555, 2010.

[88] P. K. V. V. Nukala, S. Zapperi, and S. Šimunović. **Statistical properties of fracture in a random spring model**. *Phys. Rev. E*, **71**:066106, 2005.

[89] S. Zapperi, P. Ray, H. E. Stanley, and A. Vespignani. **First-Order Transition in the Breakdown of Disordered Media**. *Phys. Rev. Lett.*, **78**:1408–1411, 1997.

[90] H. A. Kramers. **Brownian motion in a field of force and the diffusion model of chemical reactions**. *Physica*, **7**:284–304, 1940.

[91] M. Rief, M. Gautel, F. Oesterhelt, J. M. Fernandez, and H. E. Gaub. **Reversible Unfolding of Individual Titin Immunoglobulin Domains by AFM**. *Science*, **276**:1109–1112, 1997.

[92] E. Evans and K. Ritchie. **Dynamic Strength of Molecular Adhesion Bonds**. *Biophys. J.*, **72**:1541–1555, 1997.

[93] G. I. Bell. **Models for the specific adhesion of cells to cells**. *Science*, **200**:618–624, 1978.

[94] R. Merkel, P. Nassoy, A. Leung, K. Ritchie, and E. Evans. **Energy landscapes of receptor-ligand bonds explored with dynamic force spectroscopy**. *Nature*, **397**:50–53, 1999.

[95] T. Erdmann and U. S. Schwarz. **Stability of adhesion clusters under constant force**. *Phys. Rev. Lett.*, **92**:108102, 2004.

[96] F. Kun, Z. Halász, J. S. Andrade Jr, and H. J. Herrmann. **Crackling noise in sub-critical fracture of heterogeneous materials**. *J. Stat. Mech.: Theory Exp.*, **P01021**, 2009.

[97] P. Guthardt Torres, I. B. Bischofs, and U. S. Schwarz. **Contractile network models for adherent cells**. *Phys. Rev. E*, **85**:011913, 2012.

[98] D. T. Gillespie. **A General Method for Numerically Simulating the Stochastic Time Evolution of Coupled Chemical Reactions**. *J. Com. Phys.*, **22**:403–434, 1976.

REFERENCES

[99] D. T. Gillespie. **Exact Stochastic Simulation of Coupled Chemical Reactions**. *J. Phys. Chem.*, **81**:2340–2361, 1977.

[100] P. K. V. V. Nukala and S. Šimunović. **An efficient algorithm for simulating fracture using large fuse networks**. *J. Phys. A: Math. Gen.*, **36**:11403–11412, 2003.

[101] P. K. V. V. Nukala and S. Šimunović. **An efficient block-circulant preconditioner for simulating fracture using large fuse networks**. *J. Phys. A: Math. Gen.*, **37**:2093–2103, 2004.

[102] C. F. Gerald and P. O. Wheatley. *Applied Numerical Analysis*. Addison-Wesley Publishing Company, Inc., Reading, 1989.

[103] R. Fletcher and C. M. Reeves. **Function minimization by conjugate gradients**. *Comp. J.*, **7**:149–154, 1964.

[104] W. H. Press, S. A. Teukolsky, W. T. Vettering, and B. P. Flannery. *Numerical Recipes in C++*. Cambridge University Press, Cambridge, 2002.

[105] N. Otsu. **A Threshold Selection Method from Gray-Level Histograms**. *IEEE Transactions on Systems, Man, and Cybernetics*, **9**:62–66, 1979.

[106] V. Vezhnevets and V. Konouchine. **GrowCut: Interactive multi-label ND image segmentation by cellular automata**. *Proc. of Graphicon*, pages 150–156, 2005.

[107] P.-O. Persson and G. Strang. **A simple mesh generator in Matlab**. *SIAM Rev.*, **46**:329–345, 2004.

[108] H. Edelsbrunner. *Geometry and Topology for Mesh Generation*. Cambridge University Press, Cambridge, 2001.

[109] L. D. Landau and E. M. Lifshitz. *Theory of Elasticity*, **7** of *Course of Theoretical Physics*. Pergamon Press, Oxford, 2nd edition, 1970.

[110] P. Howell, G. Kozyreff, and J. Ockendon. *Applied Solid Mechanics*. Cambridge University Press, Cambridge, 2009.

[111] M. E. J. Newman and R. M. Ziff. **Efficient Monte Carlo Algorithm and High-Precision Results for Percolation**. *Phys. Rev. Lett.*, **85**:4104–4107, 2000.

[112] M. E. J. Newman and R. M. Ziff. **Fast Monte Carlo algorithm for site or bond percolation**. *Phys. Rev. E*, **64**:016706, 2001.

[113] F. Gittes, B. Mickey, J. Nettleton, and J. Howard. **Flexural rigidity of microtubules and actin filaments measured from thermal fluctuations in shape**. *J. Cell Biol.*, **120**:923–934, 1993.

[114] S. Deguchi, T. Ohashi, and M. Sato. **Tensile properties of single stress fibers isolated from cultured vascular smooth muscle cells**. *J. Biomech.*, **39**:2603–2610, 2006.

[115] R. L. Satcher Jr and C. F. Dewey Jr. **Theoretical estimates of mechanical properties of the endothelial cell cytoskeleton**. *Biophys. J.*, **71**:109–118, 1996.

[116] K. Luby-Phelps, D. L. Taylor, and F. Lanni. **Probing the structure of cytoplasm**. *J. Cell Biol.*, **102**:2015–2022, 1986.

[117] S. Hildebrandt and A. Tromba. *The Parsimonious Universe: Shape and Form in the Natural World*. Springer, New York, 1996.

[118] E. H. Lockwood. *A book of curves*. Cambridge University Press, Cambridge, 2007.

[119] W. Whewell. **Of the Intrinsic Equation of a Curve, and its Application**. *Trans. Cambridge Philos. Soc.*, **8**:659–671, 1849.

[120] M. Doi and S. F. Edwards. *The theory of polymer dynamics*. Clarendon, Oxford, 1986.

[121] J. F. Marko and E. D. Siggia. **Stretching DNA**. *Macromolecules*, **28**:8759–8770, 1995.

[122] K. Kroy and E. Frey. **Force-Extension Relation and Plateau Modulus for Wormlike Chains**. *Phys. Rev. Lett.*, **77**:306–309, 1996.

[123] C. Heussinger and E. Frey. **Stiff Polymers, Foams, and Fiber Networks**. *Phys. Rev. Lett.*, **96**:017802, 2006.

[124] M. Yoshigi, L. M. Hoffman, C. C. Jensen, H. J. Yost, and M. C. Beckerle. **Mechanical force mobilizes zyxin from focal adhesions to actin filaments and regulates cytoskeletal reinforcement**. *J. Cell Biol.*, **171**:209–215, 2005.

[125] W. R. Legant, A. Pathak, M. T. Yang, V. S. Deshpande, R. M. McMeeking, and C. S. Chen. **Microfabricated tissue gauges to measure and manipulate forces from 3D microtissues.** *Proc. Natl. Acad. Sci. USA*, **106**:10097–10102, 2009.

[126] F. Klein, B. Richter, T. Striebel, C. M. Franz, G. von Freymann, M. Wegener, and M. Bastmeyer. **Two-Component Polymer Scaffolds for Controlled Three-Dimensional Cell Culture**. *Adv. Mater.*, **23**:1341–1345, 2011.

[127] M. F. Sykes and J. W. Essam. **Exact Critical Percolation Probabilities for Site and Bond Problems in Two Dimensions**. *J. Math. Phys.*, **5**:1117–1127, 1964.

[128] D. Stauffer and A. Aharony. *Introduction to Percolation Theory*. Taylor and Francis, London, 1994.

[129] P. K. V. V. Nukala, S. Šimunović, and S. Zapperi. **Percolation and localization in the random fuse model**. *J. Stat. Mech.: Theory Exp.*, **P08001**, 2004.

Danksagungen

An dieser Stelle möchte ich mich ganz herzlich bei all jenen bedanken, die zum Gelingen dieser Arbeit wesentlich beigetragen haben.

- Herrn Prof. Dr. Ulrich Schwarz danke ich dafür, dass er mich in seine Arbeitsgruppe aufgenommen hat und mir die Möglichkeit eröffnet hat, sowohl in Heidelberg als auch in Karlsruhe zu arbeiten. Desweiteren danke ich ihm für seine geduldige Beantwortung meiner vielen Fragen und seine hervorragende Betreuung dieser Arbeit.
- Ganz herzlich bedanken möchte ich mich auch bei Dr. Ilka Bischofs-Pfeifer, Dr. Thorsten Erdmann und Jérôme Soiné für viele hilfreiche Tipps in Bezug auf meine Arbeit.
- I would like to thank the people from the Gardel Lab, Dr. Margaret Gardel, Venkat Maruthamuthu, and Dr. Patrick Oakes for providing experimental data. Special thanks to Jonathan Stricker for experimental data, all the technical advice, and assistance in stress fiber identification.
- Vielen Dank an Christoph Brand, Dr. Thorsten Erdmann, Matthäus Langosch und Jérôme Soiné für das Korrekturlesen dieser Arbeit und die vielen hilfreichen Verbesserungsvorschläge.
- Bei Melinda Feucht, Dr. Jakob Schluttig und ganz besonders Max Hoffmann bedanke ich mich für die Unterstützung in IT-Fragen und ihre große Geduld mit mir.
- An dieser Stelle ist es auch angebracht, all den Personen aus meinem Arbeitsumfeld zu danken, für die vielen netten, nicht immer wissenschaftlichen, Gespräche und eine tolle Arbeitsatmosphäre, und zwar: Philipp Albert, Johanna Baschek, Anna Battista, Dr. Krzysztof Baczynski, Dr. Achim Besser, Christoph Brand, Yin Cai, Dr. Denis Danilov, Dr. Carina Edwards, Dr. Thorsten Erdmann, Max Hoffmann, Diana Khoromskaia, Heinrich Klein, Christoph Koke, Fridtjof Kowald, Daniel Ockenfeld, Julian Weichsel, Jakob Schluttig, Prof. Dr. Ulrich Schwarz, Jérôme Soiné und Dr. Thomas Striebel von der AG Schwarz, sowie David Dasenbrook, Tarek Elsayed, Ulrich Linden und Dr. Tobias Paul, mit denen ich mir in Heidelberg das Büro geteilt habe.

- Den Mitarbeiterinnen in den Sekretariaten in Heidelberg und Karlsruhe, Sonja Bartsch, Sabine Holthoff, Cornelia Merkel und Melanie Steiert, danke ich für ihre Hilfe in organisatorischen Dingen.
- Vielen Dank auch an Herrn Prof. Dr. Heermann, dass er diese Arbeit als Gutachter bewertet.
- Meinen Eltern, Fernando Guthardt Torres und Birgit Guthardt Torres, danke ich für ihre Unterstützung.
- Nicht zuletzt sei meiner Freundin Karin Klein aufs herzlichste dafür gedankt, dass sie mich immer wieder motiviert und in stressigen Zeiten durch gutes Zureden aufgebaut hat.

Erklärung

Hiermit versichere ich, dass ich die vorliegende Arbeit nicht bereits anderweitig zu Prüfungszwecken eingereicht, die vorliegende Arbeit selbständig verfasst und keine anderen als die angegebenen Hilfsmittel verwendet habe.

Heidelberg, den 27.02.2012 Philip Guthardt Torres